

2011

# Investigation of the Hygroscopic and Morphological Properties of Atmospheric Aerosols

Laura Cook  
*Bucknell University*

Follow this and additional works at: [https://digitalcommons.bucknell.edu/masters\\_theses](https://digitalcommons.bucknell.edu/masters_theses)

 Part of the [Chemical Engineering Commons](#)

---

## Recommended Citation

Cook, Laura, "Investigation of the Hygroscopic and Morphological Properties of Atmospheric Aerosols" (2011). *Master's Theses*. 13.  
[https://digitalcommons.bucknell.edu/masters\\_theses/13](https://digitalcommons.bucknell.edu/masters_theses/13)

This Masters Thesis is brought to you for free and open access by the Student Theses at Bucknell Digital Commons. It has been accepted for inclusion in Master's Theses by an authorized administrator of Bucknell Digital Commons. For more information, please contact [dcadmin@bucknell.edu](mailto:dcadmin@bucknell.edu).

I, Laura B. Cook, do grant permission for my thesis to be copied.



INVESTIGATION OF HYGROSCOPIC AND  
MORPHOLOGICAL PROPERTIES OF ATMOSPHERIC  
AEROSOLS

by

Laura B. Cook

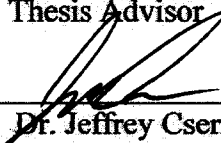
A Thesis

Presented to the Faculty of  
Bucknell University  
In Partial Fulfillment of the Requirements for the Degree of  
Master of Science in the Department of Chemical Engineering

Approved:



Dr. Timothy Raymond  
Thesis Advisor



Dr. Jeffrey Csernica  
Chair, Department of Chemical Engineering



Dr. Michael Gross  
Engineering Thesis Committee



Dr. Ryan Snyder  
Engineering Thesis Committee

Lewisburg, PA  
May 2011

## Acknowledgments

I would first and foremost like to thank my advisor, Dr. Tim Raymond, for his guidance in developing and completing this project. Additionally, I would like to thank him for his incredible enthusiasm towards aerosols science, which was a constant motivation over these last two years. I would also like to thank Dr. Michael Gross and Dr. Ryan Snyder for serving on my thesis committee and for providing the necessary support, guidance and criticism along the way.

I would also like to thank Dr. Chris Daniel and Joe Moore for training me on the ESEM, being available for troubleshooting and for guiding me as I improved my technical abilities on the instrument. On a similar note, I would like to acknowledge Dr. Lansing Madry and Dr. Dabrina Dutcher for their laboratory guidance and willingness to assist. There are many members of the Chemical Engineering Department that deserve recognition, particularly Nancy Lamay for her support and enthusiasm and Diane Hall for her assistance all of these years with acquiring laboratory supplies and contributing technical knowledge. The Aerosols Research Group especially deserves special recognition for at least one great year of data collection, shenanigans, mishaps, and an overall unforgettable experience.

Lastly, and most importantly, I would like to thank my friends and family for their steadfast love and support which made this thesis possible.

# Contents

|                                            |            |
|--------------------------------------------|------------|
| <b>Abstract</b>                            | <b>xxi</b> |
| <b>1 Introduction</b>                      | <b>1</b>   |
| 1.1 Background . . . . .                   | 1          |
| 1.1.1 Atmospheric Aerosols . . . . .       | 1          |
| Aerosol Circulation . . . . .              | 3          |
| Aerosol Size and Composition . . . . .     | 4          |
| Inorganic Aerosols . . . . .               | 6          |
| Organic Aerosols . . . . .                 | 7          |
| 1.1.2 Aerosols and Climate . . . . .       | 8          |
| 1.1.3 Aerosol-Water Interactions . . . . . | 10         |

|                                            |           |
|--------------------------------------------|-----------|
| <i>CONTENTS</i>                            | iv        |
| Clouds . . . . .                           | 10        |
| Relative Humidity . . . . .                | 11        |
| Water Activity . . . . .                   | 12        |
| Deliquescence Relative Humidity . . . . .  | 13        |
| 1.1.4 Growth Factors . . . . .             | 14        |
| 1.1.5 Particle Morphology . . . . .        | 15        |
| 1.1.6 Kappa Values . . . . .               | 16        |
| 1.1.7 Health Effects of Aerosols . . . . . | 17        |
| 1.2 Scope of Thesis . . . . .              | 18        |
| <b>2 Materials and Methods</b>             | <b>20</b> |
| 2.1 Studied Compounds . . . . .            | 20        |
| 2.2 Solvents . . . . .                     | 21        |
| 2.3 Equipment . . . . .                    | 22        |
| Atomizers . . . . .                        | 22        |
| Diffusion Driers . . . . .                 | 23        |

|                                                                    |           |
|--------------------------------------------------------------------|-----------|
| <i>CONTENTS</i>                                                    | v         |
| Scanning Mobility Particle Sizer . . . . .                         | 25        |
| Electrostatic Classifier . . . . .                                 | 26        |
| Differential Mobility Analyzer . . . . .                           | 26        |
| Condensation Particle Counter . . . . .                            | 28        |
| 2.3.1 Hygroscopic Tandem Differential Mobility Analyzer System . . | 29        |
| 2.3.2 Vibrating Orifice Aerosol Generator System . . . . .         | 30        |
| 2.4 Aerosol Imaging and Analysis . . . . .                         | 34        |
| 2.4.1 Scanning Electron Microscope (SEM) . . . . .                 | 34        |
| 2.4.2 Environmental Scanning Electron Microscope . . . . .         | 36        |
| <b>3 Results and Discussion - ESEM</b>                             | <b>40</b> |
| 3.1 Introduction . . . . .                                         | 40        |
| 3.2 Experimental . . . . .                                         | 43        |
| 3.2.1 ESEM Operating Parameters . . . . .                          | 44        |
| 3.2.2 ESEM Analysis . . . . .                                      | 45        |
| 3.3 Results and Discussion . . . . .                               | 48        |

|                                         |           |
|-----------------------------------------|-----------|
| <i>CONTENTS</i>                         | vi        |
| 3.3.1 Ammonium Sulfate . . . . .        | 49        |
| 3.3.2 Ammonium Chloride . . . . .       | 50        |
| 3.3.3 Calcium Chloride . . . . .        | 52        |
| 3.3.4 Sodium Chloride . . . . .         | 53        |
| 3.3.5 Glutaric Acid . . . . .           | 55        |
| 3.3.6 Malonic Acid . . . . .            | 57        |
| 3.3.7 Summary . . . . .                 | 58        |
| <b>4 Results and Discussion - HTDMA</b> | <b>59</b> |
| 4.1 Introduction . . . . .              | 59        |
| 4.2 Experimental . . . . .              | 60        |
| 4.3 Results and Discussion . . . . .    | 64        |
| 4.3.1 Sodium Chloride . . . . .         | 67        |
| 4.3.2 Calcium Chloride . . . . .        | 70        |
| 4.3.3 Ammonium Chloride . . . . .       | 72        |
| 4.3.4 Ammonium Sulfate . . . . .        | 74        |

*CONTENTS*

vii

|        |                                                                    |     |
|--------|--------------------------------------------------------------------|-----|
| 4.3.5  | Ammonium Nitrate . . . . .                                         | 77  |
| 4.3.6  | Adipic Acid . . . . .                                              | 79  |
| 4.3.7  | Aspartic Acid . . . . .                                            | 82  |
| 4.3.8  | Azelaic Acid . . . . .                                             | 84  |
| 4.3.9  | Maleic Acid . . . . .                                              | 86  |
| 4.3.10 | Malonic Acid . . . . .                                             | 88  |
| 4.3.11 | Phthalic Acid . . . . .                                            | 90  |
| 4.3.12 | Succinic Acid . . . . .                                            | 92  |
| 4.3.13 | Tartaric Acid . . . . .                                            | 97  |
| 4.3.14 | Mixture A: Adipic, Maleic, and Malonic Acids . . . . .             | 99  |
| 4.3.15 | Mixture B: Adipic, Succinic, and Malonic Acids . . . . .           | 101 |
| 4.3.16 | Mixture C: Adipic, Glutaric, Maleic, and Succinic Acids . . . . .  | 103 |
| 4.3.17 | Mixture D: Adipic, Glutaric, Maleic, Aspartic and Succinic Acids   | 106 |
| 4.3.18 | Mixture E: Glutaric, Maleic, Tartaric, and Malonic Acids . . . . . | 109 |
| 4.3.19 | Mixture F: Adipic, Aspartic, Phthalic and Azelaic Acids . . . . .  | 111 |

|                                                        |            |
|--------------------------------------------------------|------------|
| <i>CONTENTS</i>                                        | viii       |
| 4.3.20 Mixture G: Phthalic and Azelaic Acids . . . . . | 113        |
| 4.3.21 Mixture H: Tartaric and Malonic Acids . . . . . | 115        |
| 4.3.22 Fitted Curves . . . . .                         | 117        |
| 4.3.23 Kappa Values . . . . .                          | 120        |
| 4.3.24 Summary . . . . .                               | 125        |
| <b>5 Conclusions and Recommendations</b>               | <b>127</b> |
| 5.1 Conclusions . . . . .                              | 127        |
| 5.1.1 ESEM . . . . .                                   | 128        |
| 5.1.2 HTDMA . . . . .                                  | 129        |
| 5.2 Recommendations . . . . .                          | 130        |
| <b>6 Appendix A</b>                                    | <b>131</b> |
| 6.1 UNIFAC Model Derivations . . . . .                 | 131        |
| 6.1.1 Summary . . . . .                                | 133        |
| <b>7 Appendix B</b>                                    | <b>135</b> |

|                                                                    |            |
|--------------------------------------------------------------------|------------|
| <i>CONTENTS</i>                                                    | ix         |
| 7.1 Aerosol Distributions . . . . .                                | 135        |
| <b>8 Appendix C</b>                                                | <b>139</b> |
| 8.1 Atomic Force Microscopy Images of Studied Components . . . . . | 139        |
| 8.1.1 Summary . . . . .                                            | 143        |

# List of Tables

|     |                                                                                                                                    |     |
|-----|------------------------------------------------------------------------------------------------------------------------------------|-----|
| 2.1 | List of Studied Compounds . . . . .                                                                                                | 21  |
| 2.2 | RH(%) Ranges with propagated uncertainties for five sample temperatures . . . . .                                                  | 39  |
| 3.1 | Physical Properties of Chemical Species at 25°C . . . . .                                                                          | 42  |
| 3.2 | Thermodynamic and Solubility Data of Investigated Species . . . . .                                                                | 47  |
| 4.1 | Molecular Structures and Physical Properties of Studied Dicarboxylic Acids . . . . .                                               | 63  |
| 4.2 | Hygroscopic Data of pure component dicarboxylic acids and mixtures. Mixtures of organic species are of equal mass percent. . . . . | 65  |
| 4.3 | Curve Fit Parameters . . . . .                                                                                                     | 118 |
| 4.4 | Experimental Kappa Values . . . . .                                                                                                | 121 |

4.5 Petters and Kreidenweis (2007) Kappa Values . . . . . 123

# List of Figures

|     |                                                                   |    |
|-----|-------------------------------------------------------------------|----|
| 1.1 | Deposition of Atmospheric Aerosols . . . . .                      | 3  |
| 1.2 | Typical Composition of Fine Atmospheric Aerosols . . . . .        | 5  |
| 1.3 | Typical Urban Aerosol Size and Composition Distribution . . . . . | 6  |
| 1.4 | Effect of Aerosols on Radiative Forcing . . . . .                 | 9  |
| 2.1 | Collision-Type Atomizer . . . . .                                 | 22 |
| 2.2 | Filtered Air Supply . . . . .                                     | 23 |
| 2.3 | Diffusion Dryer with Water Trap . . . . .                         | 24 |
| 2.4 | Diffusion Dryer Diagram . . . . .                                 | 24 |
| 2.5 | Electrostatic Classifier . . . . .                                | 27 |
| 2.6 | Differential Mobility Analyzer . . . . .                          | 28 |

|      |                                                                        |    |
|------|------------------------------------------------------------------------|----|
| 2.7  | Condensation Particle Counter . . . . .                                | 29 |
| 2.8  | HTDMA Schematic . . . . .                                              | 30 |
| 2.9  | Vibrating Orifice Liquid Jet Breakup . . . . .                         | 31 |
| 2.10 | Vibrating Orifice Aerosol Generator . . . . .                          | 32 |
| 2.11 | Effects of corrosion on orifice plates . . . . .                       | 33 |
| 2.12 | Scanning Electron Microscope . . . . .                                 | 34 |
| 2.13 | Scanning Electron Microscope . . . . .                                 | 35 |
| 2.14 | Environmental Scanning Electron Microscope . . . . .                   | 37 |
| 3.1  | ESEM image of malonic acid dispersion . . . . .                        | 44 |
| 3.2  | Hygroscopic growth curves for ammonium sulfate . . . . .               | 49 |
| 3.3  | Ammonium sulfate particle at 11%, 54%, 78% and 92%RH . . . . .         | 50 |
| 3.4  | Hygroscopic growth curves for ammonium chloride . . . . .              | 51 |
| 3.5  | Ammonium chloride particle at 7.8%, 74.1%, 80.9% and 90%RH . . . . .   | 52 |
| 3.6  | Hygroscopic growth curves for calcium chloride . . . . .               | 52 |
| 3.7  | Calcium chloride particle at 10.3%, 51.2%, 65.4% and 79.9%RH . . . . . | 53 |

|      |                                                                            |    |
|------|----------------------------------------------------------------------------|----|
| 3.8  | Hygroscopic growth curves for sodium chloride . . . . .                    | 54 |
| 3.9  | Sodium chloride particle at 38%, 73%, 75% and 96.5%RH . . . . .            | 55 |
| 3.10 | Hygroscopic growth curves for glutaric acid . . . . .                      | 56 |
| 3.11 | Glutaric acid particle at 40%, 60%, and 82%RH . . . . .                    | 56 |
| 3.12 | Hygroscopic growth curves for malonic acid . . . . .                       | 57 |
| 3.13 | Malonic acid particle at 9%, 29%, 45%, and 79%RH . . . . .                 | 58 |
| 4.1  | Hygroscopic growth curves for sodium chloride . . . . .                    | 67 |
| 4.2  | Full distribution for a 1 g/L sodium chloride solution . . . . .           | 68 |
| 4.3  | Growth curves for a 1.08 shape factor applied to sodium chloride . . . . . | 69 |
| 4.4  | Size distributions for sodium chloride at 32% and 82%RH . . . . .          | 70 |
| 4.5  | Hygroscopic growth curves for calcium chloride . . . . .                   | 70 |
| 4.6  | Full distribution for a 1 g/L calcium chloride solution . . . . .          | 71 |
| 4.7  | Size distributions for calcium chloride at 20% and 72% RH . . . . .        | 72 |
| 4.8  | Hygroscopic growth curves for ammonium chloride . . . . .                  | 72 |
| 4.9  | Full distribution for a 1 g/L ammonium chloride solution . . . . .         | 73 |

|      |                                                                             |    |
|------|-----------------------------------------------------------------------------|----|
| 4.10 | Size distributions for ammonium chloride at 12%, 60% and 79% RH . . . . .   | 74 |
| 4.11 | Hygroscopic growth curves for ammonium sulfate . . . . .                    | 74 |
| 4.12 | Full distribution for a 1 g/L ammonium sulfate solution . . . . .           | 75 |
| 4.13 | Growth curves for a 1.02 shape factor applied to ammonium sulfate . . . . . | 76 |
| 4.14 | Size distributions for ammonium sulfate at 40% and 82% RH . . . . .         | 76 |
| 4.15 | Hygroscopic growth curves for ammonium nitrate . . . . .                    | 77 |
| 4.16 | Full distribution for a 1 g/L ammonium nitrate solution . . . . .           | 77 |
| 4.17 | Size distributions for ammonium nitrate at 10% and 85% RH . . . . .         | 78 |
| 4.18 | Hygroscopic growth curves for adipic acid . . . . .                         | 79 |
| 4.19 | Full distribution for a 1 g/L adipic acid solution . . . . .                | 79 |
| 4.20 | Size distributions for adipic acid at 8% and 72% RH . . . . .               | 80 |
| 4.21 | AFM images for adipic acid . . . . .                                        | 81 |
| 4.22 | Hygroscopic growth curves for aspartic acid . . . . .                       | 82 |
| 4.23 | Full distribution for a 1 g/L aspartic acid solution . . . . .              | 82 |
| 4.24 | Size distributions for aspartic acid at 16% and 74% RH . . . . .            | 83 |

|      |                                                                      |    |
|------|----------------------------------------------------------------------|----|
| 4.25 | Hygroscopic growth curves for azelaic acid . . . . .                 | 84 |
| 4.26 | Full distribution for a 1 g/L azelaic acid solution . . . . .        | 84 |
| 4.27 | Size distributions for azelaic acid at 7% and 75% RH . . . . .       | 85 |
| 4.28 | Hygroscopic growth curves for maleic acid . . . . .                  | 86 |
| 4.29 | Full distribution for a 1 g/L maleic acid solution . . . . .         | 86 |
| 4.30 | Size distributions for maleic acid at 8% and 82% RH . . . . .        | 87 |
| 4.31 | Hygroscopic growth curves for malonic acid . . . . .                 | 88 |
| 4.32 | Full distribution for a 1 g/L malonic acid solution . . . . .        | 88 |
| 4.33 | Size distributions for malonic acid at 32% and 72% RH . . . . .      | 89 |
| 4.34 | Hygroscopic growth curves for phthalic acid . . . . .                | 90 |
| 4.35 | Full distribution for a 1 g/L phthalic acid solution . . . . .       | 90 |
| 4.36 | Size distributions for phthalic acid at 16% and 82% RH . . . . .     | 91 |
| 4.37 | Hygroscopic growth curves for succinic acid . . . . .                | 92 |
| 4.38 | Full distribution for a 1 g/L succinic acid solution . . . . .       | 92 |
| 4.39 | Size distributions for succinic acid at 8%, 62% and 72% RH . . . . . | 94 |

|      |                                                                  |     |
|------|------------------------------------------------------------------|-----|
| 4.40 | AFM images of Succinic Acid . . . . .                            | 95  |
| 4.41 | AFM images of 63 nm Succinic Acid . . . . .                      | 96  |
| 4.42 | Hygroscopic growth curves for tartaric acid . . . . .            | 97  |
| 4.43 | Full distribution for a 1 g/L tartaric acid solution . . . . .   | 97  |
| 4.44 | Size distributions for tartaric acid at 17% and 83% RH . . . . . | 98  |
| 4.45 | Hygroscopic growth curves for mixture A . . . . .                | 99  |
| 4.46 | Full distribution for a 1 g/L mixture A solution . . . . .       | 99  |
| 4.47 | Size distributions for mixture A at 9% and 77% RH . . . . .      | 100 |
| 4.48 | Hygroscopic growth curves for mixture B . . . . .                | 101 |
| 4.49 | Full distribution for a 1 g/L mixture B solution . . . . .       | 101 |
| 4.50 | Size distributions for mixture B at 10% and 71% RH . . . . .     | 102 |
| 4.51 | Hygroscopic growth curves for mixture C . . . . .                | 103 |
| 4.52 | Full distribution for a 1 g/L mixture C solution . . . . .       | 104 |
| 4.53 | Size distributions for mixture C at 20% and 80% RH . . . . .     | 105 |
| 4.54 | Hygroscopic growth curves for mixture D . . . . .                | 106 |

|      |                                                                  |     |
|------|------------------------------------------------------------------|-----|
| 4.55 | Full distribution for a 1 g/L mixture D solution . . . . .       | 107 |
| 4.56 | Size distributions for mixture D at 21% and 80% RH . . . . .     | 108 |
| 4.57 | Hygroscopic growth curves for mixture E . . . . .                | 109 |
| 4.58 | Full distribution for a 1 g/L mixture E solution . . . . .       | 110 |
| 4.59 | Size distributions for mixture E at 16% and 80% RH . . . . .     | 111 |
| 4.60 | Hygroscopic growth curves for mixture F . . . . .                | 111 |
| 4.61 | Full distribution for a 1 g/L mixture F solution . . . . .       | 112 |
| 4.62 | Size distributions for mixture F at 13% and 80% RH . . . . .     | 113 |
| 4.63 | Hygroscopic growth curves of mixture G . . . . .                 | 113 |
| 4.64 | Full distribution for a 1 g/L mixture G solution . . . . .       | 114 |
| 4.65 | Size distributions for mixture G at 8% and 80% RH . . . . .      | 115 |
| 4.66 | Hygroscopic growth curves of mixture H . . . . .                 | 115 |
| 4.67 | Full distribution for a 1 g/L mixture H solution . . . . .       | 116 |
| 4.68 | Size distributions for mixture H at 6% and 81% RH . . . . .      | 117 |
| 4.69 | Curved fit for the mode growth factors of all mixtures . . . . . | 119 |

|      |                                                                            |     |
|------|----------------------------------------------------------------------------|-----|
| 4.70 | Curved fit for the geometric mean growth factors of all mixtures . . . . . | 119 |
| 4.71 | Experimental Kappa Values for the Mode . . . . .                           | 122 |
| 4.72 | Experimental Kappa Values for the Geometric Mean . . . . .                 | 122 |
| 4.73 | Comparison of Experimental and Literature Kappa Values . . . . .           | 124 |
| 4.74 | Comparison of HTDMA-derived and CCNC-derived Kappa Values . . . . .        | 125 |
| 7.1  | Number concentration of HTDMA solutions . . . . .                          | 136 |
| 7.2  | Mass concentration of HTDMA solutions . . . . .                            | 136 |
| 7.3  | Median of HTDMA solution distributions . . . . .                           | 137 |
| 7.4  | Mean of HTDMA solution distributions . . . . .                             | 137 |
| 7.5  | Mode of HTDMA solution distributions . . . . .                             | 138 |
| 7.6  | Geometric mean of HTDMA solution distributions . . . . .                   | 138 |
| 8.1  | AFM images of Adipic Acid . . . . .                                        | 140 |
| 8.2  | AFM images of Aspartic Acid . . . . .                                      | 140 |
| 8.3  | AFM images of Azelaic Acid . . . . .                                       | 141 |
| 8.4  | AFM images of Maleic Acid . . . . .                                        | 141 |

*LIST OF FIGURES*

|     |                                       |     |
|-----|---------------------------------------|-----|
| 8.5 | AFM images of Malonic Acid . . . . .  | 142 |
| 8.6 | AFM images of Phthalic Acid . . . . . | 142 |

# Abstract

The study of atmospheric aerosols has become increasingly important as aerosols have been linked to air quality degradation and subsequent health issues, visibility degradation, and climate change. The effect of aerosols on climate change is complicated through direct and indirect effects with respect to radiative forcing due to aerosol-water interactions. Directly, aerosols scatter and absorb radiation. Indirectly, aerosols alter the rate of chemical reactions in the atmosphere that may form or destroy pollutants. Additionally, the aerosols may influence secondary factors, such as precipitation, which control how aerosols deposit.

Dry atmospheric particles that interact with water create aerosols of varying light-scattering properties, atmospheric lifetimes, chemical reactivities and cloud-nucleating abilities. The complications of these properties due to water interactions and the paucity of data currently available yield the importance for understanding and quantifying these aerosol-water interactions.

The first objective of this thesis was to examine the hygroscopic and morphological nature of various substances through the use of an Environmental Scanning

Electron Microscope (ESEM). The hygroscopic growth and changes in morphology for pure-component aerosols were studied for particles greater than 2  $\mu\text{m}$  in size. Hygroscopic growth was observed through changes in relative humidity (RH) and hygroscopic growth curves were created for ammonium sulfate, ammonium chloride, sodium chloride, calcium chloride, glutaric acid, and malonic acid. The ESEM system is advantageous over the Hygroscopic Tandem Differential Mobility Analysis (HTDMA) system because it offers a *in-situ* view of changes in morphology as particles experience water uptake.

The second objective of this thesis, the hygroscopic growth of multi-component aerosol mixtures, was studied using Hygroscopic Tandem Differential Mobility Analysis (HTDMA). The size distribution for an aerosol stream was determined before and after the stream was subjected to an increase in relative humidity. The complex mixtures examined contained combinations in equal mass amounts of adipic acid, glutaric acid, maleic acid, aspartic acid, tartaric acid, succinic acid, malonic acid, phthalic acid, and azelaic acid. Pure solutions of sodium chloride, ammonium sulfate, ammonium chloride, ammonium nitrate, calcium chloride, maleic acid, tartaric acid, malonic acid, and phthalic acids were also run through the HTDMA system. Novel methods for comparing hygroscopic (<100%RH) and cloud condensation nuclei (>100%RH) data were applied to these data in the form of kappa values.

Understanding the hygroscopic growth and morphology of aerosols are essential for understanding cloud formation and climate change. This research will provide insight into the physical morphological changes that atmospheric particles exhibit when experiencing changes in humidity. The results of this research will lead to

a greater comprehension of the hygroscopic properties for organic, inorganic, and mixed composition aerosols. The understanding of physical and chemical changes that aerosols experience will lead to a better understanding of the impact anthropogenic and biogenic emissions have on the atmosphere and ultimately, more accurate climate models can be formulated.

# Chapter 1

## Introduction

### 1.1 Background

#### 1.1.1 Atmospheric Aerosols

Aerosols are solids or liquid particles suspended in a gas and generally range in size from nanometers to over 100  $\mu\text{m}$ . Aerosols are formed from natural and anthropogenic sources and these particles are continuously held within the atmosphere. Sources of natural particles include rock and soil debris, sea spray, volcanic action, and biomass burning. Natural sources, which directly emit the particles into the atmosphere, are considered primary sources. Sources of particles attributed to humans primarily arise from fuel combustion, industrial processes, and nonindustrial sources (e.g. roadway dust, construction). Anthropogenic sources account for approximately 10 percent of

the total amount of aerosols in our atmosphere globally. The concentration of particles in the atmosphere tends to change based on the location, as urban areas have higher concentrations than rural areas due to the higher density of anthropogenic sources. A cubic centimeter of air typically contains 100 to 10,000 particles, but more urban areas may contain over one million particles per cubic centimeter [1].

Emissions of particles as a result of gases reacting and condensing or cooling (gas-to-particle conversion) are considered secondary aerosols. An example of a secondary organic aerosol (SOA) is the atmospheric oxidation of biogenic (plant debris, humic matter, microbial particles) hydrocarbons, which produces particles of low volatility that are more susceptible to aerosol formation [2]. Specifically, sulfate aerosols are often formed through chemical reactions from the conversion of gaseous precursors and are considered to be a highly ubiquitous component of aerosol composition.

Once atmospheric aerosols are formed, the propensity for the particles to remain in the atmosphere are dependent on many factors, including particle stability, size, concentration and environmental conditions (e.g. other compounds, wind speed). Figure 1.1 describes these factors that lead to aerosol deposition [3].

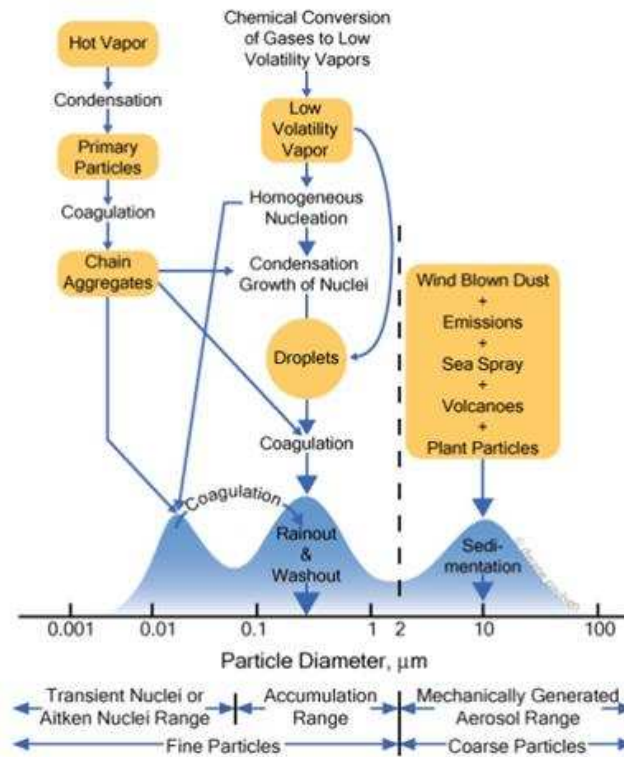


**Figure 1.1:** Deposition of Atmospheric Aerosols (Whitby and Cantrell, 1976)

## Aerosol Circulation

Aerosols are altered, removed or destroyed once they enter the atmosphere, which results in varied lifetimes of the particles in the atmosphere. Average aerosol lifetimes are on the order of a few days to a week, but depend heavily on particle size and location. Aerosols exit the atmosphere through two main processes: wet deposition and dry deposition.

Wet deposition includes types of deposition involving water, such as rainout,

washout, sweepout, and occult deposition. Rainout occurs when aerosols are small enough to act as nuclei for the condensation of cloud droplets. Once the droplets grow to a large enough size, they gravitationally settle to the surface as rain drops. Washout is very similar to rainout in that cloud droplets fall as rain. However, with washout, the aerosols are incorporated into pre-existing cloud drops that grow until settling. Sweepout occurs when aerosols below the cloud base of a raining cloud impact into falling raindrops. Finally, occult deposition occurs when aerosols are incorporated into droplets near the ground, such as with fog or orographic clouds. Occult deposition is dependent on impaction efficiency and sticking efficiency. Impaction efficiency increases for larger droplets as they are more likely to impact a surface than smaller particles. Sticking efficiency is the probability that an impacted object will not bounce off and be instantly re-suspended.

Dry deposition describes the process of depositing particles to a surface without the aid of precipitation. Types of dry deposition include gravitational settling and turbulent deposition. Gravitational settling occurs when large particles fall to the surface under the force of gravity and turbulent deposition occurs when dry particles are forced through the boundary layer to the surface. Particle aggregates are often formed with turbulence induced impaction due to the higher frequency of collision.

### **Aerosol Size and Composition**

Atmospheric aerosols are created from inorganic and organic chemicals. In a laboratory setting, these compositions can be made to specification. However, atmospheric

aerosols are composed of hundreds of thousands of organic and inorganic chemicals which are difficult to fully model experimentally. Typical aerosol compositions are characterized in Figure 1.2.

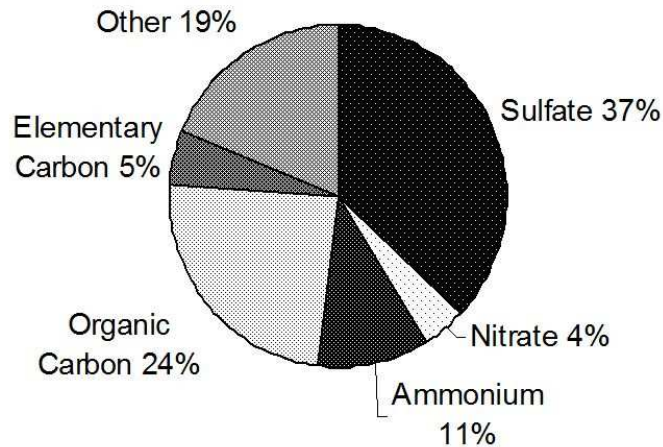


**Figure 1.2:** Typical Composition of Fine Atmospheric Aerosols (Jacob, 1999)

As illustrated in Figure 1.1, the size of an aerosol strongly affects its reactivity and deposition. It is because of this influence that atmospheric aerosols are divided into specific categories based on their size:

- Coarse aerosols - typically range in size from 1 to 10  $\mu\text{m}$  in radius. These aerosols are typically formed from natural sources.
- Fine aerosols - typically range in size from 0.1 to 2.5  $\mu\text{m}$  in radius. These aerosols are also known as accumulation mode particles and the aerosols are typically formed from the condensation of gases already in the atmosphere, such as sulfuric acid, ammonium, and organic compounds.

- Ultra fine aerosols - typically in the size range of  $10^{-4}$  to  $10^{-3}$   $\mu\text{m}$ . These aerosols are formed by nucleation, the grouping of gas molecules. As condensation and coagulation (collision of aerosols by random motion) occur, these aerosols quickly grow to form fine aerosols.

### Inorganic Aerosols

In a study performed by Wall *et al.* (1988), the concentration and size distributions of aerosol sulfate, nitrate, ammonium, chloride, sodium, and hydrogen ions were quantified for samples collected in Claremont, CA. Figure 1.3 describes how composition was related to size and concentration for this study.

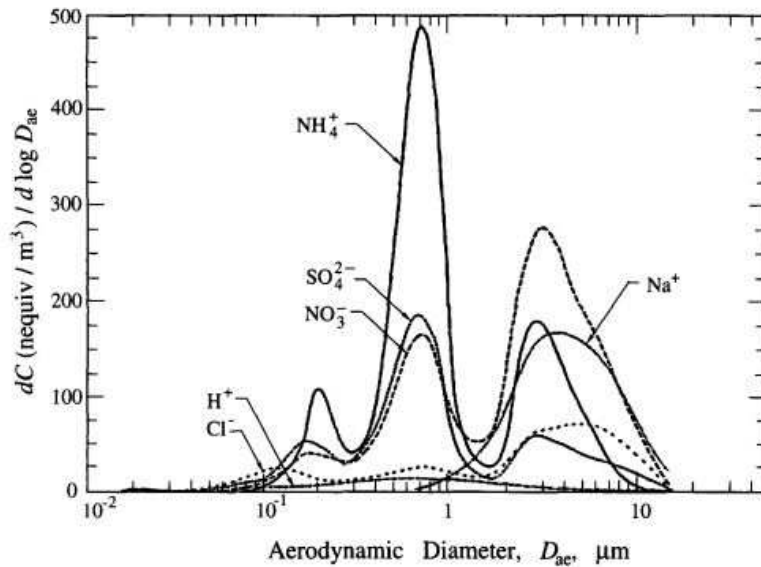


**Figure 1.3:** Atmospheric Environment  
(Wall *et al.*, 1988)

These results indicate that inorganic ions (sulfate, nitrate, ammonium) experience two modes over 0.1-1.0  $\mu\text{m}$  and a third mode over 1  $\mu\text{m}$ , which are classified as coarse mode aerosols. In fact, over half of the nitrate was found to be in coarse mode with the sodium and chloride ions, which is attributed to the reaction of nitric acid (industrial emissions) with sodium chloride [4].

Total global aerosol sources for sulfate, nitrate and sodium chloride are estimated to be 200 Tg sulfate/yr., 14.2 Tg nitrate/yr., and 54 Tg sea salt/yr. (where 1 Tg = million metric tonnes) [5]. The production of sodium chloride is naturally occurring from oceans while sulfate and nitrate particles are typically formed from secondary sources (gas-to-particle conversion) or anthropogenic primary sources. It is also interesting to note that nitrate and ammonium deposition are twice that of pre-industrial times and sulfate deposition is currently five times that of pre-industrial times [6].

### **Organic Aerosols**

Organic aerosol concentrations have been reported to constitute 20-50 % of total final aerosol mass in the United states, second to sulfate and nitrate concentrations [7]. Carbonaceous aerosols are comprised of elemental carbon, carbonate carbon and organic carbon [8]. Elemental carbon aererosols are produced through combustion and carbonate carbon is produced by soil dust. For this study, only organic carbon aerosols were studied as they are the most complex and least understood of aerosols. Specifically, dicarboxylic acids were studied. Other components of organic aerosols include *n*-alkanes, *n*-alkanoic acids, *n*-alkanals, diterpenoid acids and retene, aromatic

polycarboxylic acids, polycyclic aromatic hydrocarbons, polycyclic aromatic ketons and quinones, steroids, nitrogen-containing compounds, regular steranes, pentacyclic triterpanes, and iso- and anteiso-alkanes [1]. In a study performed by Ludwig and Klemm (1988), dicarboxylic acids were determined to constitute the majority of organic acids aerosols. Due to the complexity of chemical structure and subsequent impact on the atmosphere, organic aerosol behavior is not as well understood as inorganic aerosols, and thus proves the significance for understanding the hygroscopic behavior the mixed of organic and inorganic aerosols.

### 1.1.2 Aerosols and Climate

Aerosols affect the Earth's climate directly, by scattering and absorbing radiation, and indirectly, by serving as nuclei for cloud formation. Clouds control the reflection of solar radiation and the trapping of energy near the Earth and thus, control weather and climate changes. Because clouds are comprised of aerosols, aerosols have been studied for their association with climate change. Increased concentrations of hydrophilic tropospheric aerosols ultimately reduce mean droplet size because the fixed amount of water vapor in the surrounding air is divided among more condensation nuclei [10]. Increased numbers of smaller cloud droplets increases the optical density and albedo of the cloud, which scatters more shortwave radiation and absorbs more long wave radiation. Increased numbers of smaller droplets also decrease the number of droplets that form precipitation. Since these droplets cannot deposit from the atmosphere, their atmospheric lifetimes are prolonged, which exaggerates the same effects.

The scattering of shortwave radiation increases the overall planetary albedo, which results in a cooling effect on climate. In particular, sulfate aerosols contribute to a global mean radiative forcing ranging from  $-0.26$  to  $-0.82 \text{ Wm}^{-2}$  [2]. The absorption of radiation, such as by black carbon aerosols, produce an overall warming effect on the climate. Black carbon aerosols are produced from fossil fuels and biomass burning emissions and contribute to a global mean radiative forcing ranging from  $+0.27$  to  $+0.54 \text{ Wm}^{-2}$ . The effects that aerosols have on the warming or cooling changes of climate are described in Figure 1.4

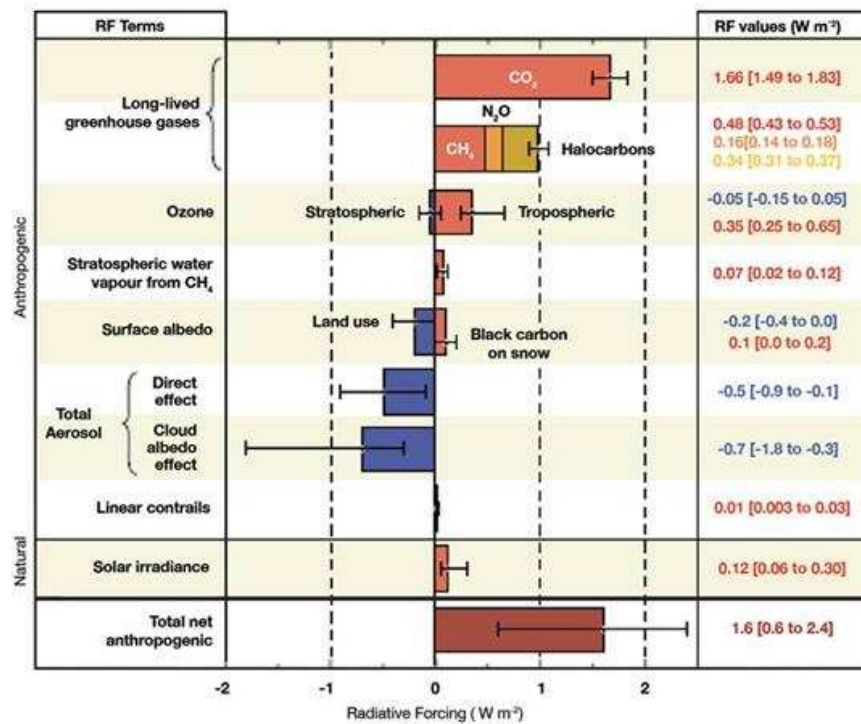


Figure 1.4: Effect of Aerosols on Radiative Forcing (IPCC, 2007)

As can be seen from Figure 1.4, the amount of uncertainty associated with aerosol effects on radiative forcing is much greater than that of other atmospheric constituents (i.e. greenhouse gases, ozone) and contributes to the large error in the total net anthropogenic radiative forcing. It can thus be surmised that aerosol interactions have considerable influence and require improved quantitative understanding.

### 1.1.3 Aerosol-Water Interactions

The Earth's oceans comprise more than 97% of the Earth's water where 2.1% is contained in the polar ice caps. Only about 0.001% of Earth's water is contained in the atmosphere and yet, the interaction between water and atmospheric aerosols can lead to profound changes in cloud formation, aerosol deposition and climate change.

#### Clouds

Clouds are formed when water vapor hydrates aerosol particles, causing the particles to grow into cloud droplets [11]. Particles that become activated to grow into cloud droplets in the presence of supersaturated water vapor are termed cloud condensation nuclei (CCN). When a particle is in a moisture rich environment below its deliquescence relative humidity (DRH), water may adsorb onto the surface, which has the potential of changing the composition and morphology of the particle. As the RH reaches above the DRH of the particle, water condenses onto the solution droplet. When the relative humidity is at or above 100%, water spontaneously condenses onto

CCN. While many hydrophobic or water-insoluble particles do not hygroscopically grow under 100% RH, these particles may act as CCN when the RH reaches above 100% [12]. The hygroscopicity of particle aggregates is dependent on the composition of the particles. According to a closure study performed by McFiggans *et al.* (2005), the inorganic component of aerosols are most responsible for any increase in hygroscopicity. However, bulk solution measurements performed by Marcolli *et al.* (2004) suggested that complex mixtures composed of five or more dicarboxylic acids will undergo deliquescence at relative humidities less than that of the pure inorganic salt largely due to an increased entropy of mixing.

The difference in diameters between the average condensation nucleus, average cloud droplet, and the average rain drop are approximately 0.0002 mm, 0.02 mm, and 2 mm, respectively. Precipitation results from the hygroscopic growth of a cloud condensation nucleus to the size of a droplet. For fine atmospheric particles ( $\leq 2.5 \mu\text{m}$ ), water typically constitutes more than half of the particle mass at relative humidities exceeding 80% [16].

## Relative Humidity

*Relative humidity* (RH) is defined as the percent ratio of the partial pressure of water,  $p_w$ , to its saturation vapor pressure,  $p_w^o$ , and is used to describe the amount of water vapor in a gaseous mixture:

$$RH(\%) = \frac{p_w}{p_w^o} * 100 \quad (1.1)$$

where a higher relative humidity value represents greater water vapor pressure. The typical relative humidity of the atmosphere has been reported as below 110%, and most often below 102% [12]. Changes in atmospheric RH generally occur when a parcel of air is cooled either isobarically or adiabatically. Isobaric cooling occurs when an air parcel moves horizontally over a cooler land mass. Adiabatic cooling occurs when a rising air parcel experiences decreases in pressure. Both of these processes result in a reduced temperature of the air and thus, a decrease in the saturation vapor pressure. As shown by Equation 1.1, a decrease in saturation vapor pressure ( $p_w^o$ ) leads to an increase in RH.

### Water Activity

Although HTDMA measurements were made using relative humidity, it is more convenient to express water uptake of aerosols by *water activity* ( $a_w$ ). The relationship between RH and  $a_w$  for a solution droplet is as follows:

$$\frac{RH}{100} = \frac{p_w}{p_w^o} = a_w \exp\left(\frac{4\sigma_s M_w}{\rho_w R T d_p}\right) \quad (1.2)$$

where the exponential term accounts for the Kelvin curvature effect,  $P_w$  is water partial pressure,  $P_w^o$  is the saturation vapor pressure of water,  $\sigma_s$  is the surface tension

of the solution,  $M_w$  is the molar mass of water,  $\rho_w$  is the density of water,  $R$  is the ideal gas constant,  $T$  is the absolute temperature, and  $d_p$  is the droplet diameter. This relation assumes the water uptake by the aerosol does not change the RH, which can occur when aerosol concentrations are too high. For particles greater than  $\sim 80$  nm, the exponential term converges to unity.

### **Deliquescence Relative Humidity**

For any given type of soluble particle, there is a critical value of RH below which the particle is stable and above which the particle spontaneously grows to become a droplet [1]. This transition is called deliquescence and occurs at the *deliquescence relative humidity* (DRH). Deliquescence is dependent on particle composition, size, physiochemical properties and morphology. Particles which do not exhibit deliquescence but grow smoothly as the relative humidity changes are termed *hygroscopic*. After deliquescence, aerosols grow hygroscopically to maintain thermodynamic equilibrium with water vapor.

The term hygroscopic behavior is frequently used to describe overall water-interactions of aerosols. Hygroscopic behavior is independent of individual aerosol species and can be either deliquescent or hygroscopic in nature. Throughout this study, the term hygroscopic behavior will be used to describe overall water-aerosol interactions and hygroscopic will be used to describe the smooth particle growth with increasing RH.

### 1.1.4 Growth Factors

Experimental growth factors were calculated by comparing the size of particles during growth ( $d_p$ ) to that of the dry particle ( $d_{p,o}$ ). To form a theoretical growth factor model, the UNiversal Functional Activity Coefficient (UNIFAC) model was employed. For this study, the mole fraction of water and the mole fractions of the components involved were known. For a given mole fraction of water ( $x_w$ ) and a calculated activity coefficient ( $\gamma_w$ ), which was determined by UNIFAC through binary interaction parameters, the water activity for the system was calculated. By using the mole fraction of water and mole fractions of the system, the mass fraction solute ( $mfs$ ) of the system was calculated. The mass fraction solute ( $mfs$ ) was then used to determine growth factors (GF) through:

$$GF = \frac{d_p}{d_{p,o}} = \left[ \frac{\rho_s \left( \frac{mfs}{\rho_s} + \frac{1-mfs}{\rho_w} \right)}{mfs} \right]^{1/3} \quad (1.3)$$

where  $d_p$  is the droplet diameter,  $d_{p,o}$  is the dry particle diameter,  $\rho_s$  is the dry solute density, and  $\rho_w$  is the density of water. Equation 1.3 assumed volume additivity to approximate the wet droplet density, as has been previously assumed in past studies [17; 18; 19]. To create a growth factor curve, growth factors were plotted against water activity. Additional explanations on the UNIFAC model can be found in Appendix A.

### 1.1.5 Particle Morphology

This study will also provide insight to one of the least understood properties of atmospheric particles – morphology. The morphology of particles influences a large number of industries, such as the pharmaceutical industry, where the size and state of particle agglomerates affect particle behavior in the human body. The morphology of nanopowders also affects the product quality of many manufactured goods, such as printer toners, rubbers, paints, and fillers [20].

Shape factors ( $\chi$ ) will be integrated into growth factor calculations to account for differences in particle morphology, where a dynamic shape factor is defined as the ratio of actual resistance force for a nonspherical particle to the resistance force of a spherical particle of equivalent volume and settling velocity.

$$\chi = \frac{F_D}{F_{D,M}} = \frac{F_D}{3\pi\eta V_T d_e} \quad (1.4)$$

$F_D$  is the drag force applied to a nonspherical particle,  $\eta$  is the air viscosity ( $1.81 \cdot 10^{-5}$  Pa·s under normal conditions),  $V_T$  is the terminal velocity of the nonspherical particle, and  $d_e$  is the equivalent volume diameter of the nonspherical particle. The drag force ( $F_D$ ) and terminal velocity ( $V_T$ ) of the particle have been determined experimentally in past studies [21]. Calculations involving the equivalent volume diameter of a cubic, nonspherical particle compared to that of a spherical particle are shown here:

$$\begin{aligned}
V_{sphere} &= \frac{\pi d^3}{2} \\
V_{cube} &= a^3 \\
V_{sphere} &= V_{cube} \\
\frac{\pi d^3}{2} &= a^3 \\
d_e &= \frac{a}{\sqrt[3]{\frac{\pi}{2}}}
\end{aligned}
\tag{1.5}$$

Once  $F_D$ ,  $V_T$ , and  $d_e$  are determined, a shape factor can be calculated. In the case of a cubic particle,  $\chi$  equals 1.08. For a spherical morphology,  $\chi$  is equivalent to 1.0 [22].

### 1.1.6 Kappa Values

Petters and Kreidenweis (2007) developed a single parameter to relate particle dry diameters and cloud condensation nuclei (CCN),  $\kappa$ . This parameter was applied to 25 components, 8 of which were used in this study. Lower values of  $\kappa$  describe components that exhibit less hygroscopic or less CCN-active behavior. Linking HTDMA and CCN data has value such that by knowing the results of one system would lead to predictions of the other. To calculate hygroscopic  $\kappa$  values, the following equation was used, as derived by Carrico *et al.* (2008):

$$\kappa_{hygro.} = \frac{(GF^3 - 1)(1 - a_w)}{a_w} \quad (1.6)$$

### 1.1.7 Health Effects of Aerosols

It is well known that the inhalation of small particles can have detrimental health effects, including asthma, lung cancer, and cardiovascular problems, where particles less than  $10 \mu\text{m}$  have a higher probability of depositing deeper into the lungs. Deeper deposition results in a higher probability of blood absorption or physical interaction with the lungs which can pose health risks [24].

Particles greater than  $10 \mu\text{m}$  are typically filtered through the tortuous nose or throat and therefore, do not cause problems whereas particles smaller than  $10 \mu\text{m}$  have the possibility of depositing in the bronchi and lungs. Nanoparticles (particles less than  $100 \text{ nm}$ ) are the most threatening because they can pass through cell membranes to travel throughout the blood stream to organs, such as the brain. Some studies have suggested that particles settling in the brain could be a cause of series diseases, such as Alzheimer Disease [25].

While particle size primarily affects deposition, so does morphology. Angular particles tend to have a high surface area which increases the capability for other particles or chemicals to bind to the particle. When hazardous chemicals bond to the particles, the potential for health risks increases. Aerosol drug delivery is being studied as one method to treat health problems as it is a rapid treatment method

with a minimal dose and minimal side effects in comparison to other drug delivery options (e.g. buccal, intravenous). One of the main challenges for drug delivery is due to the hygroscopic nature of particles. Since the air and the pathway linings of the human body have moisture, aerosol growth occurs and changes in particle size affect aerosol deposition. By studying the nature of particle morphology and hygroscopic growth, better treatment methods can be created.

## 1.2 Scope of Thesis

The investigation of the hygroscopic and morphological properties of aerosols is divided into three major sections.

Chapter 2 describes the main instrumentation and methods used throughout the study. The Environmental Scanning Electron Microscope (ESEM) is a novel *in-situ* technique for characterizing single aerosol hygroscopicity and morphology whereas the Hygroscopic Tandem Differential Mobility Analyzer (HTDMA) system is a more commonly used system in atmospheric hygroscopic studies. The humidification system for the HTDMA was built from laboratory materials and its accuracy was verified by analyzing well-studied pure components.

Chapter 3 describes the operating parameters, theory and results for the ESEM system. For this study, pure components with a dry volume diameter between 2-10  $\mu\text{m}$  were analyzed. The pure components used in this experiment included ammonium sulfate, ammonium chloride, sodium chloride, calcium chloride, glutaric acid, and

malonic acid.

Chapter 4 describes the operating parameters, theory and results for the HTDMA system. For this system, pure inorganic and organic components were analyzed to elucidate their hygroscopic properties. These pure solutions included sodium chloride, ammonium sulfate, ammonium chloride, ammonium nitrate, calcium chloride, azelaic acid, aspartic acid, maleic acid, tartaric acid, malonic acid, and phthalic acids. The study of complex mixtures provided atmospherically relevant information, which can be used for the modeling of real atmospheric conditions. Solutions of these mixed compounds were created to an equivalent 1 g/L solution: adipic acid, glutaric acid, maleic acid, aspartic acid, tartaric acid, succinic acid, malonic acid, phthalic acid, and azelaic acid. Further comparison of kappa values for experimental HTDMA and CCN work to that of published literature was summarized.

Chapter 5 summarizes the experimental results and provides recommendations based on these results. Chapter 6 describes the UNIFAC model as Appendix A. Chapter 7 is a compilation of raw HTDMA data for a full distribution (prior to size-selection) and is listed as Appendix B. Chapter 8 is a compilation of Atomic Force Microscopy images published by Juan Lopez Ruiz (2009) that were compared to the experimental data from this study and is also listed as Appendix C.

## Chapter 2

# Materials and Methods

### 2.1 Studied Compounds

A comprehensive list of the pure components for both the Environmental Scanning Electron Microscope (ESEM) and Hygroscopic Tandem Differential Analysis (HTDMA) system are tabulated in Table 2.1. The components varied slightly between systems (HTDMA and ESEM) and mixtures were made from these pure components for the HTDMA experiments, as described in Table 4.2.

**Table 2.1:** List of Studied Compounds

| Compound          | Chemical Formula | Supplier       | Purity (%) |
|-------------------|------------------|----------------|------------|
| Ammonium Chloride | $NH_4Cl$         | Alfa Aesar     | 99         |
| Ammonium Sulfate  | $(NH_4)_2SO_4$   | Alfa Aesar     | 99         |
| Calcium Chloride  | $CaCl_2$         | FisherBiotech  | 99         |
| Sodium Chloride   | $NaCl$           | Alfa Aesar     | 99         |
| Adipic Acid       | $C_6H_{10}O_4$   | Alfa Aesar     | 99+        |
| DL-Aspartic Acid  | $C_4H_7NO_4$     | Acros Organics | 99+        |
| Azelaic Acid      | $C_9H_{16}O_4$   | Fluka          | 99+        |
| Glutaric Acid     | $C_5H_8O_4$      | Alfa Aesar     | 99         |
| Maleic Acid       | $C_4H_4O_4$      | Fluka          | 99+        |
| Malonic Acid      | $C_3H_4O_4$      | Alfa Aesar     | 99         |
| Phthalic Acid     | $C_8H_6O_4$      | Fluka          | 99.5+      |
| Succinic Acid     | $C_4H_6O_4$      | Alfa Aesar     | 99+        |
| L-Tartaric Acid   | $C_4H_6O_6$      | Aldrich        | 99.5       |

## 2.2 Solvents

The water used in all experiments was purified using a Millipore, Inc. Simplicity Water Purification System, which purified water to a resistivity of at least 18.2 M $\Omega$ -cm at 25°C. Any alcohol solvents used in the experiments (mainly isopropanol) were of 99.5+% purity and 0.001% maximum residue after evaporation.

## 2.3 Equipment

### Atomizers

Aerosols were generated from solution using a collision-type TSI Model 3076 Atomizer (Figure 2.1) at a pressure of 35 psia, which produced a flow rate of  $3.244 \pm 0.005$  L/min. The solutions were made with ultra-pure water and were pulled into a syringe. The aerosols were generated by expansion of the solution through the atomizer nozzle due to the flow of compressed air. Increased air pressure generated higher flow rates of aerosols.

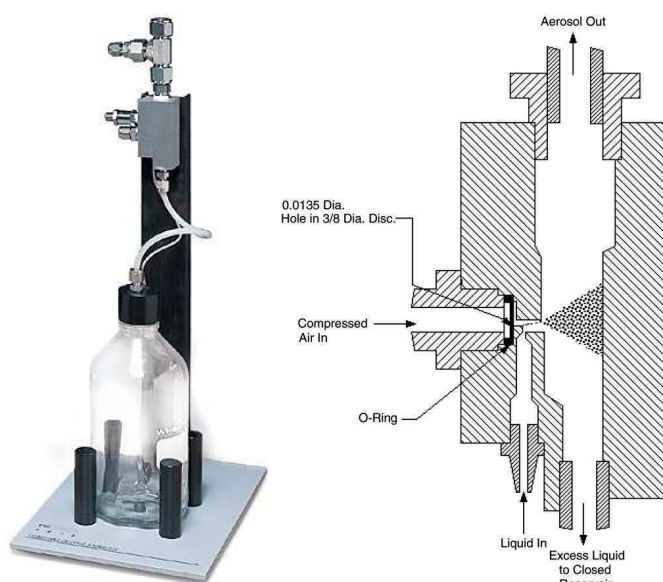


**Figure 2.1:** Collision-Type Atomizer  
(<http://www.tsi.com> and TSI Model 3076 Constant Output Atomizer Manual)

The compressed air used to atomize solutions was first filtered using the Model

3074B TSI filtered air supply, shown in Figure 2.2. Two pre-filters prevent large particles and water from entering the instrument, a membrane dryer uses selective permeation to dehumidify the air, and a separate filter uses activated carbon pellets to remove oil vapors and residual particles.



**Figure 2.2:** Filtered Air Supply  
(<http://www.tsi.com>)

### Diffusion Driers

Since aerosols are generated through the atomizing process and particles are collected for imaging, solvent must be removed from the aerosols without damaging the final product. To accommodate this removal of solvent, the aerosol stream first entered a diffusion dryer equipped with a water trap, as shown in Figure 2.3. The stream then entered a series of five dryers, which were utilized to simulate the atmospheric process of drying. These dryers consist of concentric tubes where the aerosols pass through the center of the dryer while the surrounding desiccant absorbs water, as illustrated in Figure 2.4.



**Figure 2.3:** Diffusion Dryer with Water Trap  
(<http://www.tsi.com>)

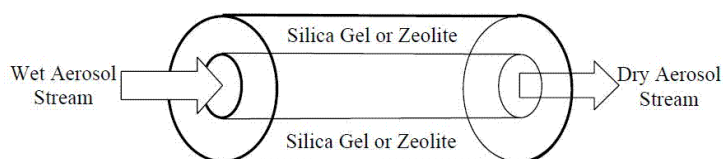


**Figure 2.4:** Diffusion Dryer Diagram

### Desiccants

Silica gel, also known as silicon dioxide ( $\text{SiO}_2$ ), with an average pore size of  $24 \text{ \AA}$ . The desiccant has a strong affinity for moisture because of the large surface area that results from the interconnected pores. Moisture is attracted to the desiccant through adsorption and capillary condensation. Although moisture can be adsorbed up to temperatures of  $220^\circ\text{F}$  ( $105^\circ\text{C}$ ), silica gel is most efficient at room temperatures ( $70^\circ$  to  $90^\circ\text{F}$ ) and high humidity (60 to 90% RH). The type of silica gel used in the production of aerosols is called indicating silica gel. Indicating silica gel is washed with cobalt chloride to give the desiccant a deep blue color when it is dry. The silica turns to a pink color as it becomes saturated with moisture, typically around 8% water by weight.

Molecular sieves, or synthetic zeolite, are porous crystalline aluminosilicates that possess strong affinity for water molecules. Due to the uniformity of zeolite's pore size (most commonly 4 Å), they do not release moisture into the system as readily as silica gel when subjected to an increase in temperature. Zeolite is also preferred over silica gel as a desiccant because it adsorbs moisture more strongly than silica gel due to the higher heat of adsorption for water, which is a sum of the latent heat of vaporization of water and heat of wetting.

### **Scanning Mobility Particle Sizer**

A scanning mobility particle sizer (SMPS) is a system consisting of an electrostatic classifier and a condensation particle counter (CPC) that are used to quantify the particle size and concentration distributions of an aerosol stream after the stream passes through the diffusion dryers. The particle size of an aerosol stream is selected by a differential mobility analyzer (DMA), coupled with the electrostatic classifier, which produces a monodisperse aerosol. The SMPS generates a size distribution by scanning the electrostatic classifier with a series of size bins. The CPC determines the concentration of particles in each bin.

Within the SMPS system, there exists an electrostatic classifier, differential mobility analyzers, and a condensation particle counter. These instruments are described in the following sections.

### **Electrostatic Classifier**

Once aerosols are created using the atomizer and exit the series of five dryers, the polydisperse particles enter into a TSI Model 3080 electrostatic classifier (EC) that is coupled with a differential mobility analyzer (DMA) to produce monodisperse particles. An image of an EC is shown in Figure 2.5. The polydisperse aerosol stream enters the EC through an impactor which removes particles of a larger size by inertial impaction. Particle charges are then neutralized by a radioactive isotope (Kr-85) which produces high concentrations of bipolar ions. These ions and particles collide by random motion to allow charge equilibrium to be reached quickly. The flow rates and voltage of the EC are controlled parameters. A DMA then separates particles based on the particle's electrical mobility, which allows for a collection of a specific size range of particles.

As seen in Figure 2.5, the polydisperse (non-uniform size, shape or mass) aerosols pass through the bipolar charger, which establishes a charge equilibrium using the radioactive isotope. The particles receive either positive, negative or zero charge(s) before entering the DMA.

### **Differential Mobility Analyzer**

After receiving a charge from the electrostatic classifier, the particles enter a long DMA where particles with a negative charge are attracted to the outer electrode, non-charged (neutral) particles are removed by excess flow and positively charged

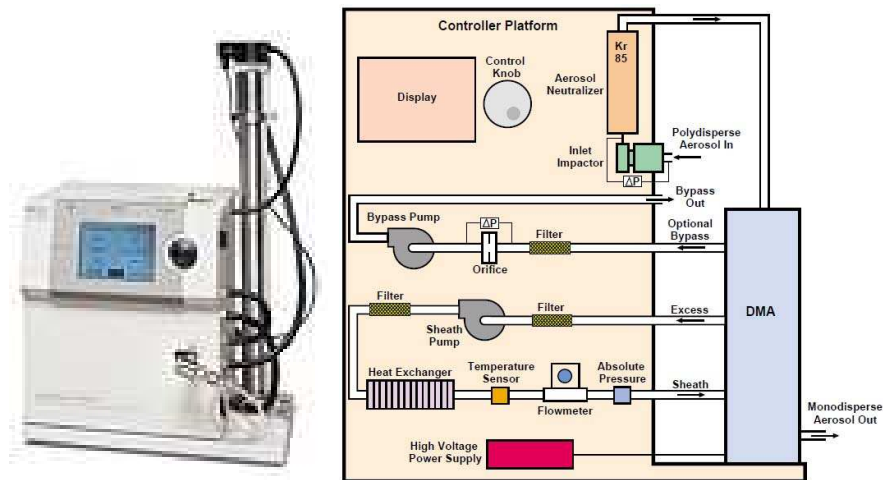


**Figure 2.5:** Electrostatic Classifier

(<http://www.tsi.com> and TSI Model 3080-Series Electrostatic Classifiers Spec Sheet)

particles are attracted to the center of the electrode. Only the particles within a specified range of electrical mobility exit the DMA as monodisperse (uniform size, shape, and mass) flow, as shown in Figure 2.6.

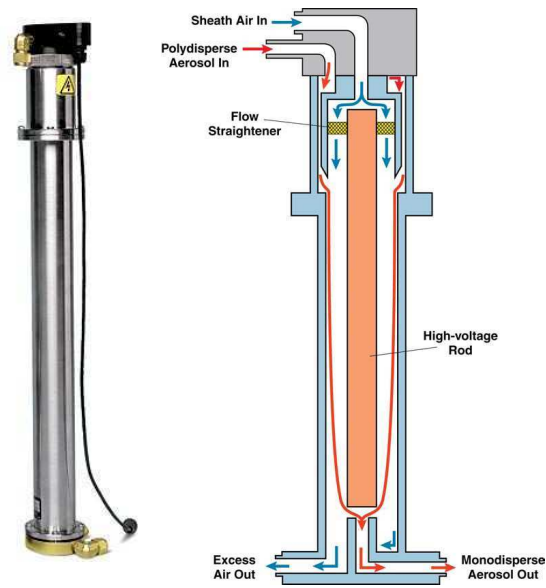


**Figure 2.6:** Differential Mobility Analyzer  
(<http://www.tsi.com>)

For this study, two long DMAs (TSI Model 2081) were used in series to form a hygroscopic tandem differential mobility analyzer (HTDMA) system. After the particles exit the DMAs, they entered a condensation particle counter (CPC) to form a scanning mobility particle sizer (SMPS) system.

### Condensation Particle Counter

A TSI Model 3775 condensation particle counter (CPC) (Figure 2.7) was used to detect the size distribution and concentration of aerosols in the electrostatic classifier. The CPC operates by heating 1-butanol to form a saturated vapor. Aerosols enter into the vapor and are passed through a condenser where the alcohol becomes

supersaturated. The aerosol particles act as condensation nuclei for the vapor and begin to swell until an optical detector senses the particle's presence.



**Figure 2.7:** Condensation Particle Counter (CPC)  
(<http://www.tsi.com>)

### 2.3.1 Hygroscopic Tandem Differential Mobility Analyzer System

The hygroscopic tandem differential mobility analyzer (HTDMA) system uses all of the equipment described above. A detailed schematic of the HTDMA system is depicted in Figure 2.8. To summarize, aerosols are generated from solution, dried through a series of driers and size selected by a differential mobility analyzer (DMA). The flow then continues through a series of Nafion tubing that alters and controls the relative humidity of the stream, which hygroscopically grows the particles into aerosols. Post-growth, the flow enters the second DMA and a CPC to complete the scanning mobility particle sizer (SMPS) system.

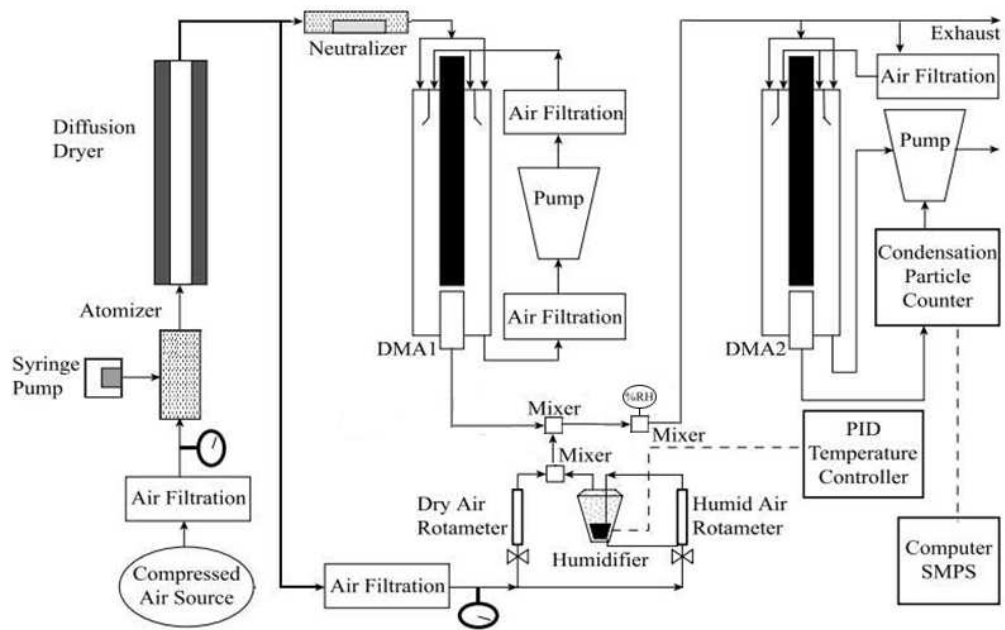


**Figure 2.8:** HTDMA experimental setup

For this study, the HTDMA was used extensively to investigate the hygroscopic properties of aerosols under 100 nm in diameter. Morphological effects were also rationalized based on these results.

### 2.3.2 Vibrating Orifice Aerosol Generator System

The HTDMA system is useful for generating and analyzing particles less than 100 nm in size. In order to produce monodisperse particles that are larger than 1  $\mu\text{m}$ , a TSI Model 3450 Vibrating Orifice Aerosol Generator (VOAG) was used. The VOAG uses a vibrating orifice to control the breakup of a liquid jet, which enables the VOAG to

produce uniform droplets with a standard deviation of  $<1\%$  of the mean droplet size (Figure 2.9).

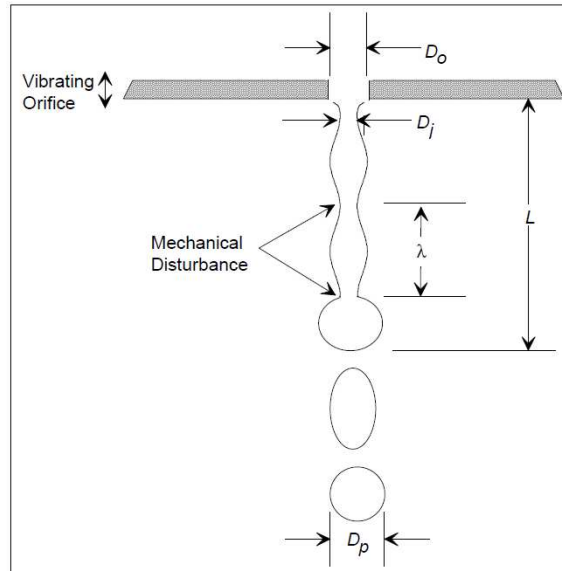


**Figure 2.9:** Vibrating Orifice Liquid Jet Breakup (VOAG Manual)

A syringe pump is set to a predetermined, constant volumetric flow rate to feed a liquid stream to the vibrating orifice. The orifice is set to an oscillation operating frequency which regulates how the jet is broken up. Once the droplets are formed, they travel up a column of dry air, which evaporates the volatile portion of the droplets, leaving a dry particle to be collected. The liquid flow rate, dispersion air, dilution air, and oscillation frequency are controlled by the user. Using the liquid flow rate ( $Q$ ), oscillation frequency ( $f$ ) and the volumetric concentration of the solution ( $C$ ), the final theoretical particle diameter ( $D_p$ ) can be calculated:

$$Dp = \left( \frac{6QC}{\pi f} \right)^{1/3} \quad (2.1)$$

A diagram and holistic image of the VOAG are shown in Figure 2.10.

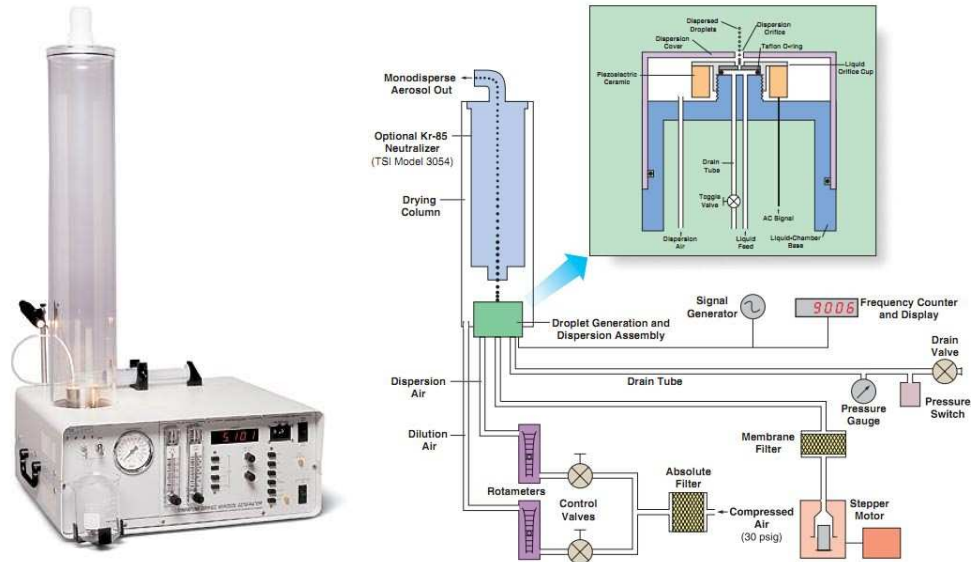


**Figure 2.10:** Vibrating Orifice Aerosol Generator  
(<http://www.tsi.com>)

For this study, a 60 mL syringe was used at a rate of  $4.2 \cdot 10^{-4}$  cm/s to produce a liquid feed rate ( $Q$ ) of 0.139 cc/min. The dilution rate was set to 45 lpm and the dispersion air was set at 1500 cc/min. The operating frequencies were calculated by multiplying 0.6 by the maximum operating frequency and ranged from 63 to 76 kHz. Once the particles were collected onto gold-coated steel or aluminum discs, the samples were viewed under a Scanning Electron Microscope (SEM) to ensure that well-dispersed, uniform particles were created from the parameters set on

the VOAG. Samples were then created to be viewed and analyzed under the Environmental Scanning Electron Microscope (ESEM) where a variable relative humidity chamber allowed for the quantitative growth of the aerosols.

It is important to note that the repeated use of organic acids, especially of high concentrations, can lead to corrosion of the system. This corrosion can cause defects in the orifice plate, as shown in Figure 2.11, and subsequent stream deformations.

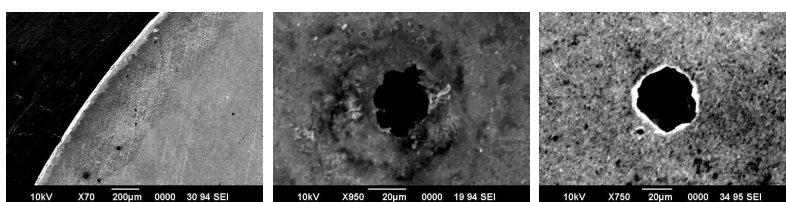


**Figure 2.11:** Effects of corrosion on vibrating orifice plates

The images above were taken with a Scanning Electron Microscope (SEM). To correct the issue of corrosion, brass fittings were replaced with stainless steel fittings and the instrument was flushed with three 60 mL syringes of pure isopropanol pre- and post-collection.

## 2.4 Aerosol Imaging and Analysis

### 2.4.1 Scanning Electron Microscope (SEM)

The Scanning Electron Microscope (SEM) was employed to ensure the correct VOAG settings and solution concentration were used and that the particles were favorable for imaging and hygroscopic analysis with respect to size range and concentration. It was expected that more concentrated solutions would yield larger particle sizes due to the increase in impaction. For this research, a JSM-6390 LV SEM, like the one in Figure 2.12, was utilized.



**Figure 2.12:** Scanning Electron Microscope  
(<http://www.jeol.com>)

The SEM is a type of electron microscope that uses a high-energy beam of elec-

trons to scan a surface to ultimately create an image. A traditional optical microscope uses lenses to bend light waves and these lenses are adjusted for focus. In the SEM, electromagnets are used to bend an electron beam to create an image. These electromagnets control the magnification and clarity of the image. A diagram of an SEM is shown in Figure 2.13.

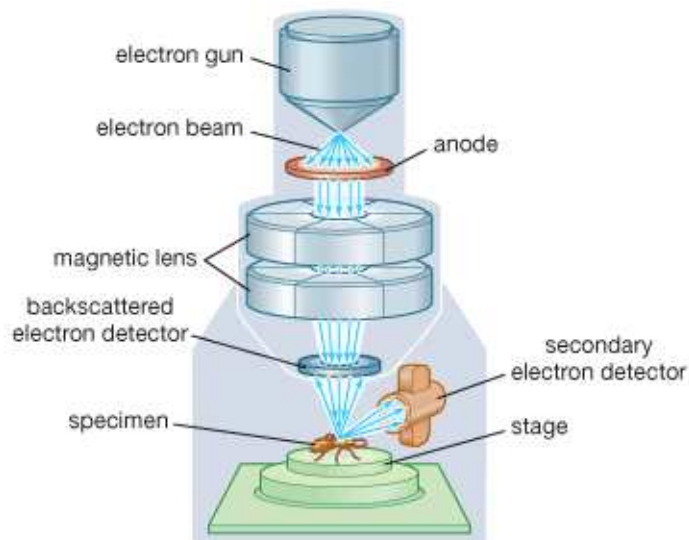


**Figure 2.13:** Scanning Electron Microscope  
(Encyclopedia Britannica)

A beam of electrons are produced at the electron gun by applying a voltage to heat a metallic filament, which functions as the cathode. For this instrument, tungsten hairpin filament was used. The electron beam follows a vertical path down through the column towards an anode. Some electrons hit the anode, while the majority of electrons pass down the column. As the electrons flow through the column, they pass through electromagnetic lenses which focus and direct the beam towards the stage

where the sample is held. Upon impact, some electrons are ejected as backscattered or secondary electrons. Backscattered electrons (BSEs) occur when electrons circle the nucleus and come out of the sample without slowing down. Backscatter electron detectors are often used to capture these electrons and form images from them. Since heavy elements (high atomic number) backscatter electrons more strongly than light elements (low atomic number), BSEs are used to detect contrast between areas with different chemical compositions. Secondary electrons are formed when impacting electrons interact with the sample. The impacting electrons repel the electrons of the sample atoms until the electrons of the sample are ejected. Since these electrons move slowly and are negatively charged, they can be attracted to a positively charged detector, which allows electrons to be captured from a wide area. The ability to pull in electrons from around corners is what results in 3-D secondary electron images and so, secondary electrons are most valuable for showing morphology and topography of samples. Once the electrons are collected, they are converted to a voltage that is amplified. The amplified voltage is then converted to an electrical signal that is used to create images.

### **2.4.2 Environmental Scanning Electron Microscope**

While the SEM operates under a vacuum to maximize the number of electrons that reach the sample surface, a high vacuum environment may cause samples of low volatility to evaporate and relative humidity changes cannot be attained at low pressures. The Environmental Scanning Electron Microscope (ESEM) operates under low pressure (1-50 Torr) and in the presence of certain non-corrosive gases, such as water

vapor. In order for the ESEM to produce images, it incorporates a pressure-limiting aperture below the objective aperture which maximizes the pressure in the chamber while minimizing the path that the electrons must follow through to reach the sample. The ESEM also utilizes differential pumping which protects the electron optics column from contamination of water vapor or particle fragments found in a higher pressure environment, as shown in Figure 2.14 [27].

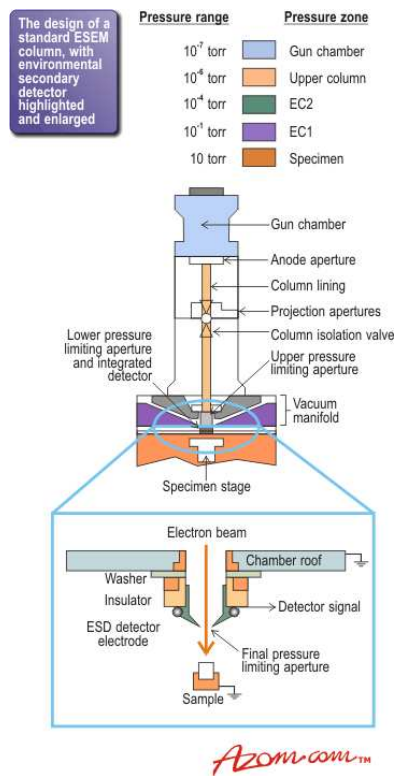


**Figure 2.14:** ESEM Diagram  
(<http://www.azom.com>)

The incident electron beam strikes the surface and then dissipates into the ionized gas, which is collected by the gaseous secondary electron detector (GSED). The gas

molecules in the chamber can also deflect secondary electrons back to the detector. It is for this reason that a higher chamber pressure can result in a higher contrast and resolution image. If the chamber pressure is too high, however, the gas molecules may prevent the incident beam from reaching the sample, resulting in a low contrast and resolution image. For this study, the hygroscopic analysis of the particles  $>2\mu\text{m}$  in diameter occurred with the FEI Quanta 400 Environmental Scanning Electron Microscope. Since water vapor was the gas of interest in this study, the relative humidity of the sample had to be well-controlled. To accomplish this, a Peltier stage with temperature control held the sample. The maximum operating range of the Peltier stage is  $-25^\circ\text{C}$  to  $50^\circ\text{C}$ . Using the temperature, the saturation vapor pressure of water can be determined using this 6th order polynomial as published by Ficke and Lowe [28]:

$$p_w^o(\text{mbar}) = a_o + a_1T + a_2T^2 + a_3T^3 + a_4T^4 + a_5T^5 + a_6T^6 \quad (2.2)$$

where the temperature is in  $^\circ\text{C}$  and the constants are given as:

$$\begin{aligned} a_o &= 6.107799961 \\ a_1 &= 4.436518521 \cdot 10^{-1} \\ a_2 &= 1.428945805 \cdot 10^{-2} \\ a_3 &= 2.650648471 \cdot 10^{-4} \\ a_4 &= 3.031240396 \cdot 10^{-6} \\ a_5 &= 2.034080948 \cdot 10^{-8} \\ a_6 &= 6.136820929 \cdot 10^{-11} \end{aligned}$$

Through calculating the saturation vapor pressure and knowing that the relative humidity is the ratio of the water vapor pressure to the saturation vapor pressure, the following table of data could be formulated. The water vapor pressure of interest to this study was between 2.00 and 7.00 torr and so, Table 2.2 was created for these pressures.

**Table 2.2:** RH(%) Ranges with propagated uncertainties for five sample temperatures

| Temperature ( $^{\circ}C$ ) | RH(%) Range                      |                                  |
|-----------------------------|----------------------------------|----------------------------------|
|                             | $P = 2.00 \pm 0.01(\text{torr})$ | $P = 7.00 \pm 0.01(\text{torr})$ |
| $4.0 \pm 0.5$               | $32.8 \pm 0.6$                   | $114.8 \pm 1.9$                  |
| $5.0 \pm 0.5$               | $30.6 \pm 0.5$                   | $107.0 \pm 1.6$                  |
| $15.0 \pm 0.5$              | $15.6 \pm 0.1$                   | $54.8 \pm 0.4$                   |
| $20.0 \pm 0.5$              | $11.4 \pm 0.1$                   | $39.9 \pm 0.2$                   |
| $30.0 \pm 0.5$              | $6.28 \pm 0.04$                  | $22.0 \pm 0.01$                  |

By holding the temperature of the ESEM constant while slowly increasing the pressure, the relative humidity of the ESEM chamber slowly increased. Once images were compiled over a range of RH, the ImageJ software was used to calculate growth factors.

# Chapter 3

## Results and Discussion - ESEM

### 3.1 Introduction

Aerosols affect the Earth's climate directly, by scattering and absorbing radiation, and indirectly, by serving as nuclei for cloud formation. Clouds control the reflection of solar radiation and the trapping of energy near the Earth and thus, control weather and climate changes. In fact, the uptake of water by atmospheric aerosols can strongly influence the light scattering efficiency [29; 30; 31; 32], cloud nucleating ability, and chemical reactivity [33] of the aerosols. In addition, the composition, size, and phase of the aerosols are complicated with these water interactions, which creates more uncertainty in climate modeling. This study will serve to improve upon the paucity of data available for the modeling particles greater than  $2 \mu\text{m}$  in diameter.

Electrodynamic balances, infrared absorption cells, optical microscopy, and particle mobility analyzers have been extensively used to investigate hygroscopic growth of inorganic and organic aerosol particles in both field and laboratory settings [34]. While these techniques are useful for determining the DRH for particles, they fail to recognize any morphological changes that may occur. With the use of the ESEM, both hygroscopic and morphological data can be obtained through the *in-situ* growth of particles of known composition.

Past studies of chemical speciation has revealed significant concentrations of sulfate, nitrate, and chloride anions; sodium, ammonium, and calcium cations; and innumerable organic species [35; 36]. Such studies have also shown higher concentrations of low carbon-number dicarboxylic acids when measuring water-soluble organic carbon (WSOC) [7; 37; 38]. Past ESEM usage has been performed primarily on atmospherically relevant inorganic compounds (e.g. sodium chloride, ammonium sulfate). However, this study will be expanded to include other inorganic compounds, as well as two common organic compounds, as listed in Table 3.1.

**Table 3.1:** Physical Properties of Chemical Species at 25°C

| Compound          | MW<br>(g/mol) | Density <sup>a</sup><br>(g/cm <sup>3</sup> ) | Solubility <sup>c</sup><br>in 100g water<br>(g)(25°C) | DRH<br>(%)                                                | GF<br>(85%RH)                         |
|-------------------|---------------|----------------------------------------------|-------------------------------------------------------|-----------------------------------------------------------|---------------------------------------|
| Ammonium Chloride | 53.492        | 1.519                                        | 35.1                                                  | 76.5-77.3 <sup>d</sup> , 78.5 <sup>a</sup>                | -                                     |
| Ammonium Sulfate  | 132.141       | 1.77                                         | 70.4                                                  | 79.0 <sup>e</sup> , 81.3 <sup>d</sup> , 79.8 <sup>f</sup> | 1.49 <sup>e</sup> , 1.54 <sup>g</sup> |
| Calcium Chloride  | 110.983       | 2.15                                         | 72.3                                                  | 19-24 <sup>d</sup> , 28.1 <sup>a</sup>                    | 1.54 <sup>h</sup>                     |
| Sodium Chloride   | 58.443        | 2.17                                         | 32.3                                                  | 74-76 <sup>d</sup> , 75.0 <sup>e</sup>                    | 2.1 <sup>e</sup>                      |
| Glutaric Acid     | 132.116       | 1.429 <sup>(15°C)</sup>                      | 151.1 <sup>(24°C)<sup>b</sup></sup>                   | 88.9 <sup>g</sup> , 85 <sup>e</sup>                       | 1.0 <sup>g</sup> , 1.09 <sup>i</sup>  |
| Malonic Acid      | 104.062       | 1.619 <sup>(10°C)</sup>                      | 163.7 <sup>(24°C)<sup>b</sup></sup>                   | 71.9 <sup>g</sup> , 65.2 <sup>i</sup> , 72.1 <sup>j</sup> | 1.40 <sup>i</sup> , 1.32 <sup>g</sup> |

<sup>a</sup> CRC Handbook of Chemistry and Physics, 86th Ed.

<sup>b</sup> Brooks *et al.* (2002) - Bulk solution measurements (24°C)

<sup>c</sup> International Critical Tables (Interpolated)

<sup>d</sup> Cohen *et al.* (1987) - EDB Study

<sup>e</sup> Cruz and Pandis (2000) - TDMA Study

<sup>f</sup> Ebert *et al.* (2002) - ESEM Study at 5°C and extrapolated to 25°C

<sup>g</sup> Wise *et al.* (2003) - Bulk Solution Measurement Study at 24.7-24.9°C

<sup>h</sup> Chen and Grace Lee (1998) - TDMA Study

<sup>i</sup> Peng, Chan and Chan (2001) - EDB and Bulk Measurement Study

<sup>j</sup> Parsons *et al.* (2004) - Optical Microscope / Flow Cell Study at Multiple Temperatures

## 3.2 Experimental

Hygroscopic experiments were conducted using a FEI Quanta 400 ESEM located in the O'Leary Center at Bucknell University. The investigated species and their respective physical properties were tabulated in Table 3.1. The sources and purities for each species were tabulated in Table 2.1.

Concentrated solutions ranging from 5 g/L to 20 g/L were created for each of the compounds and 2-10  $\mu\text{m}$  particles were generated using the vibrating orifice aerosol generator (VOAG). Each species was dissolved using 18.2 M $\Omega$ -cm resistivity ultra-pure water generated from the Millipore, Inc. purification system. This ultra-pure water also contained less than 20 ppb of total organic carbon. The use of ultra-pure water is extremely important for these studies as even small amounts of inorganics can strongly influence hygroscopic properties of aerosols [39].

Aerosols were generated for 30 minutes while filling the drying column. The aerosol stream was then shut down and the aerosols were collected via gravitational settling onto gold-coated discs for 1 hour. As the particles are not forced onto a substrate, this method is believed to best simulate how aerosols are collected from the atmosphere. Gold-coated discs were chosen as a substrate because the imaging of aerosols on a high-Z substrate yielded better imaging contrast than when copper or polypropylene was used [40]. Figure 3.1 illustrates the dispersion of  $\sim 10 \mu\text{m}$  malonic acid particles, as generated by the VOAG and captured by the ESEM.

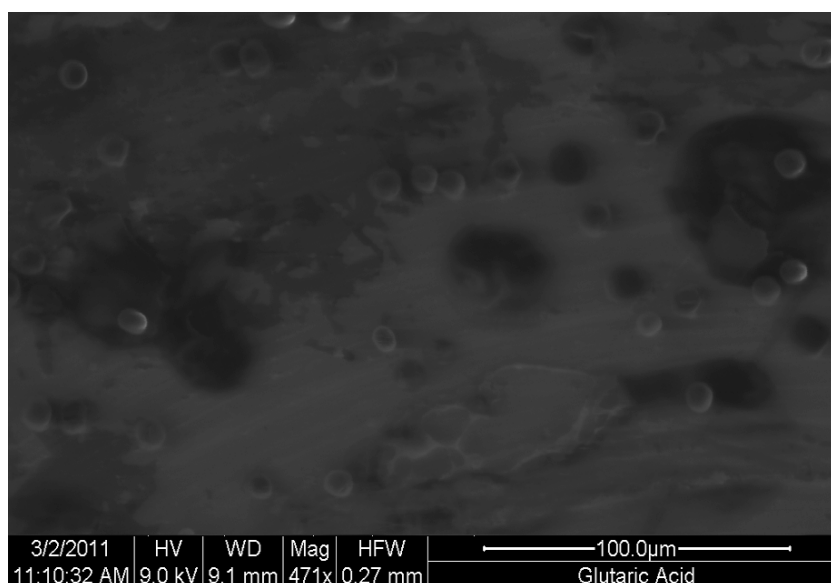


**Figure 3.1:** ESEM image of malonic acid dispersion

### 3.2.1 ESEM Operating Parameters

The ESEM was operated with a gaseous secondary electron detector (GSED). The chamber purge settings were customized to prevent the sample from being subjected to high relative humidities while the system pumped down. The minimum purge pressure was set to 0.9500 torr and the maximum purge pressure was set to 5.000 torr while at 30°C, approximately 3% and 15% RH, respectively. Beam voltages were kept under 10 kV, as any voltage higher than 10 kV caused sample damage. A spot size of 3.0 was also used at a working distance between 5 and 10 mm. The average magnification was around 10,000x, where inorganics were viewed at higher magnifications and organics were viewed under lower magnifications.

A Peltier stage pumped with cooling water was used to control the temperature

of the chamber. This temperature was kept around 30°C during pumping, purging and venting to prevent the samples from being subjected to a high relative humidity. Once the system was in ESEM mode, the temperature was lowered to the operating temperature (4°C) while the chamber was held at 1.00 torr.

Since a change in temperature had a more difficult method of control due to fluctuations from the PID controller, the temperature of the chamber was held constant while the pressure was slowly increased to increase the relative humidity environment. 5-20 minutes were allocated to each change in pressure to allow the sample to equilibrate with its surroundings. To minimize sample-beam interactions, the beam was blanked between each view of the sample. Each of the samples viewed underwent deliquescence only once.

### 3.2.2 ESEM Analysis

Electron micrographs at varying levels of relative humidity were provided by the ESEM and NIH's ImageJ software (version 1.44, available at <http://rsbweb.nih.gov/ij/>) was used to analyze the images. Initial attempts at using the software were to measure the particle areas and from the area, derive an effective diameter of the droplet using:

$$d_{p,wet} = \left[ \frac{8}{\sqrt{\pi^3}} \left[ A_{wet}^{3/2} + \frac{\rho}{s} (A_{dry}^{3/2} - A_{wet}^{3/2}) \right] \right]^{1/3} \quad (3.1)$$

which correlates a circular area to a spherical volume. The solubility is denoted as  $s$ , density as  $\rho$ , area of the wet particle as  $A_{wet}$ , and area of the dry particle as  $A_{dry}$ . Complications with this equation arise when any amount of spreading occurs on a substrate. Because only a top-down view is generated from the ESEM and unless a surface is perfectly hydrophobic to ensure no spreading occurs, an aerosol will appear to have a larger volume than in reality. This larger volume would translate to a larger calculated particle diameter and seemingly more active growth. In addition to complications with volume calculations, the software appeared to have difficulties with the resolution of the images. Thus, ImageJ was, instead, used to directly measure the diameters of the particles. More elaborate attempts were made with the software to calculate areas for amorphous particles.

While most studies are performed between 20-25°C, the ESEM analysis in this study was performed at 4°C. To compare the DRH values for different temperatures, the correlation given by Tang and Munkelwitz (1993) was used:

$$\ln \left( \frac{\%DRH(T)}{\%DRH(T^*)} \right) = \left( \frac{\Delta H_s}{R} \right) \left[ A \left( \frac{1}{T} - \frac{1}{T^*} \right) - B \ln \frac{T}{T^*} - C (T - T^*) \right] \quad (3.2)$$

where %DRH(T) is the deliquescence relative humidity at temperature T, %DRH(T\*) is the deliquescence relative humidity at another temperature T\*,  $\Delta H_s$  is the enthalpy of solution, and R is the gas constant. A, B, and C are constant coefficients of a 2<sup>nd</sup> order polynomial fit of solubility, n, to temperature. Solubility is expressed in moles of solute per mole of water.

$$n = A + BT + CT^2 \quad (3.3)$$

The parameters for Equations 3.2 and 3.3 are listed in Table 3.2, as compiled by Moore (2006).

**Table 3.2:** Thermodynamic and Solubility Data of Investigated Species

| Compound          | $\Delta H_s$ at<br>$25^\circ C$      | Solubility<br>Parameters |           |           | Solubility Data<br>References |
|-------------------|--------------------------------------|--------------------------|-----------|-----------|-------------------------------|
|                   |                                      | A                        | B         | C         |                               |
| Ammonium Chloride | 14.0 <sup>a</sup>                    | 0.02731                  | -6.804E-4 | 3.466E-6  | a                             |
| Ammonium Sulfate  | 6.4 <sup>a</sup> , 6.32 <sup>b</sup> | 0.1149                   | -4.489E-4 | 1.385E-6  | b                             |
| Calcium Chloride  | -56 <sup>a</sup>                     | 1.318                    | -9.894E-3 | -9.894E-3 | a                             |
| Sodium Chloride   | 1.88 <sup>b</sup>                    | 0.1805                   | -5.310E-4 | 9.965E-7  | b                             |
| Glutaric Acid     | 22.6 <sup>a*</sup>                   | 7.329                    | -5.599E-2 | 1.075E-4  | c                             |
| Malonic Acid      | 18.8 <sup>a*</sup>                   | 3.751                    | -2.782E-2 | 5.418E-5  | d                             |

\* enthalpy of solution at infinite dilution; all others at lowest reported dilutions

<sup>a</sup> International Critical Tables, 1st Electronic Edition

<sup>b</sup> Tang and Munkelwitz (1993)

<sup>c</sup> Stephen and Stephen (1963)

<sup>d</sup> Apelblat and Manzurola (1987)

### 3.3 Results and Discussion

The Aerosols Inorganic Model (AIM), the Gibbs Free Energy Minimization (GFEMN) model and the UNiversal Functional Activity Coefficient (UNIFAC) thermodynamic models have been applied to experimental data. AIM, as developed by Clegg, Brimblecombe and Wexler, provides thermodynamic models for gas/liquid/solid equilibrium and accounts for the temperature of the system, component ions involved and interactions of the ions over the span of specified relative humidity. GFEMN is a thermodynamically theoretical model and has been used previously for PM<sub>2.5</sub>, or fine particles. GFEMN, as referenced by Khlystov *et al.* (2005), was used as a secondary literature reference for ammonium sulfate.

UNIFAC is a semi-empirical model for predicting activity of non-ideal solutions [45]. This model uses the interaction of functional groups of a component, as well as binary interaction coefficients, to determine the activity coefficients of the mixture and the liquid equilibria information. Equations used to derive the UNIFAC model are explained in Appendix A.

Horizontal error bars show the propagated uncertainties for temperature and pressure measurements, as set by the user. Vertical error bars show one standard deviation of the mean growth factor between particles at the same RH. Other sources of error were associated with particle-beam interactions in the ESEM and uncertainty with imaging analysis.

### 3.3.1 Ammonium Sulfate

Ammonium sulfate and sodium chloride are the best characterized inorganics in both experimental and theoretical work. The hygroscopic growth of four ammonium sulfate aerosols ranging in size between  $5 \mu\text{m}$  and  $8 \mu\text{m}$  was characterized by ESEM for this study. Using the equation by Tang and Munkelwitz (1993) for the temperature dependence of DRH and the thermodynamic and solubility data for ammonium sulfate, a temperature decrease from  $25^\circ\text{C}$  to  $4^\circ\text{C}$  results in a theoretical increase in DRH by 1.6%.

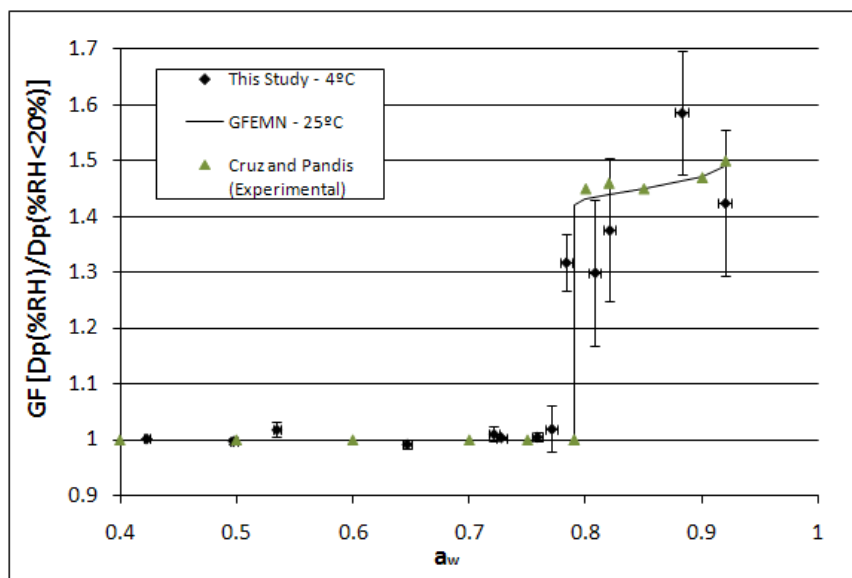


**Figure 3.2:** Hygroscopic growth curves for ammonium sulfate

Ammonium sulfate observed full deliquescence at 80% relative humidity, which was  $\sim 1\%$  higher DRH than predicted by GFEMN. As can be seen from Figure 3.2, deliquescence initially occurred approximately 2% lower than that predicted by models

(77%), but was not considered to fully deliquesce until 80%. Deliquescence is observed under a microscope and thus, morphological changes can be seen on a smaller scale before the bulk of an aerosol stream would detect the change. The DRH can then be inferred to occur at the onset of water uptake, rather than full deliquescence. The GFEMN model was created for particles under  $2.5 \mu\text{m}$ , which may explain why the growth in this experiment for particles greater than  $2 \mu\text{m}$  was greater than that of the model. Error in the growth factors increased with increasing relative humidity because as water adsorbed to the particle, the edge of the particle began to disappear into the substrate, as can be seen in Figure 3.3.



**Figure 3.3:** Ammonium sulfate at 11%, 54%, 78% and 92%RH, respectively

### 3.3.2 Ammonium Chloride

The hygroscopic properties of ammonium chloride have also been well-characterized at  $25^\circ\text{C}$ , although less than that of ammonium sulfate or sodium chloride. According to the equation provided by Tang and Munkelwitz (1993), it was calculated that a decrease in temperature from  $25^\circ$  to  $4^\circ\text{C}$  would result in an increase of DRH by 3.2%. For this study, three ammonium chloride particles between  $3$  and  $7 \mu\text{m}$  were analyzed.

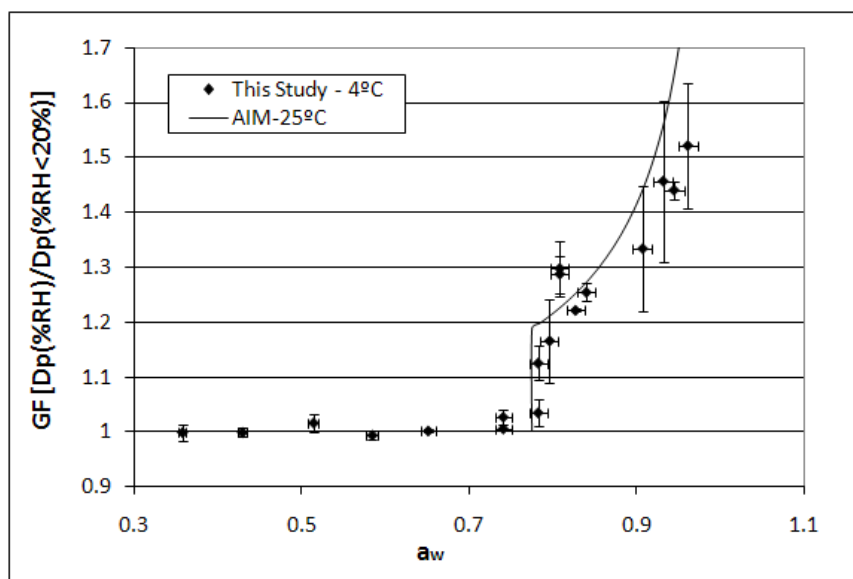


**Figure 3.4:** Hygroscopic growth curves for ammonium chloride

As can be seen from Figure 3.4, ammonium chloride was another inorganic compound that underwent deliquescence. While the Aerosol Inorganics Model predicted a DRH of 77%, experimental DRH values ranged from 77% to 79% with respective error bars. Figures 3.4 and 3.5 depict how ammonium chloride did not experience as much growth compared to other inorganics with similar properties, which was predicted by AIM. Once 93% RH was reached, the particle could not be discerned from the substrate and as a result, growth factors could not be calculated.

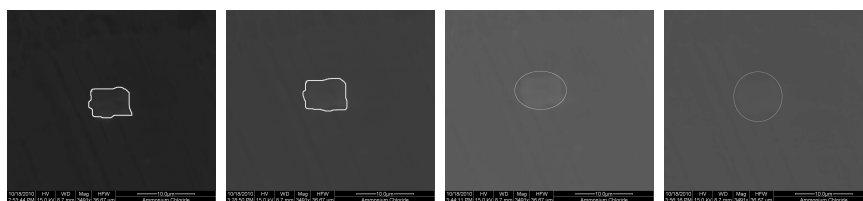


**Figure 3.5:** Ammonium chloride at 7.8%, 74.1%, 80.9% and 90%RH, respectively. It should be noted the 7.8% and 90% images were at a lower magnification.

### 3.3.3 Calcium Chloride

It is well known that calcium chloride grows hygroscopically with a very smooth growth curve with increasing RH [46]. Four calcium chloride particles were created that ranged in size from 5 to 8  $\mu\text{m}$ .

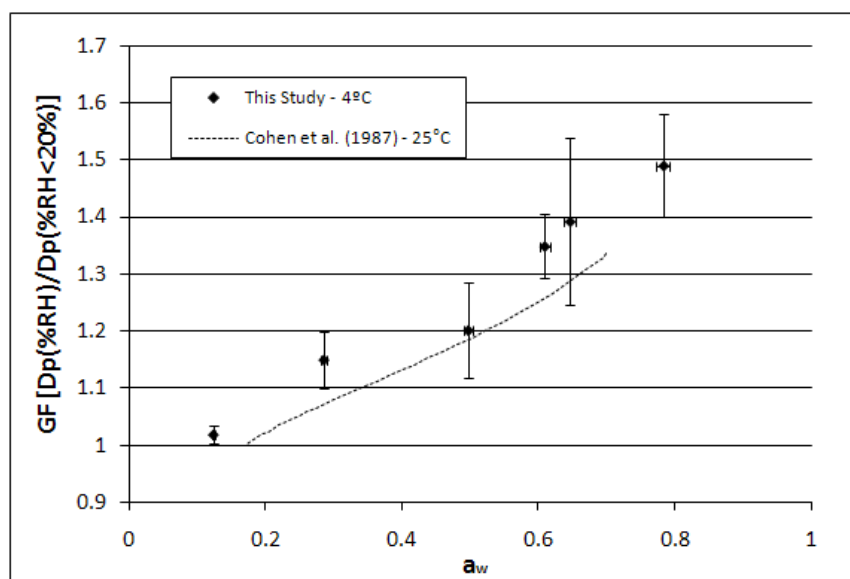


**Figure 3.6:** Hygroscopic growth curves for calcium chloride

Calcium chloride is a unique inorganic compound in that it grew hygroscopically, rather than experiencing deliquescence. This behavior was expected as calcium chloride is used commercially as a desiccant due to its affinity for water. Although past bulk measurement studies have shown calcium chloride to be hygroscopic, there is still debate as to whether the component is ever dry in atmospheric environments. In a study performed by Cohen *et al.* (1987), hygroscopic growth was performed on an electrodynamic balance at 25°C and it was concluded that calcium chloride never exists in crystalline form. The electron micrographs from this study (Figure 3.7) illustrate how the edges of the particle became rounded as water uptake occurred, even at relative humidities 10%. Large errors bars are associated with particle growth at higher relative humidities as the particle edges were difficult to determine against the background.

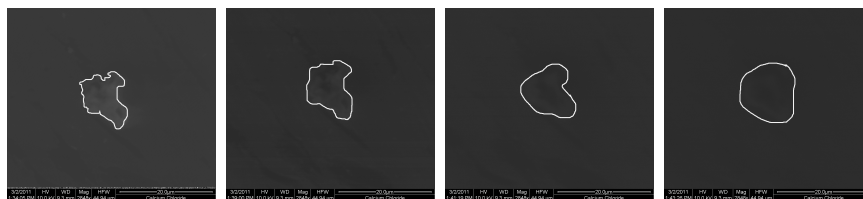


**Figure 3.7:** Calcium chloride particle at 10.3%, 51.2%, 65.4% and 79.9%RH, respectively

### 3.3.4 Sodium Chloride

The study of sodium chloride, although previously well-analyzed, is important for several reasons. First of all, sodium chloride is a principle component in sea salt and is ubiquitous in the atmosphere. Secondly, as its hygroscopic properties are

well-known, sodium chloride acts as a great base study for comparison to literature sources and other components in this study. Lastly, the DRH of sodium chloride does not have a strong temperature relationship and can thus be compared to studies performed at varying temperatures. Seven 3-10  $\mu\text{m}$  sodium chloride particles were created and analyzed using ESEM. According to the Tang and Munkelwitz (1993) correlation, a decrease in temperature from 25° to 4°C would result in an increase of DRH by only 0.8%.

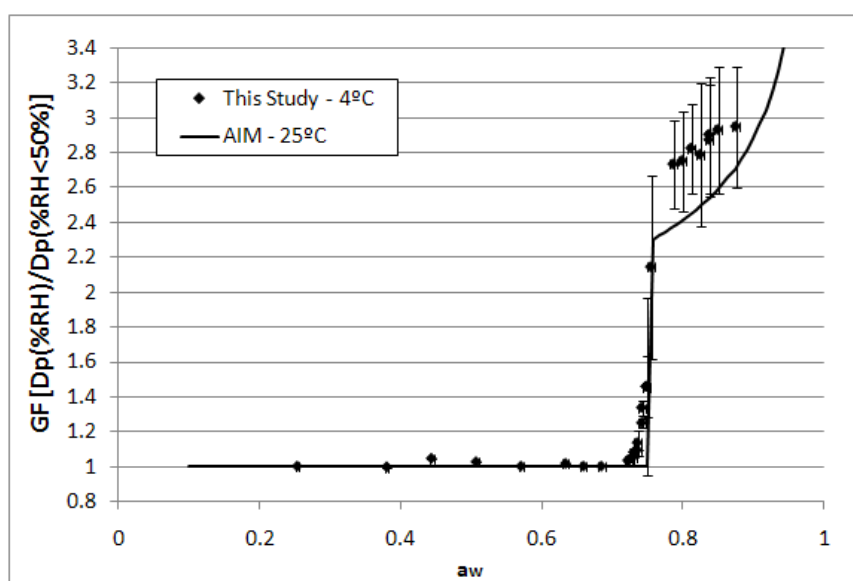


**Figure 3.8:** Hygroscopic growth curves for sodium chloride

Although sodium chloride has been studied extensively, these ESEM results produced new information. The DRH for NaCl has been repeatedly reported as 75-77%. However, the particles clearly begin water uptake as low as 73% RH, as verified by Figures 3.8 and 3.9, due to the strong adsorption of water onto the crystal surface prior to droplet formation. As per the electron micrographs, the edges of the cubic

particles begin to round out as a result of water adsorption. Full deliquescence can be interpreted as  $\sim 75\%$ , which is consistent with previous bulk aerosol measurements.

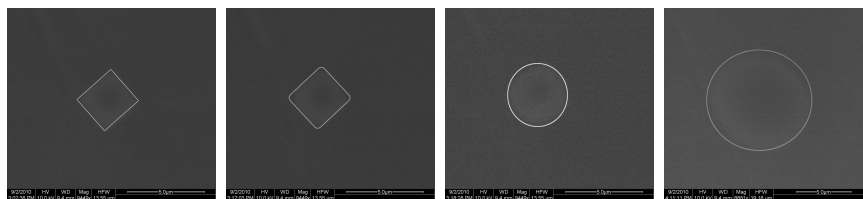


**Figure 3.9:** Sodium chloride particle at 38%, 74%, 75% and 96.5%RH, respectively

### 3.3.5 Glutaric Acid

Glutaric acid is another ubiquitous component of the atmosphere and consequently, has been well studied. For this study, values were compared to AIM and thermodynamic UNIFAC models. A decrease in temperature from  $25^{\circ}$  to  $4^{\circ}\text{C}$  theoretically results in an increase of DRH by 4.9%. Three 2-6  $\mu\text{m}$  particles of glutaric acid were analyzed using the ESEM.

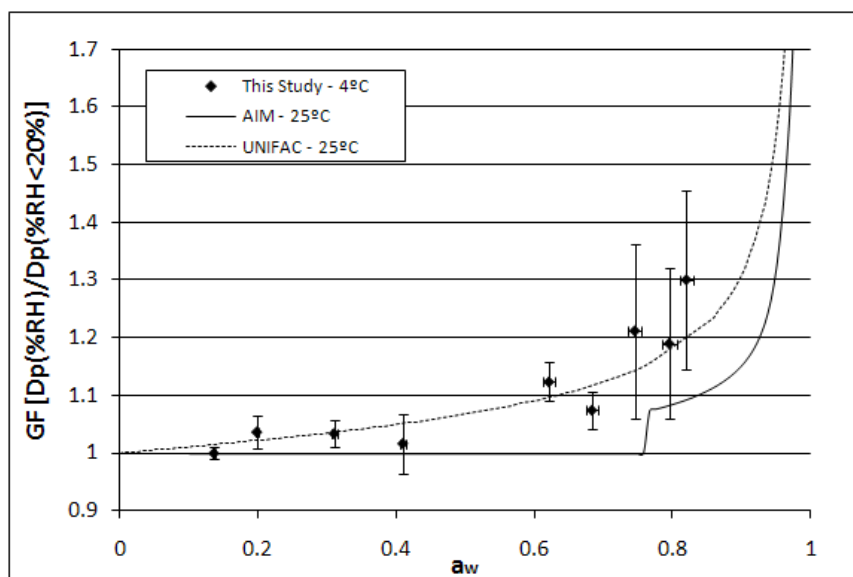


**Figure 3.10:** Hygroscopic growth curves for glutaric acid

Organic compounds have a propensity to form hydrogen groups, and thus, tend to be hydrophilic. The greater the affinity of a particle for water, the more difficult it becomes to form images at high RH. It is because of this phenomenon that images above 82% were unable to be analyzed for particle growth and images around 70% had large error associated with them. As glutaric acid experienced hygroscopic behavior, a DRH could not be determined.



**Figure 3.11:** Glutaric acid particle at 40%, 60%, and 82%RH, respectively

### 3.3.6 Malonic Acid

Malonic acid has been reported to exhibit hygroscopic growth [47]. Three malonic acid particles ranging in size from 4 to 7  $\mu\text{m}$  were analyzed in the ESEM.

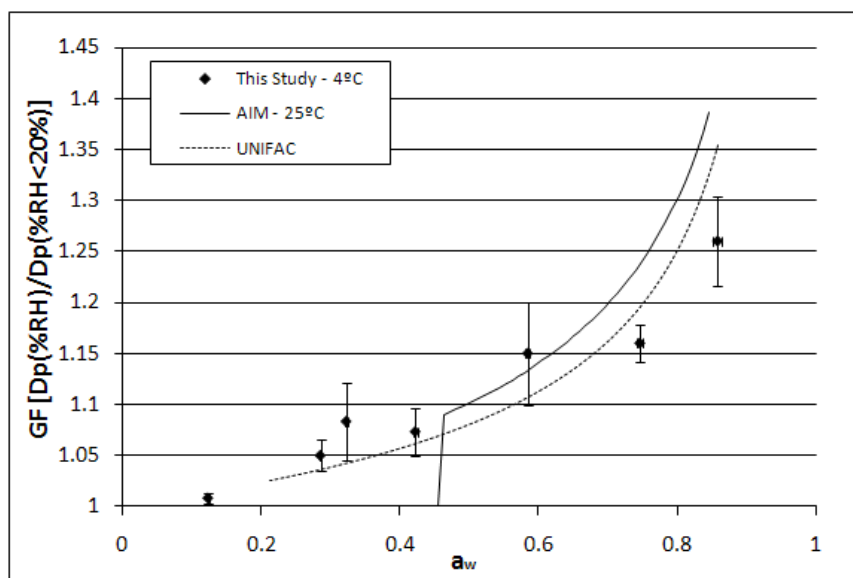


**Figure 3.12:** Hygroscopic growth curves for malonic acid

Although AIM predicted a DRH around 46% RH, this study resulted in hygroscopic growth of malonic acid due to the particles already having water adsorbed to the surface. However, the experimental equilibrium growth was consistent with that theorized by the models. As with glutaric acid, the image contrast for malonic particles at high RH (80%) was not high enough for analysis. This decrease in contrast has been attributed to water adsorption close to the hydrophilic particles, which can deflect incident and dispersed electrons so the detector cannot produce a proper image.

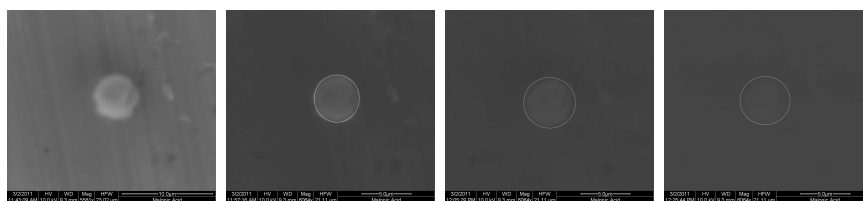


**Figure 3.13:** Malonic acid particle at 9%, 29%, 45%, and 79%RH, respectively

### 3.3.7 Summary

Overall, the hygroscopic growth of components in this study were consistent with that by published literature. In some cases, the experimental DRH was higher than that of other studies, which can be explained by the temperature-dependence of the component. In the case of sodium chloride, the DRH was lower than expected due to earlier onset of water adsorption, which was seen in the ESEM, but is not quantified in bulk measurement studies. Ammonium sulfate experienced both initial growth before that of the reported DRH and continued to grow at a value higher than the reported DRH.

The main complications from this system occurred at higher relative humidity environments within the microscope when imaging and subsequent analysis became difficult due to the hydrophilic nature of certain particles. As water uptake increased, it became more difficult to discern the particle edge from the substrate. Thus, organic acids and strongly hydrophilic components were difficult to image and analyze at these levels.

## Chapter 4

# Results and Discussion - HTDMA

### 4.1 Introduction

Organic aerosols are ubiquitous in the atmosphere, requiring that their role be accounted for in aerosol-water interactions and ultimately, climate models. According to Kanikidou *et al.* (2005), 90% of total tropospheric aerosol mass can be attributed to organic species and White reported that organics constitute 20-50% of fine aerosol mass over the continental United States. Out of the total tropospheric organic aerosols, up to 50% has been reported to be polycarboxylic acids [50; 13], although aerosols can contain mixtures of both organic and inorganic components. Low molecular weight dicarboxylic acids are expected to exist most prevalently in atmospheric aerosols. Unlike their inorganic counterparts, these aerosol-water interactions have not been well characterized [47] and generally exist as complex mixtures.

As dicarboxylic acids have a tendency to form hydrogen bonds, the organic species are hydrophilic and favorably water soluble.

In this study, five inorganic species and eight dicarboxylic acids plus their complex mixtures were examined to determine their deliquescence and hygroscopic growth properties. Pure components and mixtures were studied to model more realistic atmospheric environments.

## 4.2 Experimental

The instrumentation involved with the hygroscopic tandem differential mobility analysis (HTDMA) was described in Section 2.3. The humidification system was built from laboratory materials, including Nafion tubes for the membranes and a mixing tank to ensure proper mixing of the aerosols and the humidified air stream. The species investigated include sodium chloride, calcium chloride, ammonium chloride, ammonium sulfate, ammonium nitrate, adipic acid, aspartic acid, azelaic acid, maleic acid, malonic acid, phthalic acid, succinic acid, and tartaric acid. The chemical structures of the organic species are outlined in Table 4.1. Complex mixtures of organic species were also created, as described in Table 4.2. The hygroscopic results are also summarized in Table 4.2.

Solutions were made using ultra-purified water generated by a Millipore, Inc. water purification system that purified the water to a resistivity of 18.2 M $\Omega$ -cm and less than 20 ppb total organic carbon. Solutions were made to a concentration of 1

g/L and mixtures were made with equal mass percents of each component. The hygroscopic properties of sodium chloride and ammonium sulfate have been extensively reported and thus, these components were used to verify the experimental set-up and technique.

The precision of the scanning mobility particle sizing system (SMPS) is estimated to be  $\pm 2$  nm. The Vaisala humidity and temperature probes are accurate to within  $\pm 1\%$  RH (0-90%RH),  $\pm 2\%$  RH (90-100%RH), and  $\pm 0.1^\circ\text{C}$ . Relative humidities were increased from below 20% to over 80% and temperature readings remained fairly constant at 23-25°C.

First, a full size distribution for each trial was recorded to better understand the concentrations of the generated aerosols, as well as the arithmetic mean, median, mode, and geometric mean of the distributions (Appendix B). The arithmetic mean size is defined as the sum of the particle diameters over the number of particle diameters. The median is the absolute middle value of the data set and the mode is the most frequency observed value of the data set. The geometric mean is another statistical average generated by the HTDMA system and is defined by:

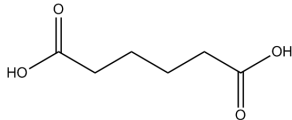
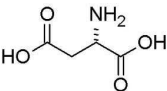
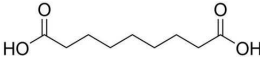
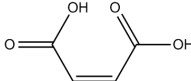
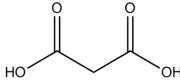
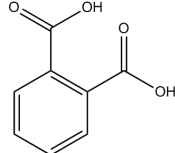
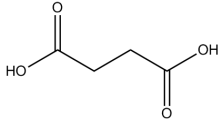
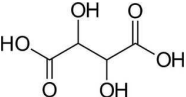
$$GM = \sqrt[n]{y_1 \cdot y_2 \cdot \dots \cdot y_n} \quad (4.1)$$

The geometric mean is generally used when working with percentages (which are derived from values), whereas the standard arithmetic mean is used with the values themselves. For this application, the bin size can constitute a percentage of the total

size and thus, the geometric mean can be applied.

Due to the experimental set-up of the humidification system, a wet air stream and an aerosol stream are mixed and the relative humidity of this mixture is controlled using a flow meter. It is due to using a flow meter that a higher initial concentration of aerosols must be selected, as the concentration of the dry aerosol stream slowly decreases with increasing relative humidity. For that reason, a diameter for size-selection was determined based on the corresponding concentration of the distribution (approximately  $6 \cdot 10^5$  particles/cc). Selected particle sizes ranged between 30 and 60 nm.

**Table 4.1:** Molecular Structures and Physical Properties of Studied Dicarboxylic Acids

| Compound         | Molecular Structure                                                                 | Density <sup>a</sup> (g/cm <sup>3</sup> ) | Solubility at 25°C (g/L) |
|------------------|-------------------------------------------------------------------------------------|-------------------------------------------|--------------------------|
| Adipic Acid      |    | 1.36                                      | 24.9 <sup>b</sup>        |
| DL-Aspartic Acid |    | 1.66                                      | 5.02 <sup>b</sup>        |
| Azelaic Acid     |    | 1.23                                      | 2.14 <sup>b</sup>        |
| Maleic Acid      |    | 1.59                                      | 78.0 <sup>b</sup>        |
| Malonic Acid     |    | 1.619                                     | 1260 <sup>b</sup>        |
| Phthalic Acid    |   | 1.59                                      | 1.0 <sup>b</sup>         |
| Succinic Acid    |  | 1.572                                     | 87.7 <sup>b</sup>        |
| L-Tartaric Acid  |  | 1.79                                      | 20.6 <sup>c</sup>        |

<sup>a</sup> CRC Handbook of Chemistry and Physics, 90<sup>th</sup> Ed. (2009).

<sup>b</sup> Apelblat and Manzurola (1987).

<sup>c</sup> Apelblat and Manzurola (1989).

### **4.3 Results and Discussion**

Hygroscopic properties of the pure organics and the mixtures based on literature and this study are listed in Table 4.2.

**Table 4.2:** Hygroscopic Data of pure component dicarboxylic acids and mixtures. Mixtures of organic species are of equal mass percent.

| Compound                                     | Pure %DRH (25°C)                                           | Mixture  |          |       |          |       |          |          |          |
|----------------------------------------------|------------------------------------------------------------|----------|----------|-------|----------|-------|----------|----------|----------|
|                                              |                                                            | A        | B        | C     | D        | E     | F        | G        | H        |
| Adipic Acid                                  | 100 <sup>a</sup> , ≥95.0 <sup>b</sup>                      | X        | X        | X     | X        |       | X        |          |          |
| DL-Aspartic Acid                             | -                                                          |          |          |       | X        |       | X        |          |          |
| Azelaic Acid                                 | ≥86 <sup>c</sup>                                           |          |          |       |          |       | X        | X        |          |
| Glutaric Acid                                | 87.5 <sup>b</sup> , 88.9 <sup>e</sup>                      |          |          | X     | X        | X     |          |          |          |
| Maleic Acid                                  | 87.5 <sup>b</sup> , 71-86 <sup>d</sup> , 88.9 <sup>e</sup> | X        |          | X     | X        | X     |          |          |          |
| Malonic Acid                                 | <i>h</i> <sup>f</sup> , 71.9 <sup>e</sup>                  | X        | X        |       |          | X     |          |          | X        |
| Phthalic Acid                                | <i>h</i> <sup>g</sup>                                      |          |          |       |          |       | X        | X        |          |
| Succinic Acid                                | 91.0 <sup>b</sup> , 97.6 <sup>e</sup> , 99.1 <sup>h</sup>  |          | X        | X     | X        |       |          |          |          |
| L-Tartaric Acid                              | <i>h</i> <sup>f</sup> , 77.5 <sup>i</sup>                  |          |          |       |          | X     |          |          | X        |
| Number of Components                         |                                                            | 3        | 3        | 4     | 5        | 4     | 4        | 2        | 2        |
| Avg. Solubility<br>(g/100g H <sub>2</sub> O) |                                                            | 72.8     | 48.7     | 37.8  | 56.6     | 105.0 | 0.4      | 0.19     | 138.5    |
| Avg. MW (g/mole)                             |                                                            | 122.1    | 122.8    | 128.1 | 129.1    | 125.6 | 158.4    | 177.2    | 127.1    |
| Mixture %DRH (±2%)                           |                                                            | <i>h</i> | <i>h</i> | 73-79 | <i>h</i> | 76-79 | <i>h</i> | <i>h</i> | <i>h</i> |

<sup>a</sup> Parsons *et al.* (2004) - Optical Microscope/Flow Cell Study at Multiple Temperatures

<sup>b</sup> Brooks *et al.* (2002) - Bulk solution measurements (24°C)

<sup>c</sup> Andrews and Larson (1993) - EDB measurements (20-25°C)

<sup>d</sup> Choi and Chan (2002) - EDB measurements (20-23°C)

<sup>e</sup> Wise *et al.* (2003) - Bulk solution measurements (24.7-24.9°C)

<sup>f</sup> Peng, Chan, and Chan (2001) - Bulk solution measurements (25°C)

<sup>g</sup> Brooks *et al.* (2004) - TDMA measurements (24°C)

<sup>h</sup> Marcolli, Luo, and Peter (2004) - Bulk solution measurements (25°C)

<sup>i</sup> Apelblat *et al.* (1995) - Vapor pressure isoteniscope technique

The Aerosols Inorganic Model (AIM), the Gibbs Free Energy Minimization (GFEMN) model and the UNiversal Functional Activity Coefficient (UNIFAC) thermodynamic models have been applied to experimental data. AIM, as developed by Clegg, Brimblecombe and Wexler (1998), provides thermodynamic models for gas/liquid/solid equilibrium and accounts for the temperature of the system, component ions involved and interactions of the ions over the span of specified relative humidity [57]. Particles which exhibit curvature effects ( $0.1 \mu\text{m}$ ) are not yet included in the model, nor are sulfate ions. However, current work in AIM has been to extend the model to organics. For this study, AIM was compared to malonic acid.

GFEMN is a thermodynamically theoretical model and has been used previously for  $\text{PM}_{2.5}$ , also known as fine particles. GFEMN, as referenced by Khlystov *et al.* (2005), was used as a secondary literature reference for ammonium sulfate [45] to model the equilibrium growth of particles, which occurs when the free energy is minimized. UNIFAC is a semi-empirical model for predicting activity of non-ideal solutions [45]. This model uses the interaction of functional groups of a component, as well as binary interaction coefficients, to determine the activity coefficients of the mixture and the liquid equilibria information. Equations used to derive the UNIFAC model are explained in Appendix A.

Richard Moore (2006) ran equal mass percent solutions for up to 9 organic acid mixtures and used a trend line to quantify his findings. This trend line was applied to the organic mixtures in this study to verify the results. Overall, the fit was consistent with the results, with few exceptions, as described in the following. Published empirical data, as published by Cruz and Pandis (2000) and Cohen *et al.* (1987),

were also used to compare data with that of ammonium sulfate and calcium chloride. Atomic Force Microscopy (AFM) images were compiled from a thesis published by Juan Lopez-Ruiz (2009) and can be found in Appendix C.

### 4.3.1 Sodium Chloride

To ensure the HTDMA system was functioning properly, several inorganic salts that have been previously well-characterized were analyzed and their hygroscopic properties were compared to that of literature. The first of these salts was sodium chloride.

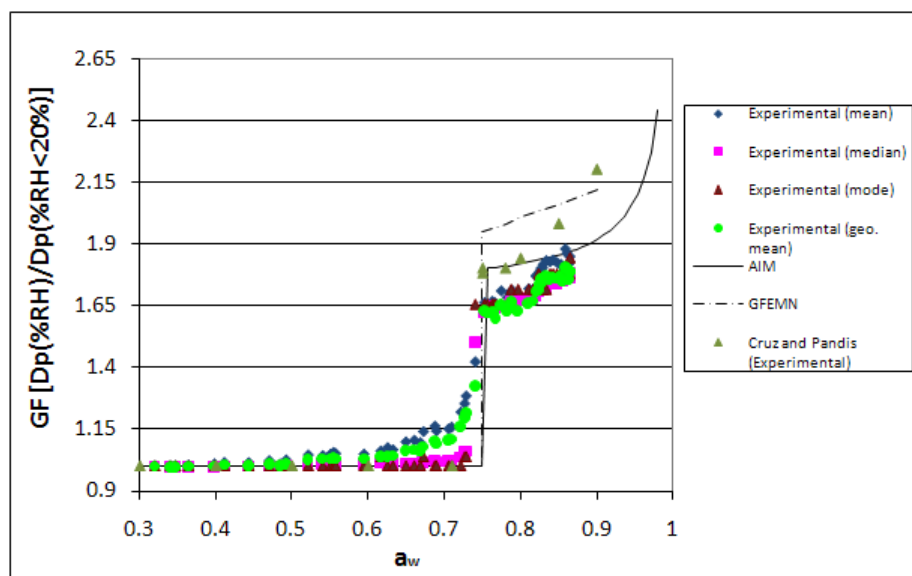


**Figure 4.1:** Hygroscopic growth curves for sodium chloride

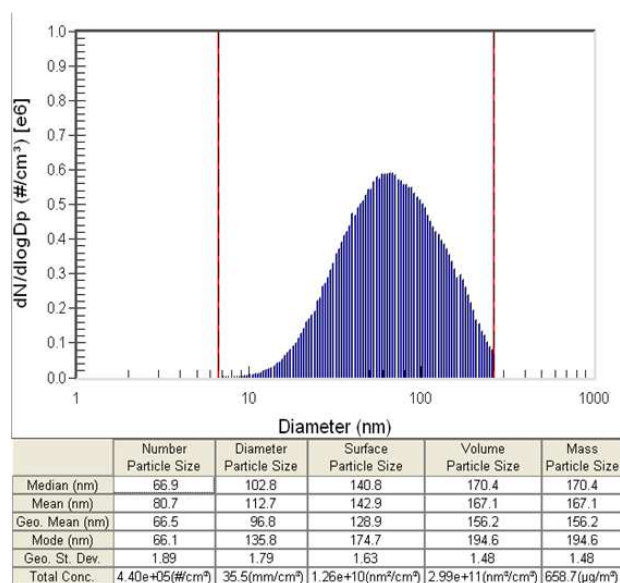


**Figure 4.2:** Full distribution for a 1 g/L sodium chloride solution

As can be seen in Figure 4.2, the full distribution for sodium chloride is a normal distribution. Sodium chloride experienced deliquescence between 73 and 75% RH for the mean, median, mode and geometric mean. The DRH for sodium chloride matched that as reported by Cruz and Pandis (2000) (75%), Aerosols Inorganic Model (AIM)(75-76%), and Gibbs Free Energy Minimization (GFEMN) model (75%). Although the DRH for previous experiments and this study were consistent, the growth factors at the DRH for this study ( $1.64 \pm 0.02$ ) were below expected. AIM and Cruz and Pandis (2000) predicted growth factors of 1.78 and GFEMN predicted 1.95 at the DRH. To correct this issue, a dynamic shape factor of 1.08 was applied to account for the cubic shape of NaCl particles, as described by Kramer *et al.* Figure 4.3 shows the increase in growth factors after the applied shape factor correction.

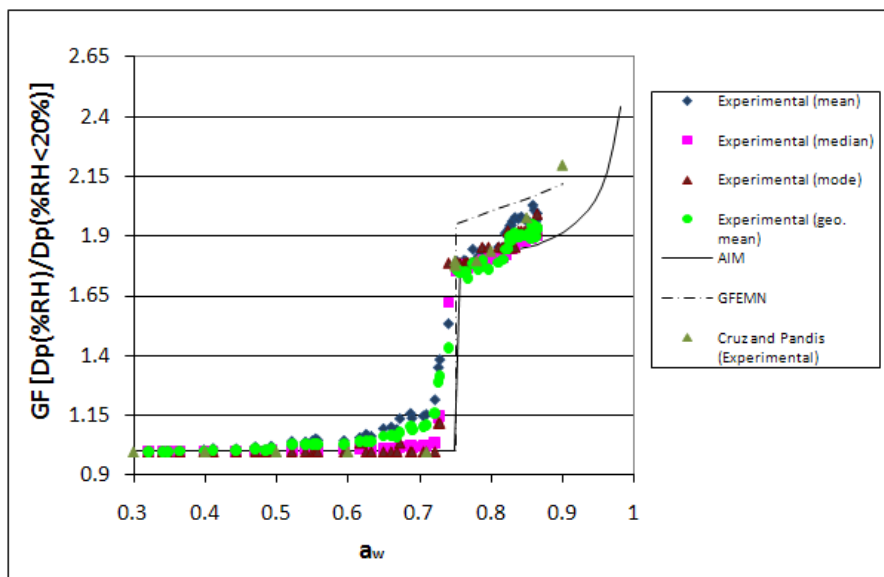


**Figure 4.3:** Growth curves for a 1.08 shape factor applied to sodium chloride

Once the shape factor was applied, the average growth factors at the DRH increased to  $1.81 \pm 0.07$ , which is most consistent with that of AIM. Morphological effects did not appear to affect the size-selection as the distributions in Figure 4.4 were as expected.

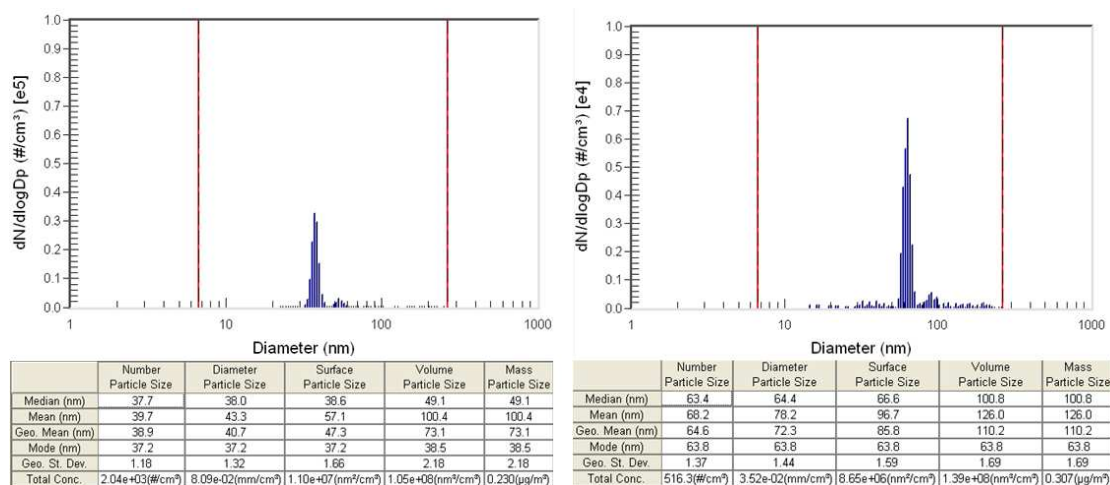


Figure 4.4: Size distributions for sodium chloride at 32% and 82%RH, respectively

### 4.3.2 Calcium Chloride

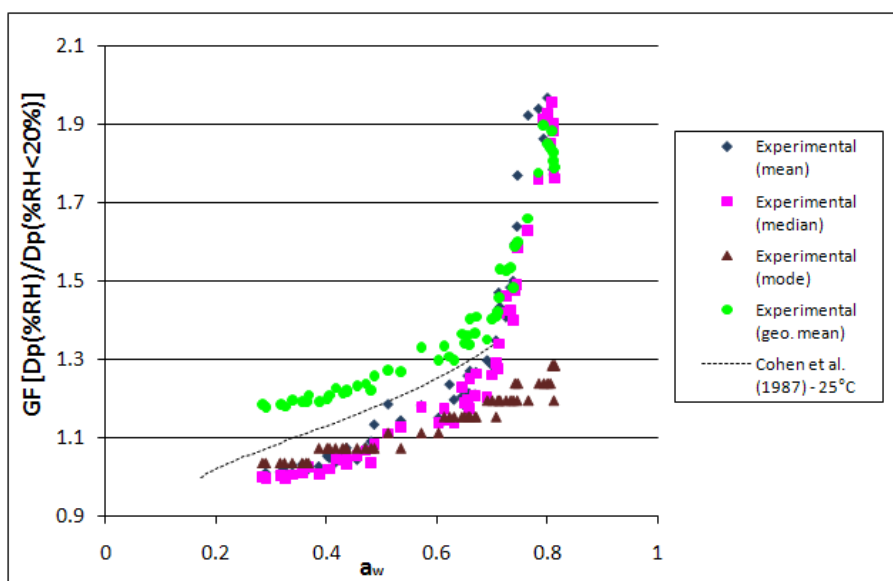
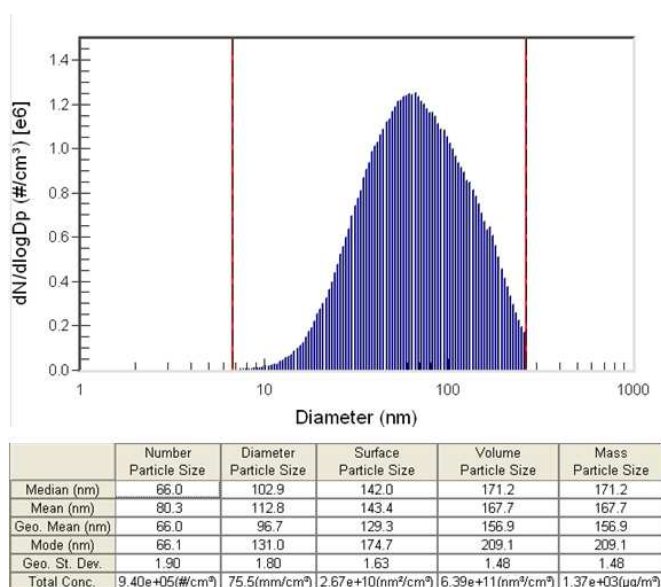


Figure 4.5: Hygroscopic growth curves for calcium chloride



**Figure 4.6:** Full distribution for a 1 g/L calcium chloride solution

As can be seen from the growth curves, calcium chloride grew hygroscopically. The listed literature DRH values for  $\text{CaCl}_2$  at  $25^\circ\text{C}$  are 19-24% and 28.1% RH (Table 3.1). As this experiment was conducted at an initial RH of 24% and did not produce a DRH value, it can either be assumed that the component had a lower DRH value than that of literature or it grew hygroscopically, as water had most likely adsorbed to the particles' surface.

For this study, the average maximum growth factor for the mean, median, and geometric mean was  $1.75 \pm 0.02$ , where as the max growth factor for the mode was 1.29. As can be seen from the distributions, the main peak (mode) of the distribution did experience much growth (41.4 nm to 49.6 nm), but many of the peaks in the larger size region (above the main peak) did increase in concentration with increasing

relative humidity. This shows that growth did occur for those particles.

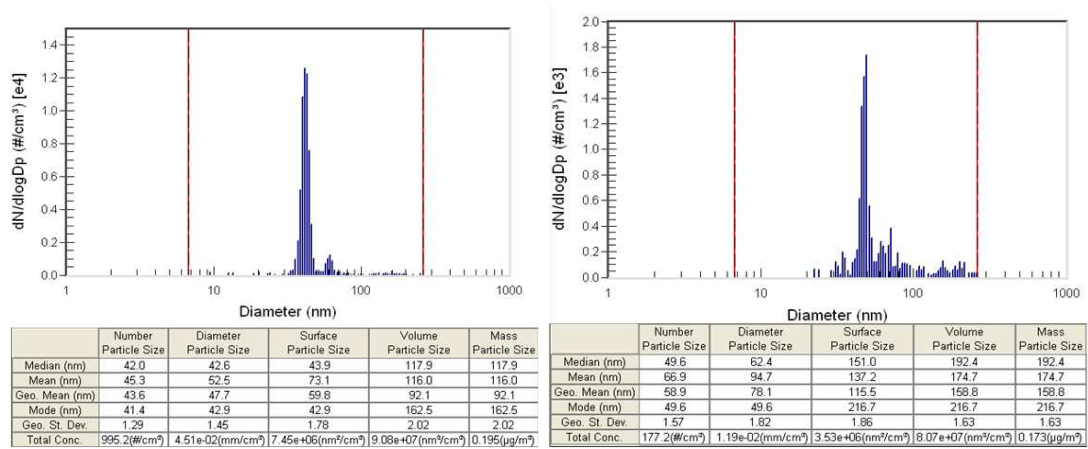


Figure 4.7: Size distributions for calcium chloride at 20% and 72% RH, respectively

### 4.3.3 Ammonium Chloride

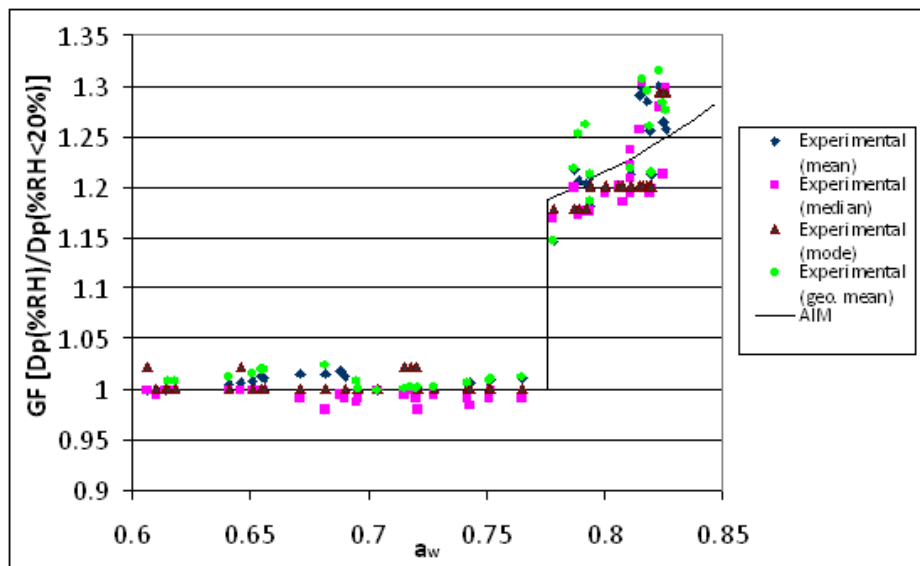
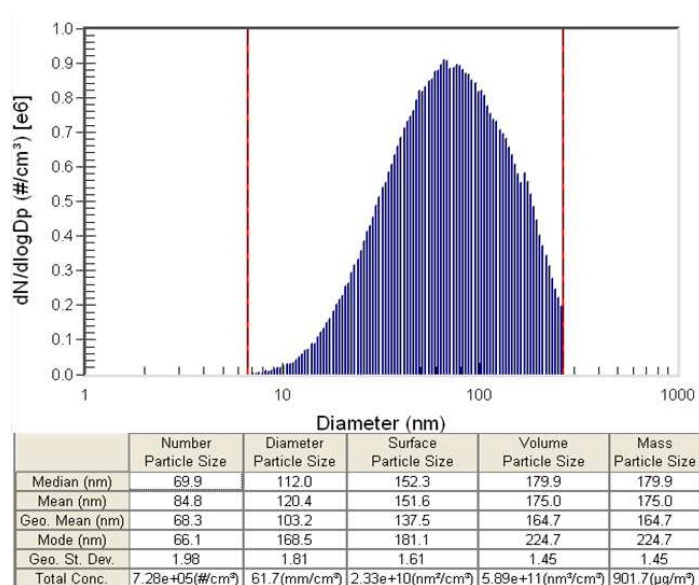


Figure 4.8: Hygroscopic growth curves for ammonium chloride



**Figure 4.9:** Full distribution for a 1 g/L ammonium chloride solution

The DRH for this study was 78%, which matched exactly with AIM and reported literature values by Winston and Bates (1960) at 25°C. The GFs for this study were also well-fitted to AIM. As can be seen from the distributions, ammonium chloride exhibited normal distributions and produced distributions during size-selecting that were expected - clean peaks with the observation of a double-charged particle peak.

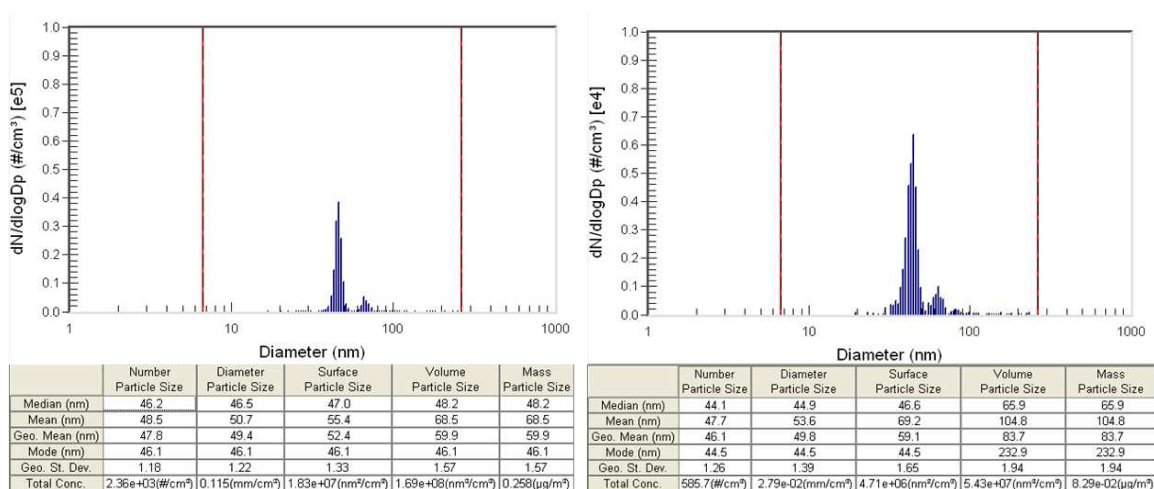


Figure 4.10: Size distributions for ammonium chloride at 12% and 60% RH, respectively

### 4.3.4 Ammonium Sulfate

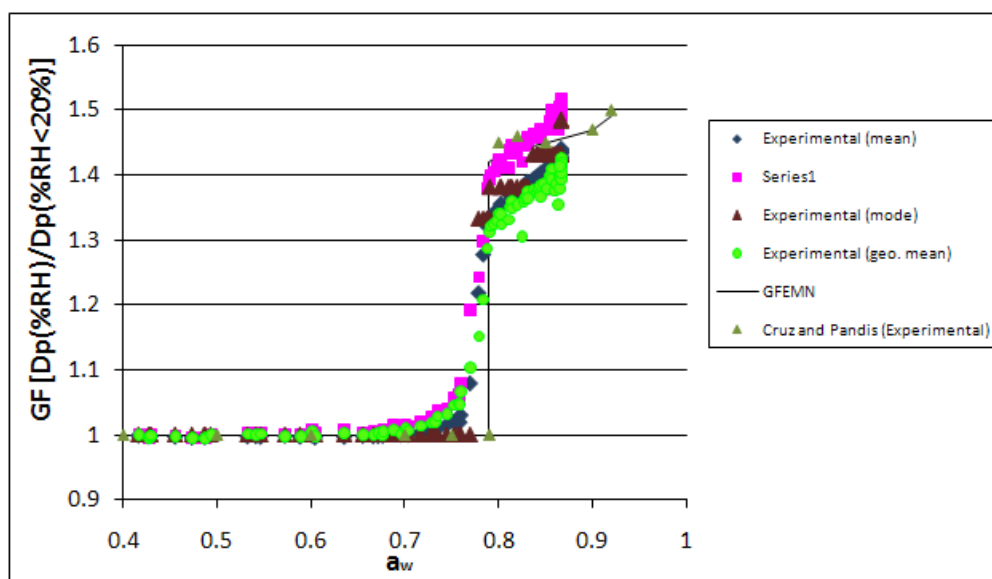
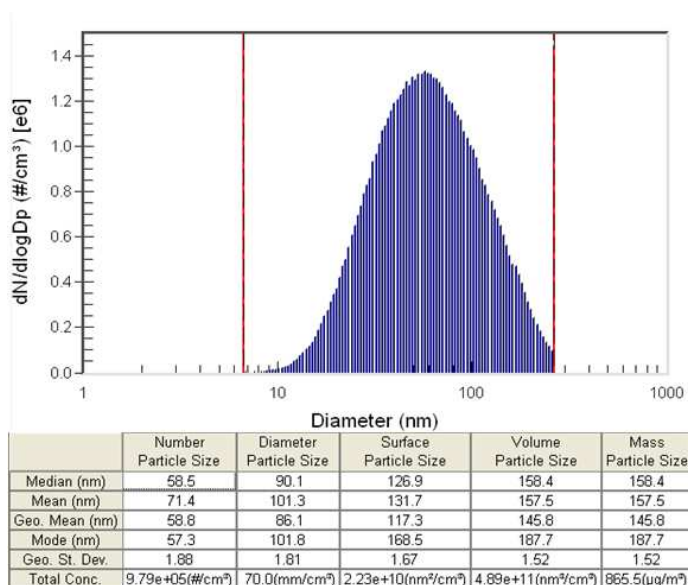


Figure 4.11: Hygroscopic growth curves for ammonium sulfate



**Figure 4.12:** Full distribution for a 1 g/L ammonium sulfate solution

The average GF for the mean, median, mode, and geometric mean at the DRH (75-79%) was  $1.34 \pm 0.03$ . The maximum GF occurred at 87% with an average value of  $1.45 \pm 0.04$ . The DRH values from this study compared best to that reported by Brooks, DeMott and Kreidenweis (2004), who reported DRH values for ammonium sulfate to be  $77 \pm 2\%$  at  $30^\circ\text{C}$ . The DRH values also were consistent with those of the GFEMN model and experimental data supplied by Cruz and Pandis, which were both at 79%. However, the GFs for this study were lower than that of either. At the DRH of 79%, the GFEMN and Cruz and Pandis values were 1.45 and 1.43, respectively. As suggested by Rose *et al.* (2008), a shape factor of 1.02 was applied to ammonium sulfate to produce an average GF at the DRH  $1.38 \pm 0.04$ , which is closer to the theoretical values. This difference in growth can be seen in Figure 4.12. As with most inorganic species, ammonium chloride exhibited normal distributions

and produced distributions during size-selecting that were expected (Figures 4.12 and 4.14).

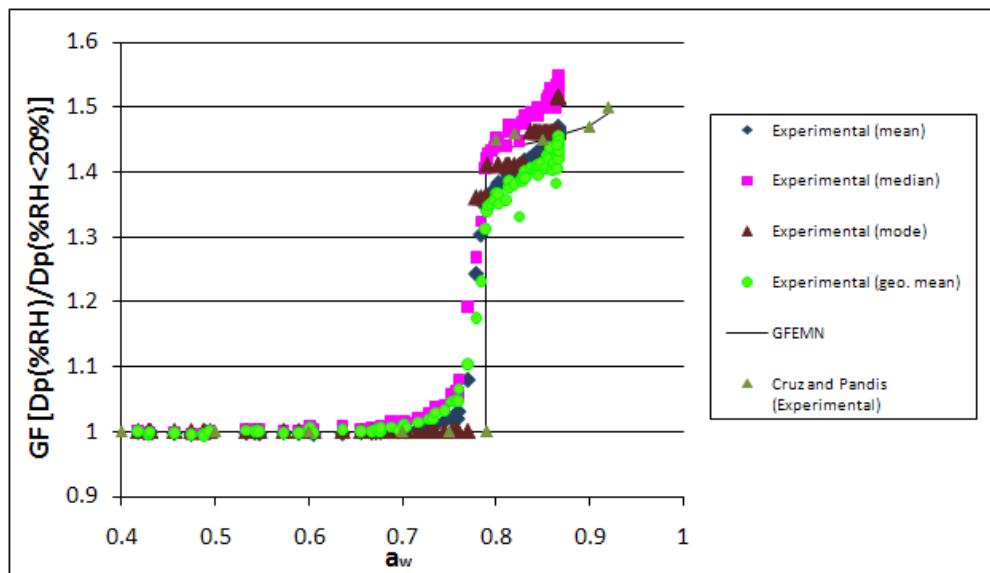


Figure 4.13: Growth curves for a 1.02 shape factor applied to ammonium sulfate

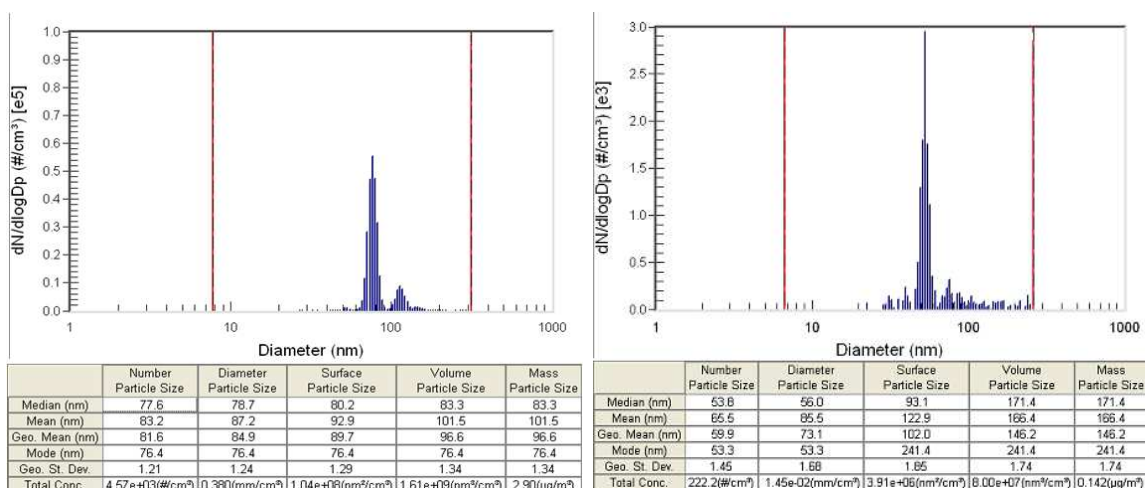


Figure 4.14: Size distributions for ammonium sulfate at 40% and 82% RH, respectively

### 4.3.5 Ammonium Nitrate

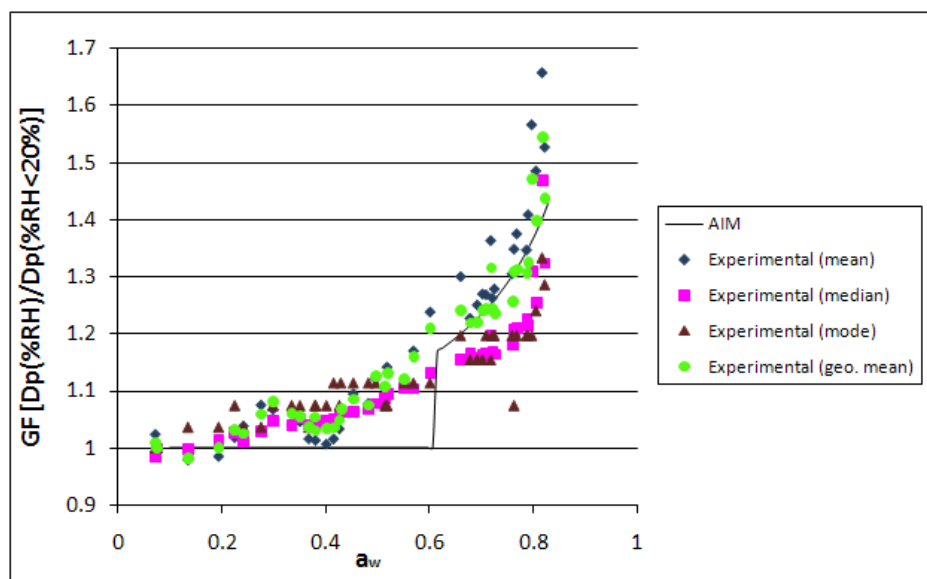


Figure 4.15: Hygroscopic growth curves for ammonium nitrate

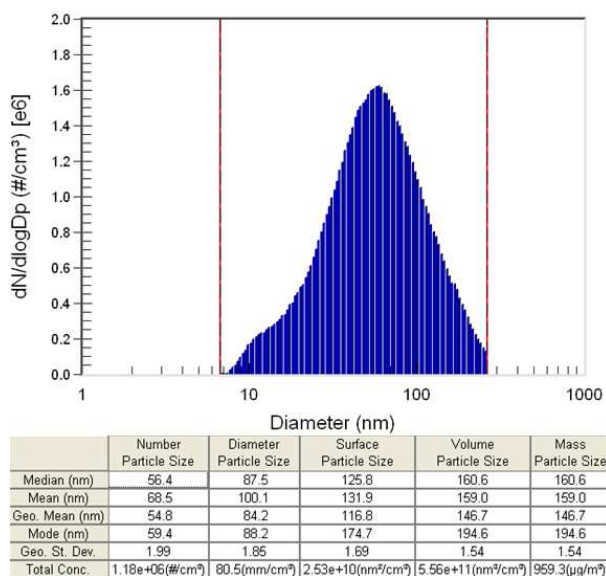
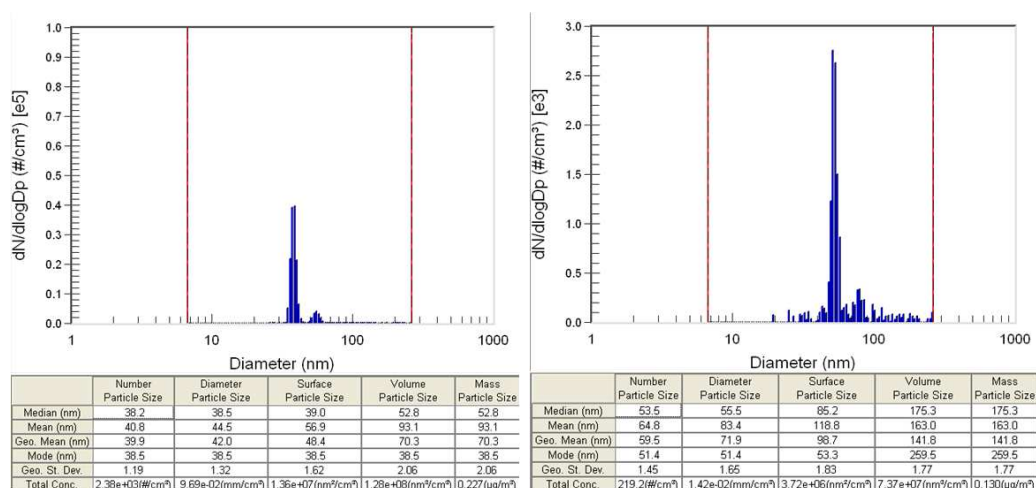


Figure 4.16: Full distribution for a 1 g/L ammonium nitrate solution

In this study, ammonium nitrate grew hygroscopically, even though DRH values have been listed in literature. According to Winston and Bates (1960), the DRH should be  $\sim 63\%$ . The Aerosol Inorganic Model predicted a DRH between 60 and 61%. As shown in Figure 4.16, growth after the supposed DRH match that of AIM. The average maximum GF for the experimental ammonium nitrate for the mean, median, mode and geometric mean was  $1.39 \pm 0.11$ . The GF associated with AIM was 1.40.

The distributions for ammonium nitrate were interesting in that the full distribution experienced nearly bi-modal behavior. Despite this, the size-selected distributions had clean peaks, which suggests no morphological changes occurred between particles.



**Figure 4.17:** Size distributions for ammonium nitrate at 10% and 85% RH, respectively

### 4.3.6 Adipic Acid

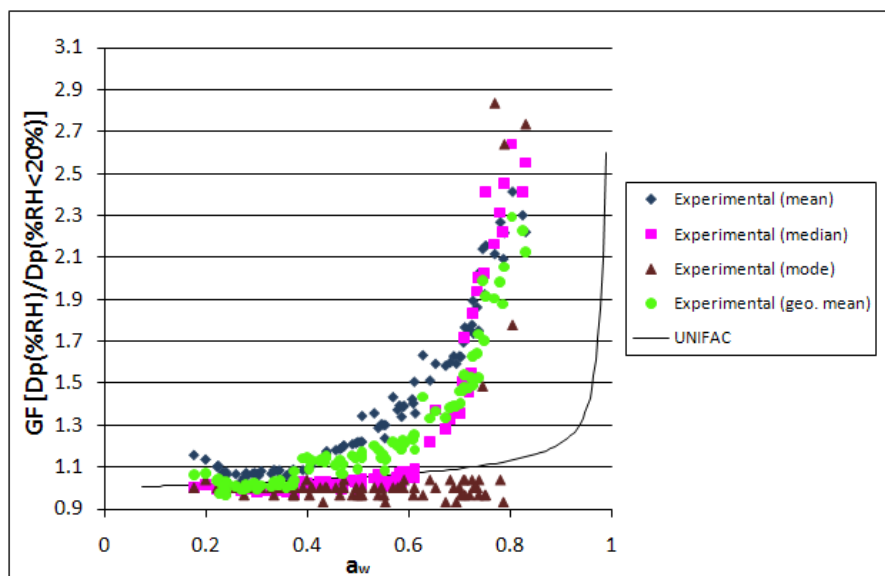


Figure 4.18: Hygroscopic growth curves for adipic acid

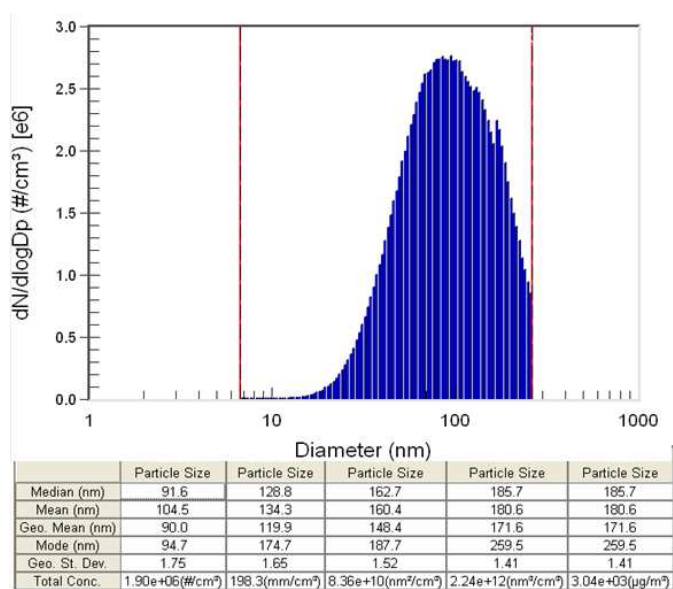
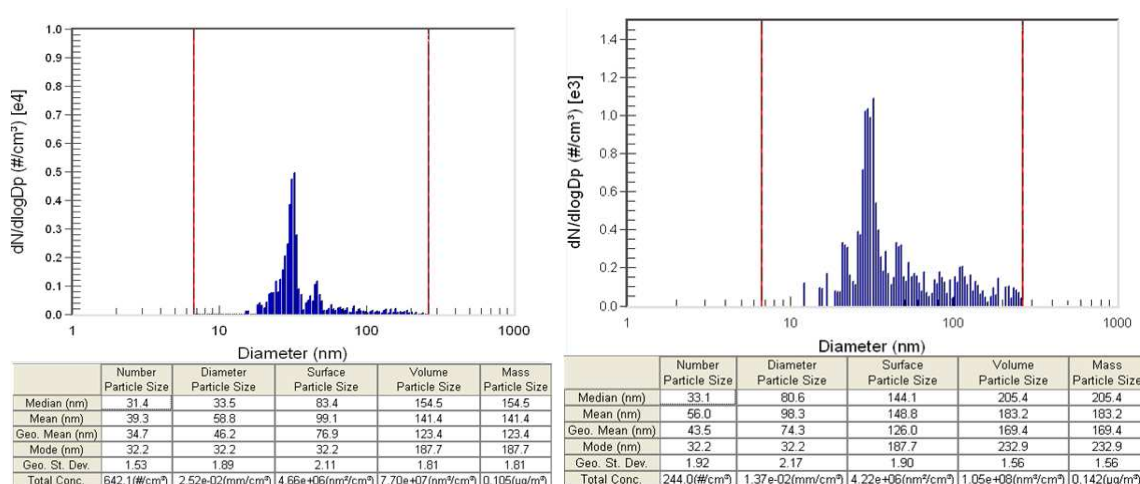


Figure 4.19: Full distribution for a 1 g/L adipic acid solution

As shown in Figure 4.18, the mean, median and geometric mean appear to grow hygroscopically while the mode experiences a sharper increase in growth at 80% RH. The sharp growth increase is consistent with UNIFAC, but occurs at a RH approximately 18% lower. The average maximum GF for the mean, median, mode and geometric mean is  $2.52 \pm 0.20$ . UNIFAC predicted a growth factor of 2.60.

Compared to other organic acids, adipic acid experienced the greatest growth. As can be seen from Figure 4.20, particles in the upper size region increased in concentration at the higher RH. It is interesting to note that adipic acid also experienced a tail in the distribution when size-selection occurred at 30 nm, which suggests differences in morphology between particles.



**Figure 4.20:** Size distributions for adipic acid at 8% and 72% RH, respectively

To confirm adipic acid experienced changes in morphology, images were taken using Atomic Force Microscopy (AFM).

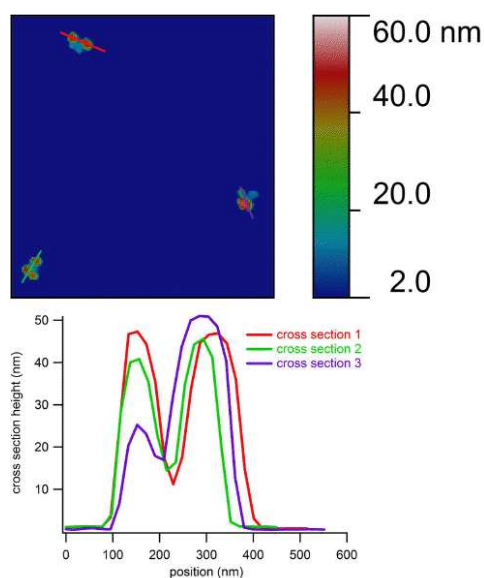


**Figure 4.21:** AFM images for adipic acid  
(Images courtesy of Dr. Dabrina Dutcher (2011))

As can be seen in Figure 4.21, the particles are approximately six times long as they are tall, which accounts for the morphological changes illustrated by the size distributions and explains the slight decrease in GF by the mode. This effect, although similar, is not as drastic as succinic acid.

### 4.3.7 Aspartic Acid

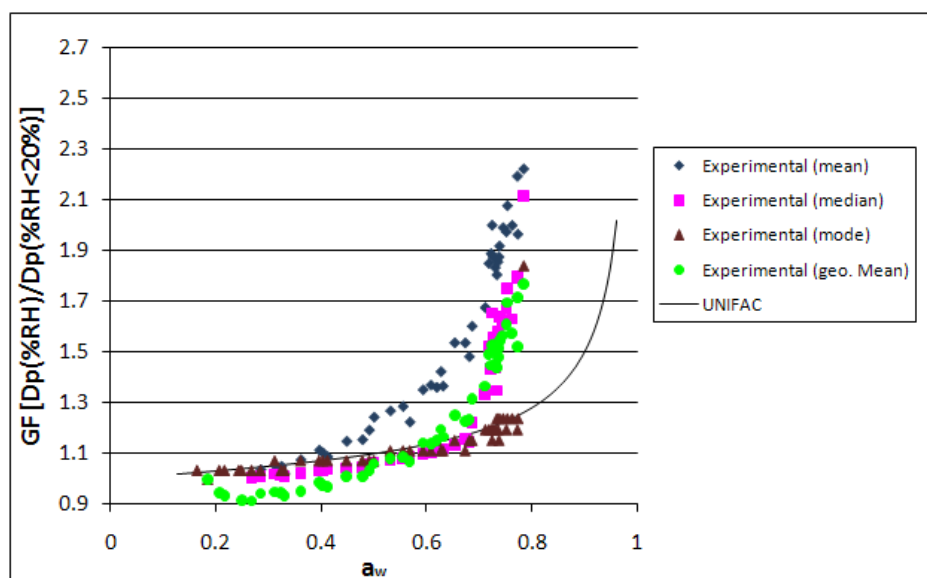


Figure 4.22: Hygroscopic growth curves for aspartic acid

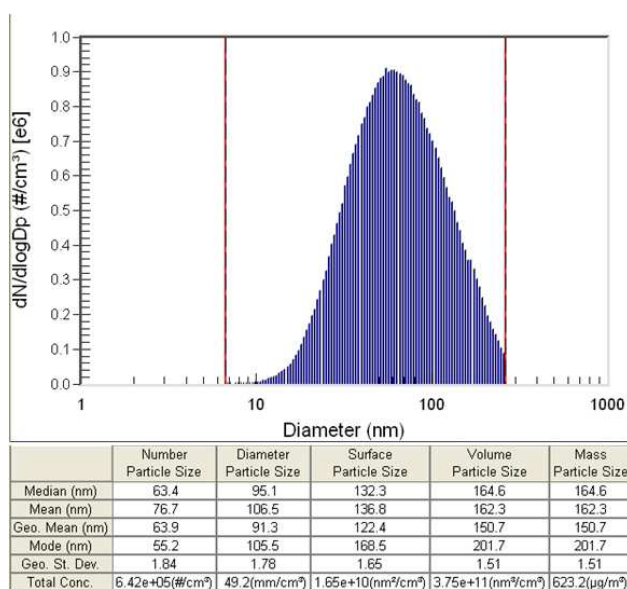
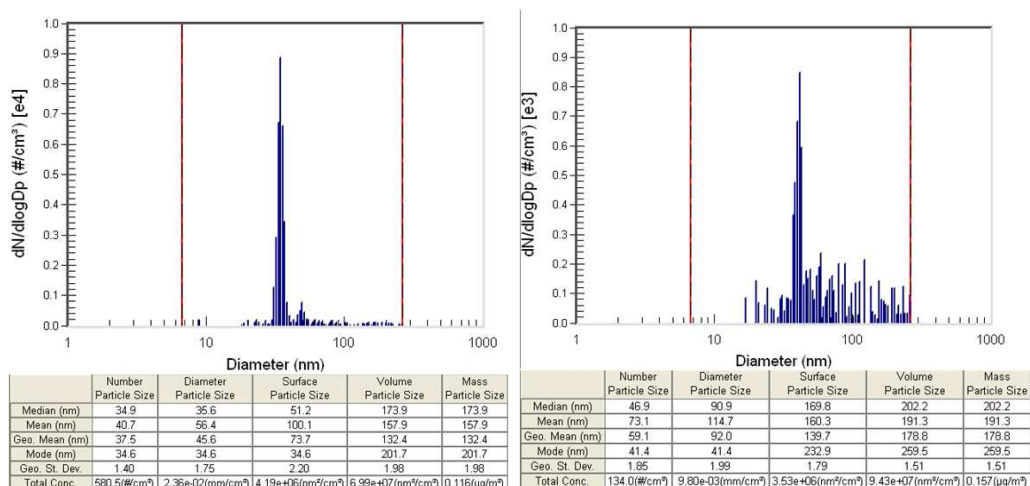


Figure 4.23: Full distribution for a 1 g/L aspartic acid solution

Figure 4.22 shows that the median and geometric mean grow similarly, whereas the mean tends to experience more growth at lower RH and the mode appears to deliquesce at around 79% RH. UNIFAC fits well to the modal distribution up to 79%. As can be seen in Figure 4.24, particles of the upper size region experience the growth while the bulk peak does not. This is also represented in the growth factors graph as the mode does not seem to grow as rapidly as the mean, median or geometric mean until 79%. The maximum average GF for the mean, median, mode and geometric mean is  $1.63 \pm 0.34$ , which reflects the range in growths.



**Figure 4.24:** Size distributions for aspartic acid at 16% and 74% RH, respectively

### 4.3.8 Azelaic Acid

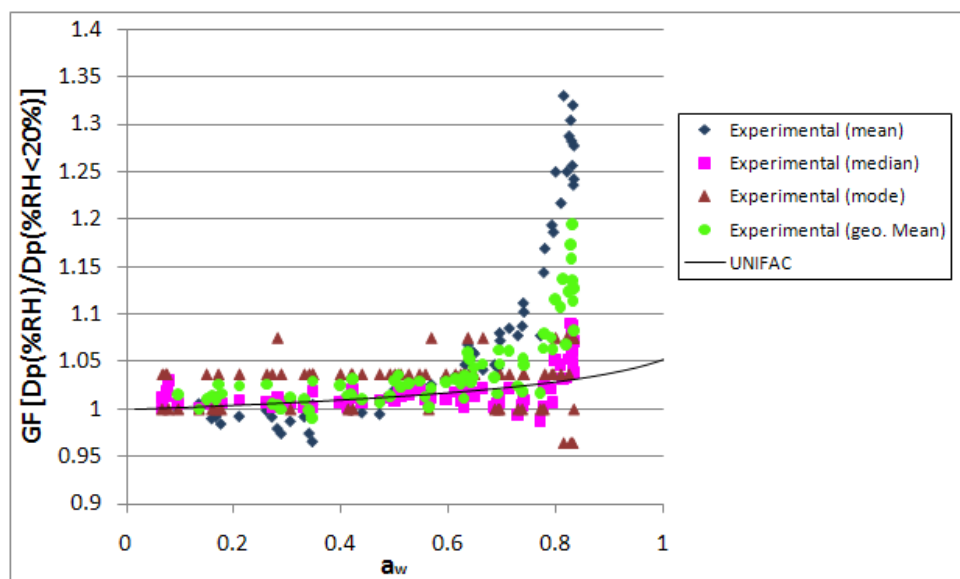


Figure 4.25: Hygroscopic growth curves for azelaic acid

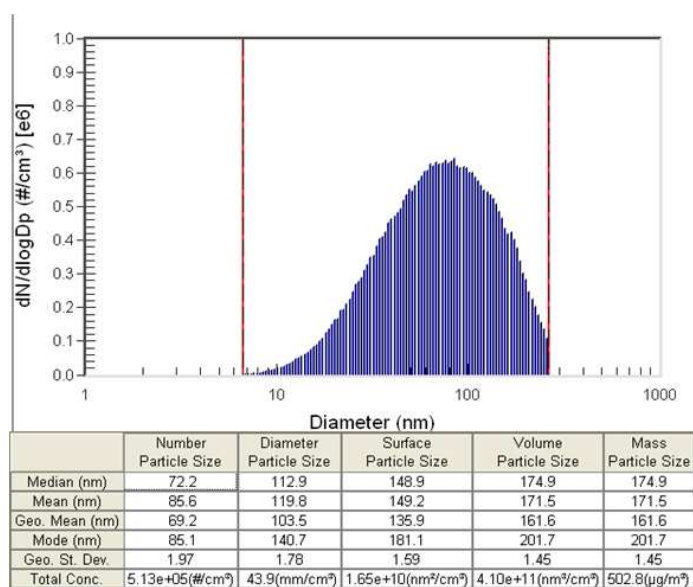
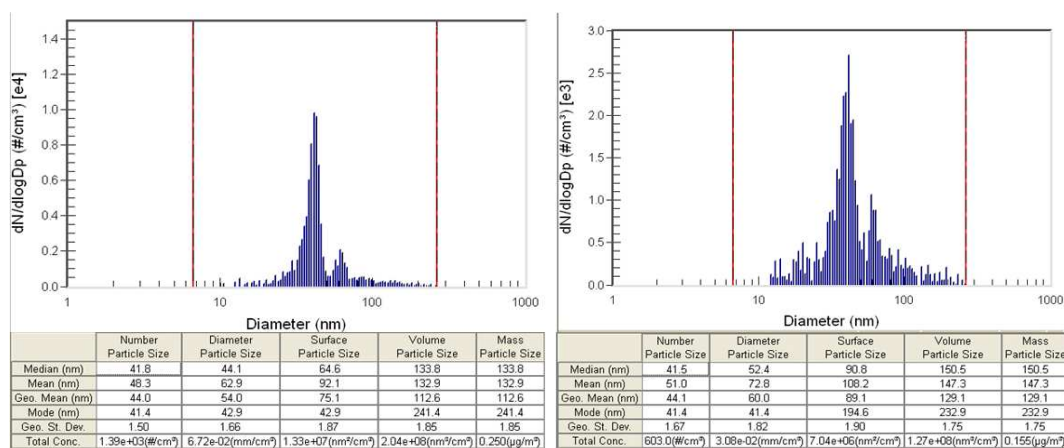


Figure 4.26: Full distribution for a 1 g/L azelaic acid solution

As can be seen from Figure 4.25, the mean and geometric mean experienced the greatest amount of growth, followed by the median, while the mode did not experience much, if any, growth. However, UNIFAC also does not predict much growth and so, it best reflects the results of the mode. Most of the growth that did occur was between 75 and 81% RH. The average maximum growth was  $1.17 \pm 0.11$ . As shown in Figure 4.27, each distribution exhibits a tail, which suggests differences in particle morphology. The larger particles also appear to have experienced much growth, which directly affects the mean and geometric mean, while the bulk of the distribution (mode) remained about the same.



**Figure 4.27:** Size distributions for azelaic acid at 7% and 75% RH, respectively

### 4.3.9 Maleic Acid

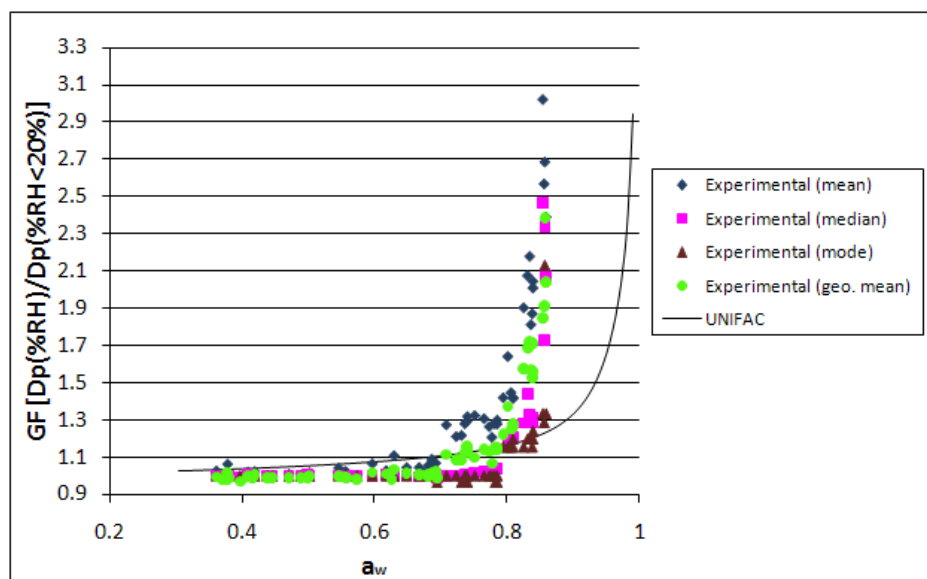


Figure 4.28: Hygroscopic growth curves for maleic acid

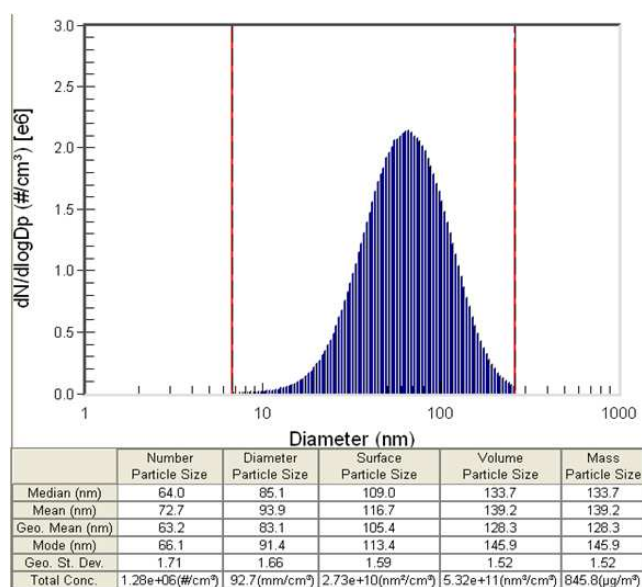
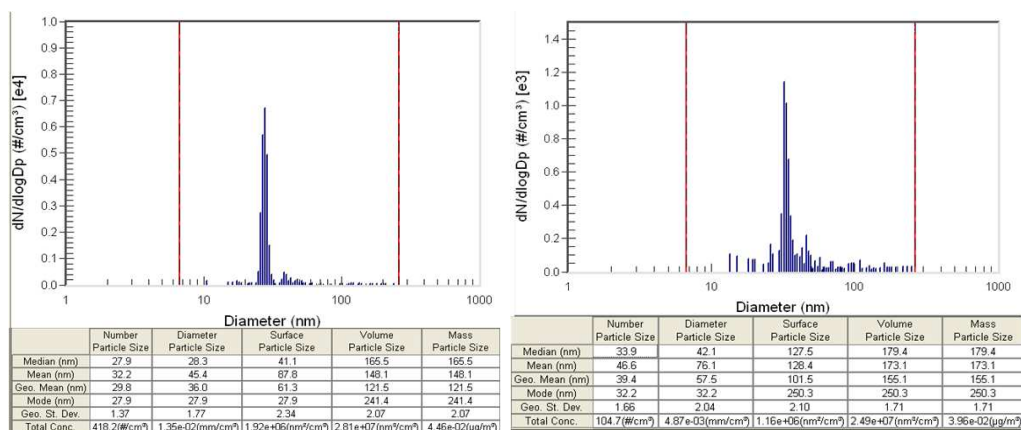


Figure 4.29: Full distribution for a 1 g/L maleic acid solution

The trend of the growth curves for maleic acid were consistent between the mean, median, mode and geometric mean, also verified by the expected distributions for the full and size-selected trials. Each of the growth curves experienced a sharp increase of growth (deliquescence point) around 80% RH. The average maximum growth factor was  $2.50 \pm 0.38$ . The large error resulted because the mode did not show as much growth as the mean, median and geometric mean. The maximum growth factor predicted by UNIFAC was 2.94 and occurred approximately 10% RH higher than the experimental results.



**Figure 4.30:** Size distributions for maleic acid at 8% and 82% RH, respectively

### 4.3.10 Malonic Acid

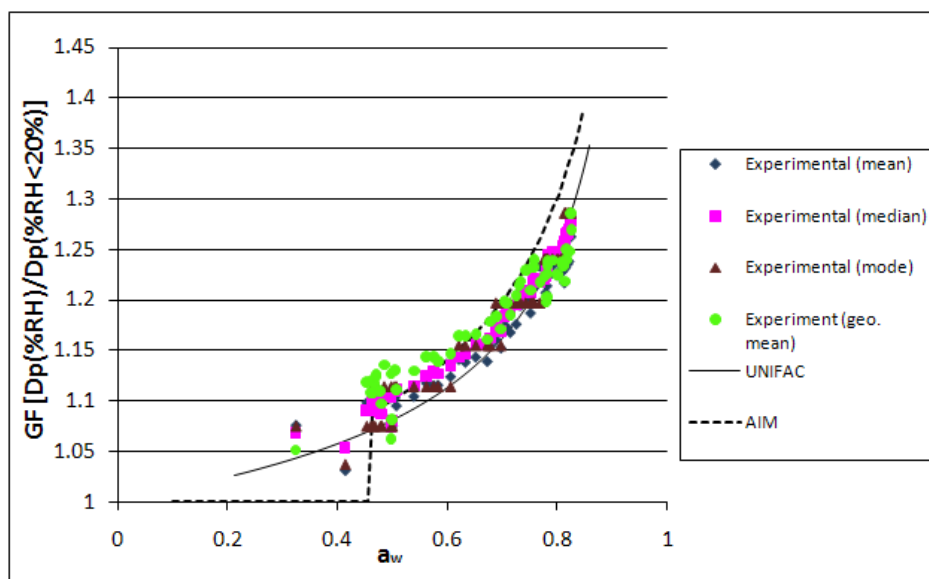


Figure 4.31: Hygroscopic growth curves for malonic acid

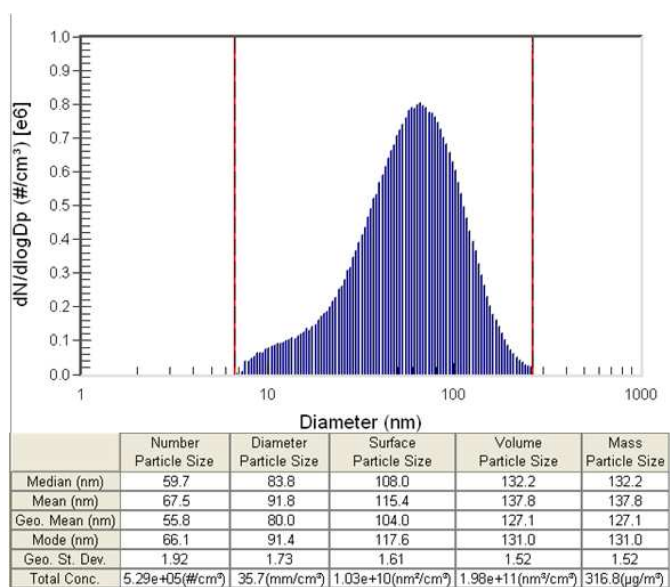
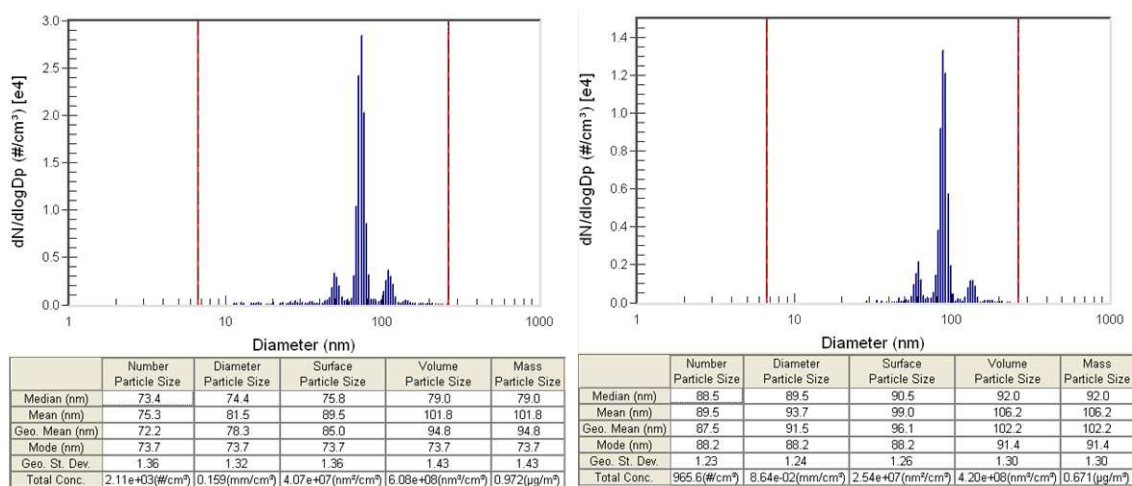


Figure 4.32: Full distribution for a 1 g/L malonic acid solution

Malonic acid experienced hygroscopic growth that was consistent between the averages and with both UNIFAC and AIM (post-deliqescence). The maximum average growth factor was  $1.28 \pm 0.004$ . For a RH of  $\sim 80\%$ , the experimental growth factor ( $1.29 \pm 0.02$ ) also matches that published by Wise *et al.* (2003)(1.32). As can be seen from Figure 4.33, the full distribution naturally has an increased number of smaller particles ( $< 50\text{nm}$ ) than other full organic distributions. It is also interesting to note that the size-selected distributions have three peaks, instead of the expected two. This can be explained by either smaller particles of malonic acid experiencing more growth or that doubly-charged particles are formed and exhibit greater electrical mobility.



**Figure 4.33:** Size distributions for malonic acid at 32% and 72% RH, respectively

### 4.3.11 Phthalic Acid

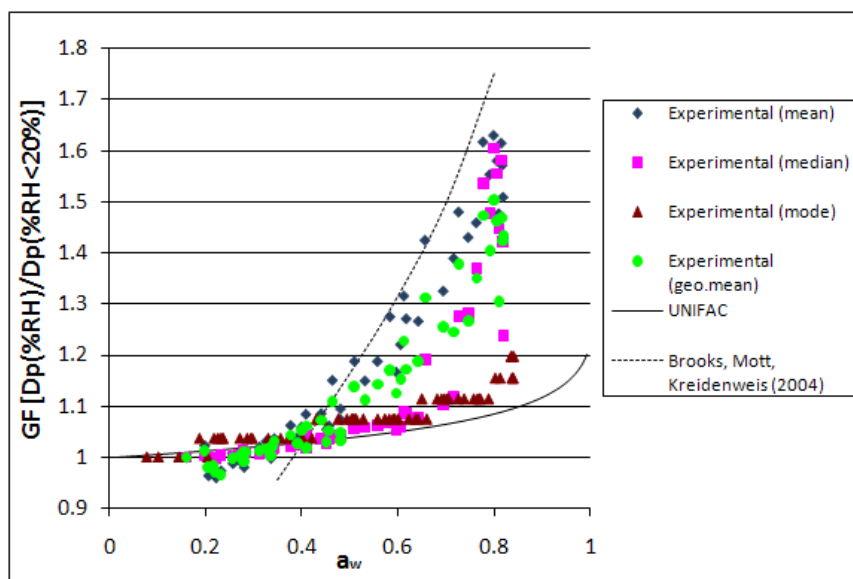


Figure 4.34: Hygroscopic growth curves for phthalic acid

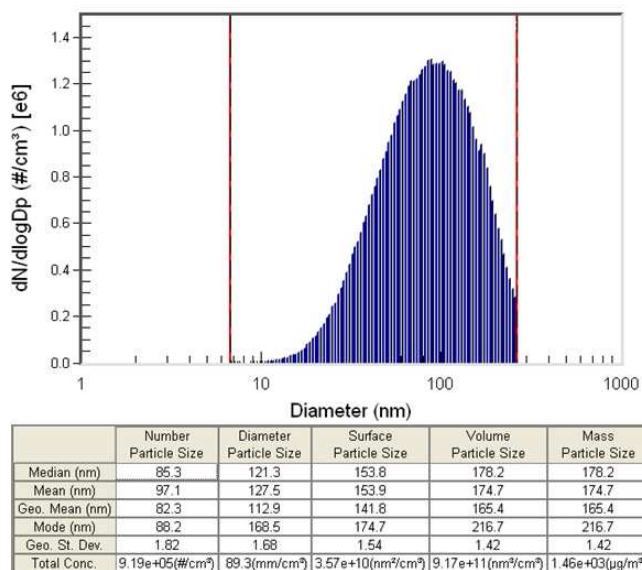
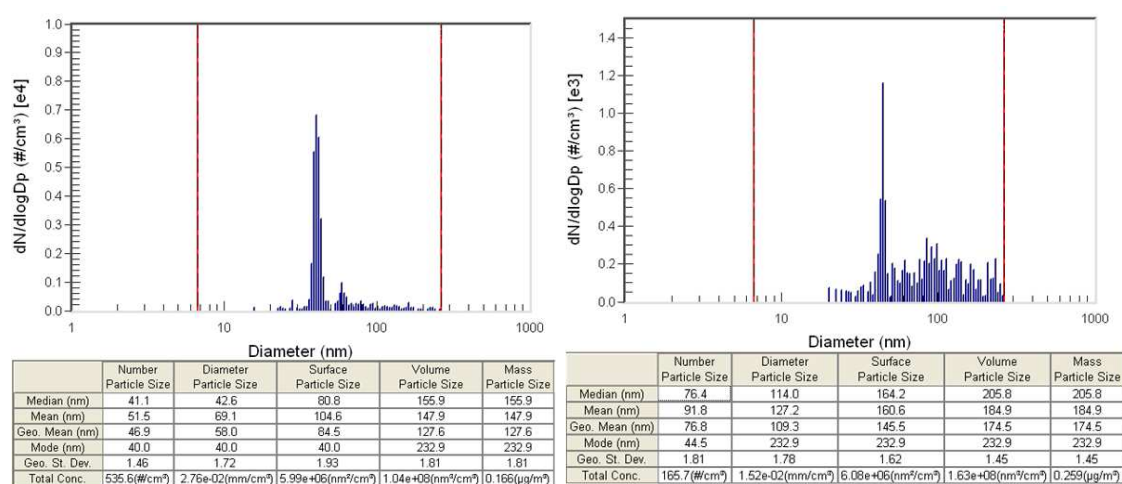


Figure 4.35: Full distribution for a 1 g/L phthalic acid solution

The growth for the experimental mean and geometric mean seem to be consistent with each other, while the mode did not experience much growth and the median was between the two. The experimental mode curve was fairly consistent with UNIFAC, while the mean and geometric mean curves were closer to that published by Dick *et al.* (2000). The maximum average GF for all curves was  $1.44 \pm 0.23$  where the mode only experienced a max GF of 1.14. The size-selected distributions, as shown in Figure 4.36, illustrate the idea of a shift in growth towards the larger particles.



**Figure 4.36:** Size distributions for phthalic acid at 16% and 82% RH, respectively

### 4.3.12 Succinic Acid

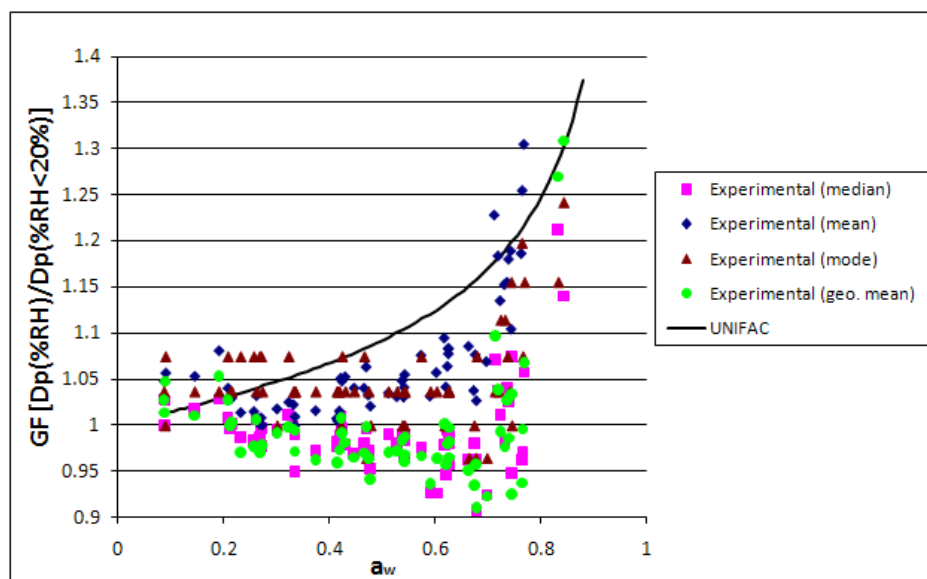


Figure 4.37: Hygroscopic growth curves for succinic acid

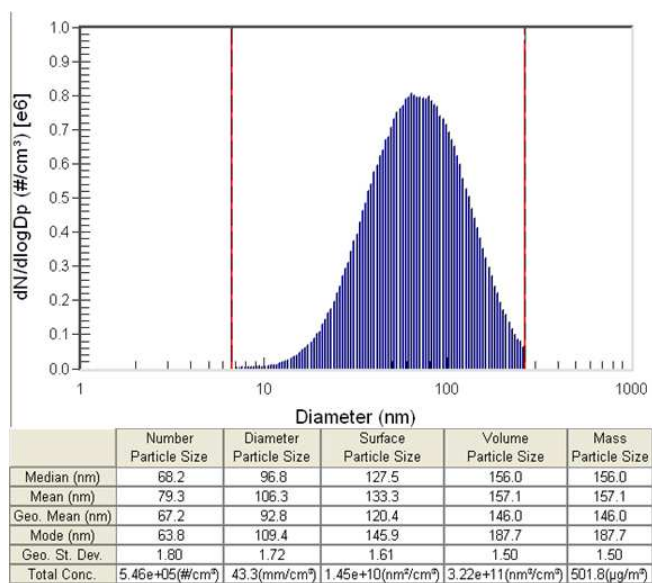
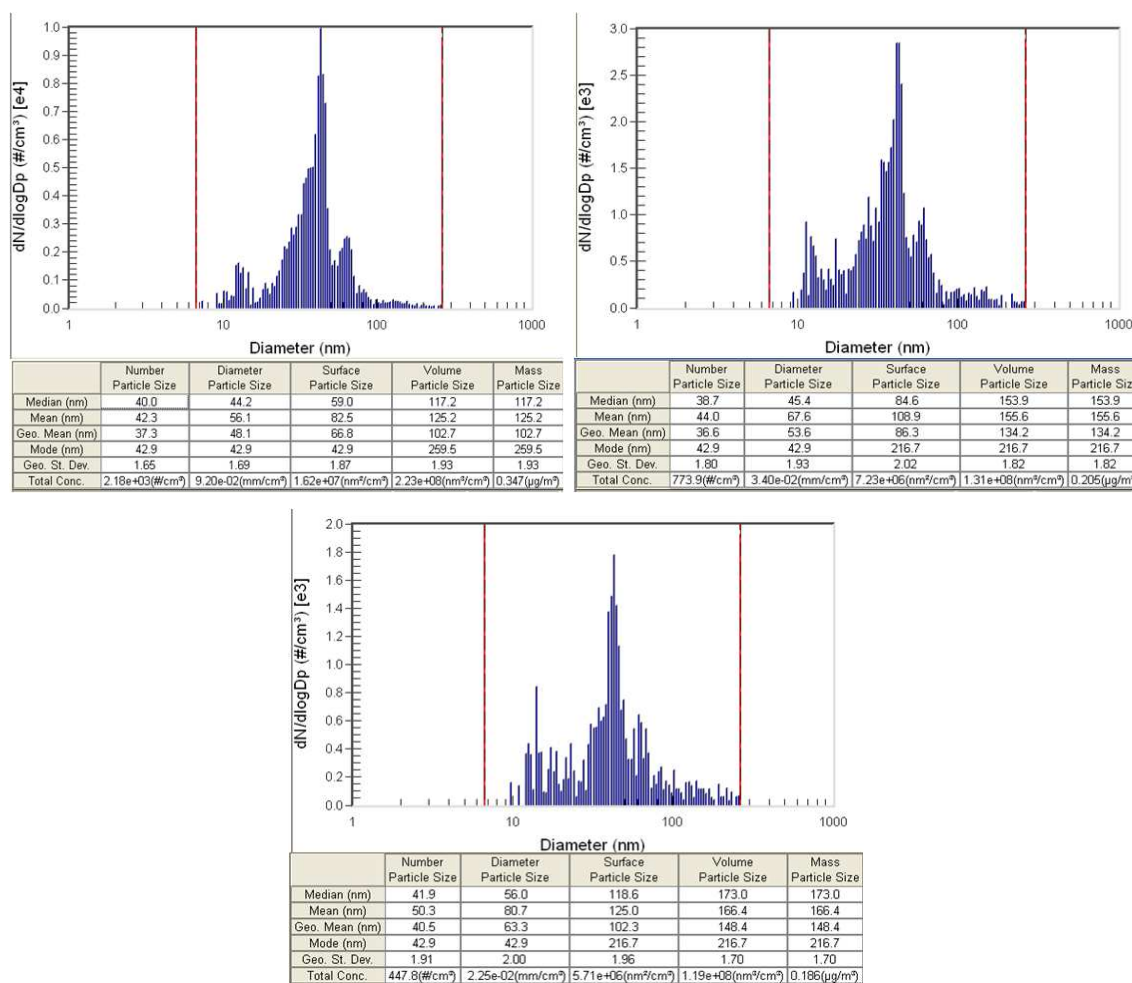


Figure 4.38: Full distribution for a 1 g/L succinic acid solution

The maximum average GF for succinic acid in this study was  $1.18 \pm 0.09$ . Although the maximum GF for succinic acid was consistent with UNIFAC (1.25), the growth curves were generally below the UNIFAC trend line for relative humidities below 79%. In fact, succinic acid experienced the most interesting results out of all the pure organic acids. As can be seen from Figure 4.37, the growth factor trends decrease before experiencing a sharp increase. This decrease can be explained by a change in morphology. As succinic has been studied as a plate-like crystal, it is possible that adsorption of water caused the particle morphology to shift to a spherical shape, which causes the DMAs to read a smaller overall diameter. The distributions for succinic acid were also interesting, as each selection had a tail from the main peak, but also had a smaller peak before the bulk diameter. The smaller peak could possibly correspond to the DMA reading the plate-like structure from a different angle, as each angle would influence the diameter of the readings. As depicted in Figure 4.39, the main peak of the 72% distribution is more defined, which can confirm this theory of morphological changes. As the aerosols become more spherical, the size selection becomes more uniform.



**Figure 4.39:** Size distributions for succinic acid at 8%, 62% and 72% RH, respectively

To further corroborate this theory of changing morphology, images were taken using Atomic Force Microscopy (AFM). Dave Marchese (2010) also produced AFM images of succinic acid from a full 1 g/L solution. As can be seen in Figure 4.40, the particles formed agglomerates that were considerably longer than tall, which would account for the unique behavior in the HTDMA system.

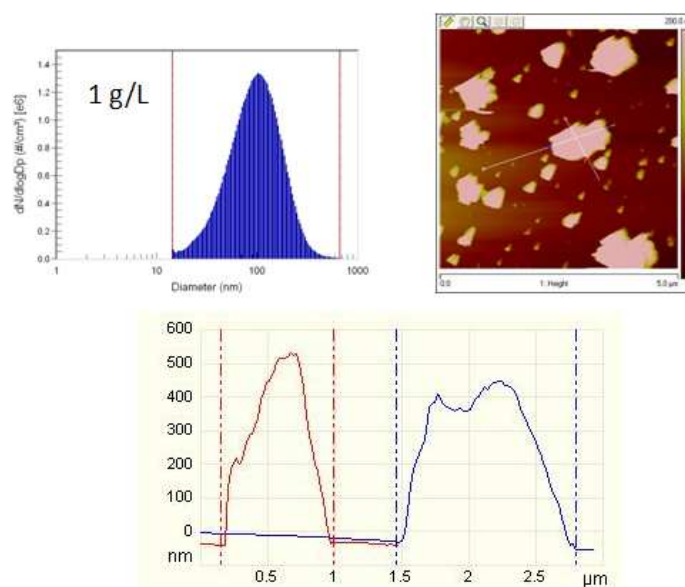


**Figure 4.40:** AFM images of Succinic Acid from 1 g/L solution (Dave Marchese, Bucknell University (2010))

However, Dabrina Dutcher (2011) also viewed succinic acid under the AFM and found different results.

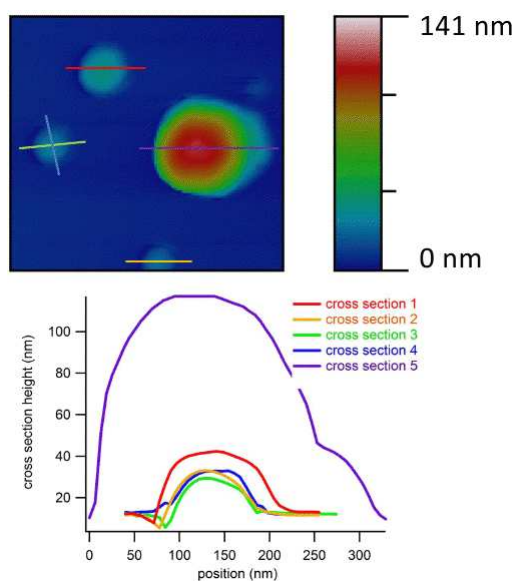


**Figure 4.41:** AFM images of 63 nm Succinic Acid particles  
(Images courtesy of Dr. Dabrina Dutcher (2011))

While the particles are still elongated, they exhibit a more spherical shape. This phenomenon is described in Figure 4.41 and could be the result of transporting the samples through a humid environment prior to imaging.

### 4.3.13 Tartaric Acid

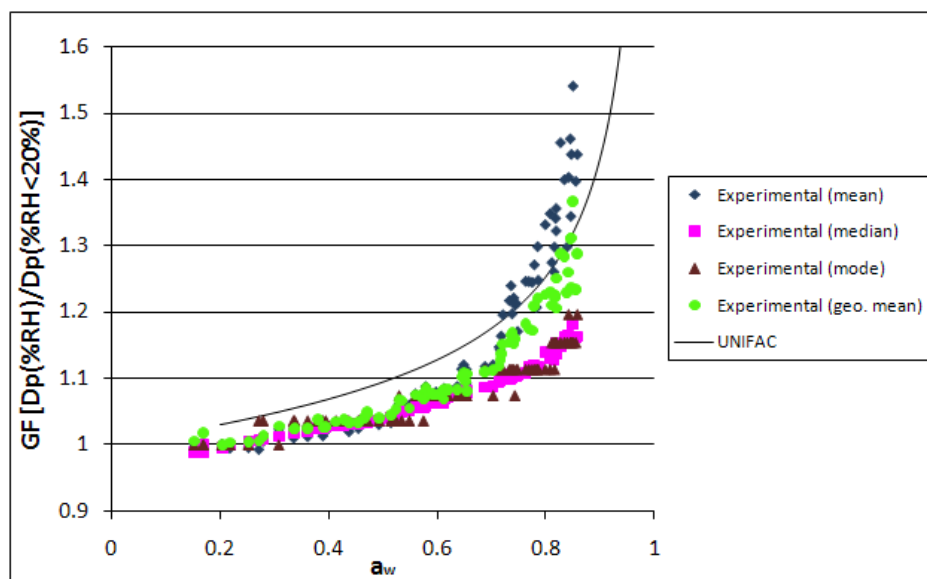


Figure 4.42: Hygroscopic growth of tartaric acid

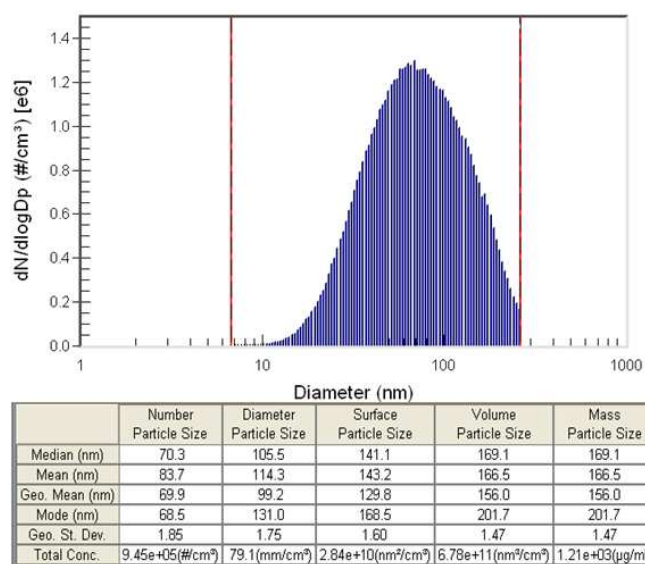


Figure 4.43: Full distribution for a 1 g/L tartaric acid solution

The growth curves for tartaric acid were fairly consistent with each other and with UNIFAC. The curve is slightly below that of UNIFAC until 70% RH, meaning the aerosols are not as active as predicted by theory. Above 70%, the mean and geometric mean increase more than UNIFAC. The maximum average GF was  $1.27 \pm 0.12$ , where the mean and geometric mean experienced the most growth. All distributions for tartaric acid appear to be what is expected.

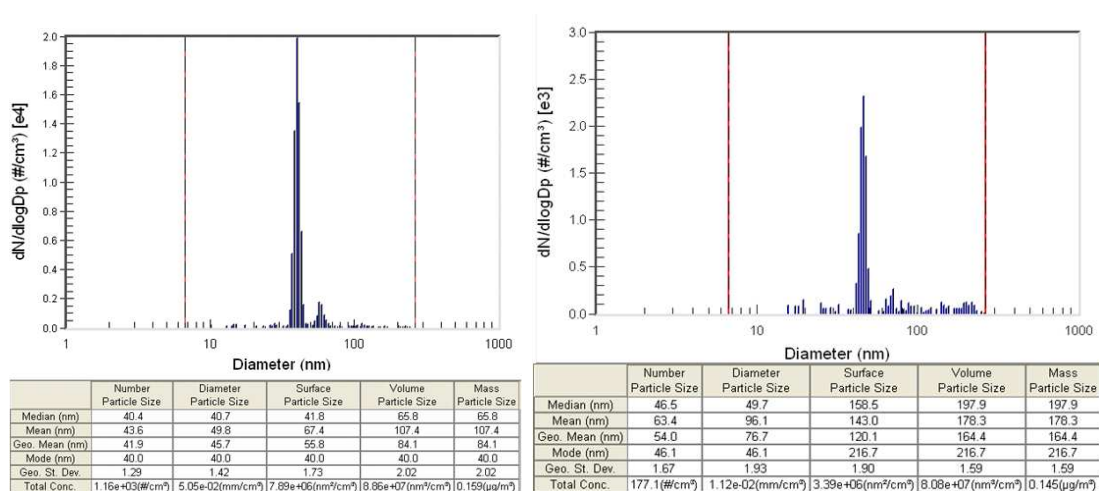


Figure 4.44: Size distributions for tartaric acid at 17% and 83% RH, respectively

### 4.3.14 Mixture A: Adipic, Maleic, and Malonic Acids

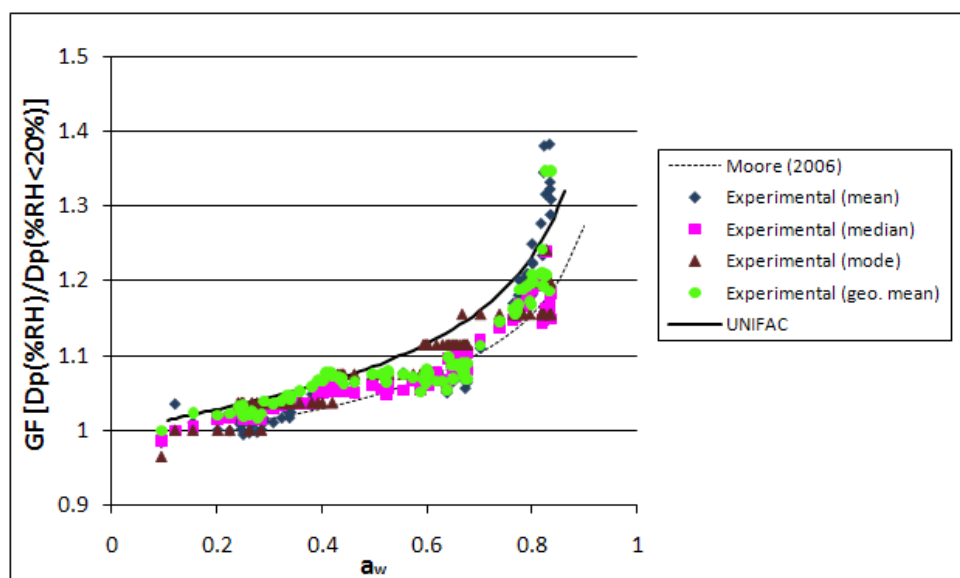


Figure 4.45: Hygroscopic growth curves for mixture A: adipic, maleic, and malonic acids

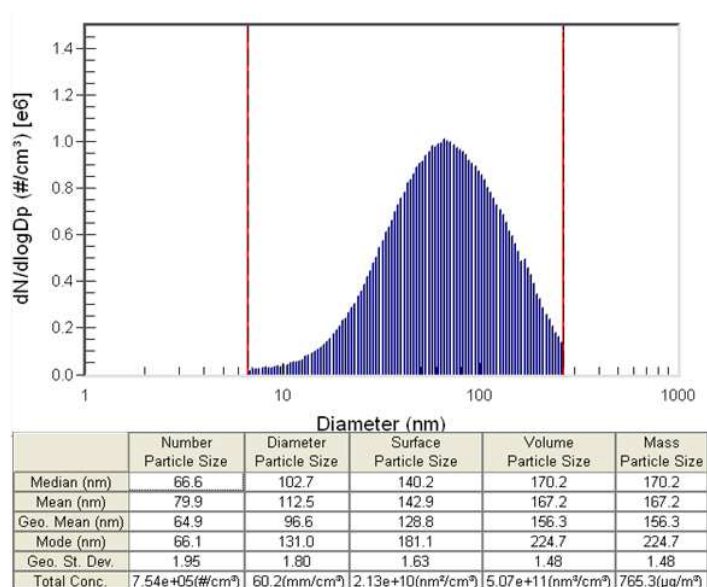
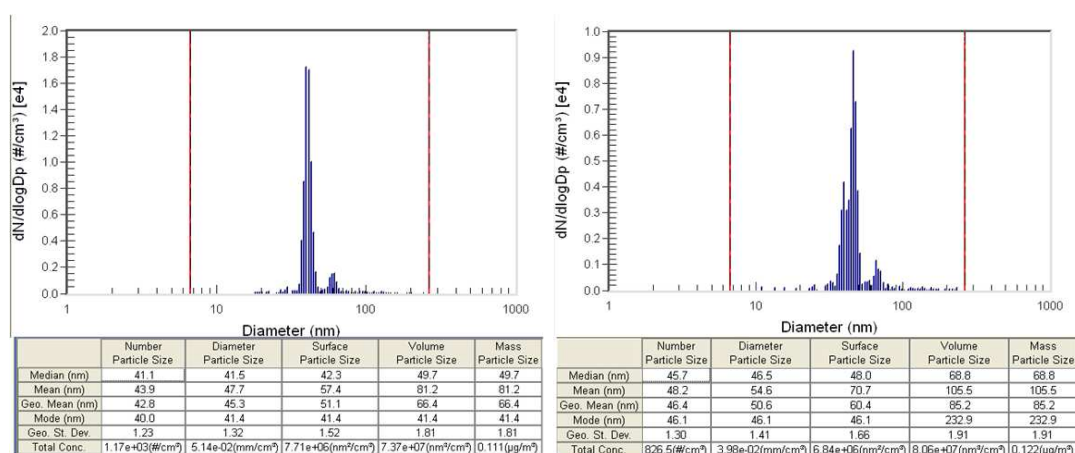


Figure 4.46: Full distribution for a 1 g/L mixture A solution

Mixture A was composed of equal mass amounts of adipic, maleic and malonic acids. As can be seen from Figure 4.45, the mixture grew hygroscopically and this growth was consistent with UNIFAC and data published by Moore (2006). The averages were also very consistent with each other; the maximum average growth factor for all averages was  $1.29 \pm 0.09$ . The full and size-selected distributions also appeared to be normal (Figure 4.47).



**Figure 4.47:** Size distributions for mixture A at 9% and 77% RH, respectively

### 4.3.15 Mixture B: Adipic, Succinic, and Malonic Acids

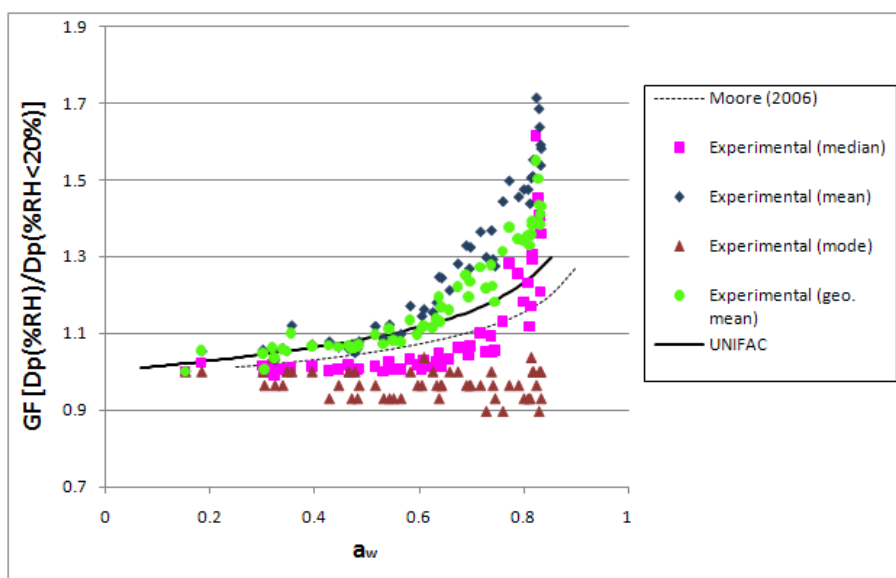


Figure 4.48: Hygroscopic growth curves for mixture B: adipic, succinic, and malonic acids

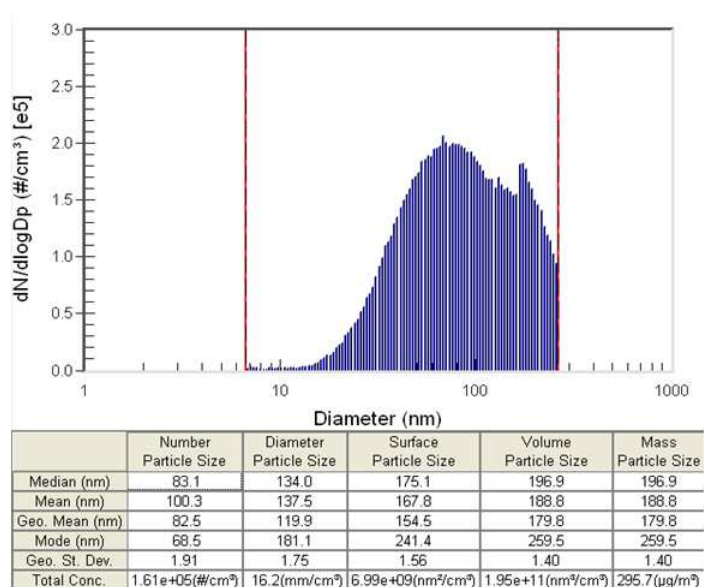
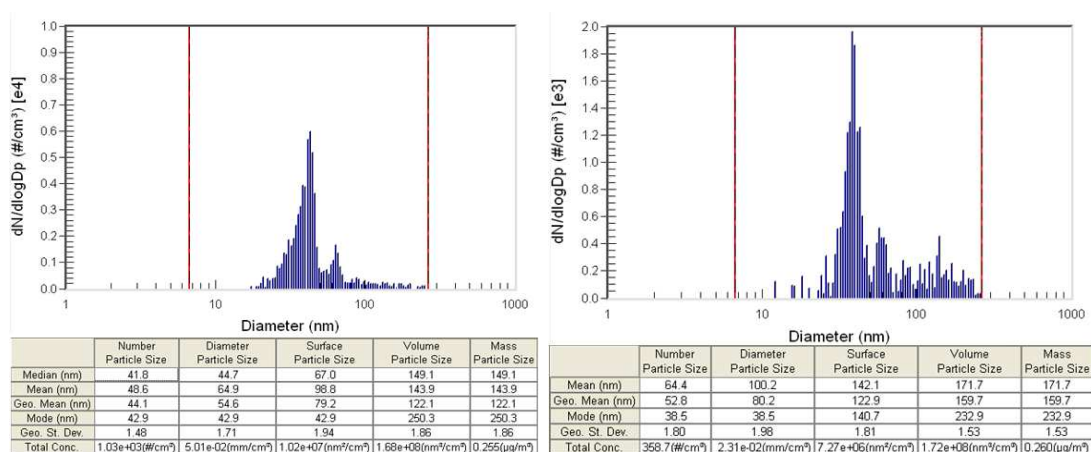


Figure 4.49: Full distribution for a 1 g/L mixture B solution

Mixture B contained equal mass percents of adipic, succinic, and malonic acids. As mixture B contained adipic and succinic acids, it experienced some interesting behavior, much like the pure succinic acid. The modal growth curve seemed to decrease with increasing relative humidity, while the mean, median, and geometric mean growth increased hygroscopically. While the mean and geometric mean were consistent with each other, the median experienced growth between that and the mode. The trend published by Moore (2006) was most consistent with the median, while UNIFAC more closely followed that of the mean and geometric mean. This unusual behavior is enforced by the distributions shown in Figure 4.50, which are very similar to that of pure succinic acid. The dry particle distribution has a tail off the main peak to suggest the particles are of differing morphologies. At higher RH, the larger sized particles increased in concentration as the smaller particles grew, which explains the growth of the mean, median and geometric mean. The bulk peak tends to not shift as much, which explains the minimal growth of the modal curve. The average maximum growth factors for all averages was  $1.44 \pm 0.3$ .



**Figure 4.50:** Size distributions for mixture B at 10% and 71% RH, respectively

### 4.3.16 Mixture C: Adipic, Glutaric, Maleic, and Succinic Acids

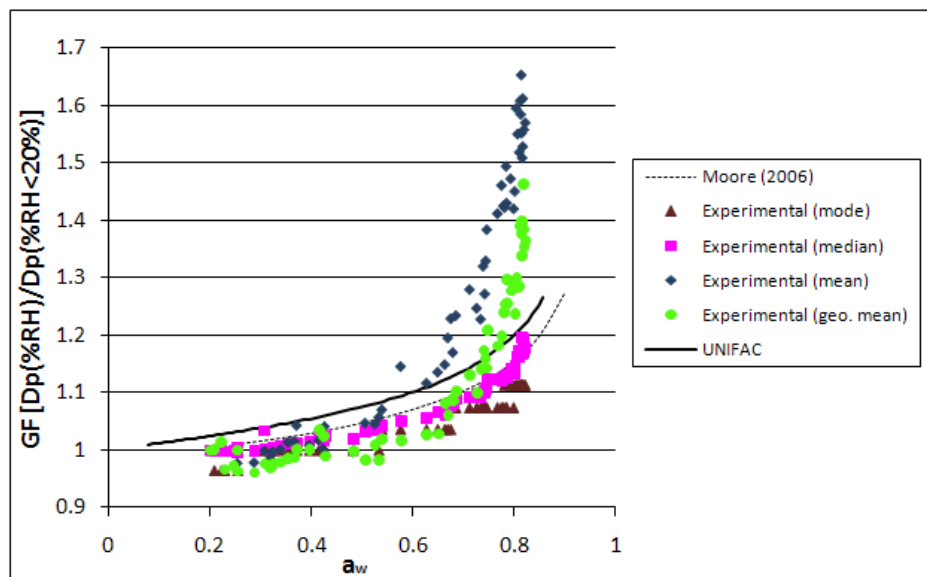


**Figure 4.51:** Hygroscopic growth curves for mixture C: adipic, glutaric, maleic, and succinic acids

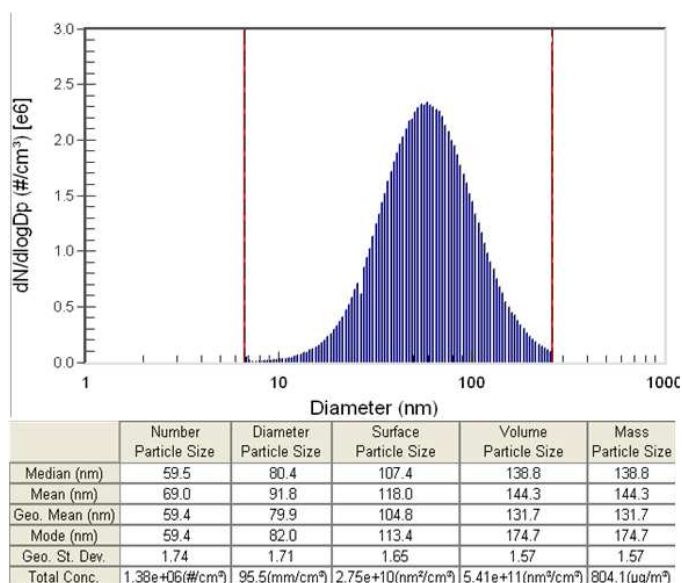


**Figure 4.52:** Full distribution for a 1 g/L mixture C solution

Mixture C contained adipic, glutaric, maleic and succinic acids. Although this mixture contained adipic and succinic acids, their effects were not as well documented due to lower concentrations of adipic and succinic acids present. Although the concentrations were low enough not to drastically affect growth curve behavior, a lack of growth in the mixture curve is indicative of succinic and adipic influences. The dramatic increase in growth by 80% RH is consistent with the behavior of pure maleic acid. The trend line published by Moore (2006) was very consistent with the trends of the median and mode. Again, increased concentrations of larger sized particles contributed to the increase of the mean and geometric mean values (Figure 4.53). The average maximum growth factor for all averages was  $1.34 \pm 0.25$ , where the large error can be attributed to more growth of larger particles.

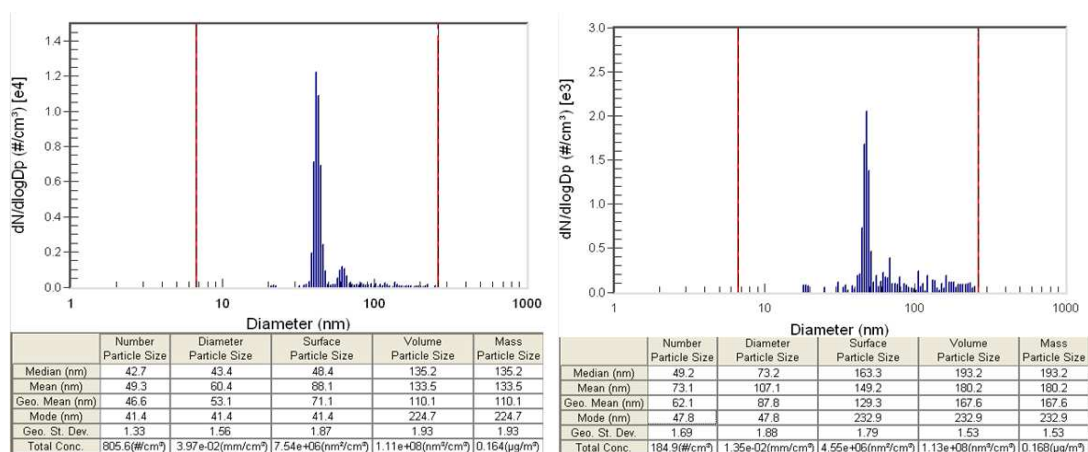
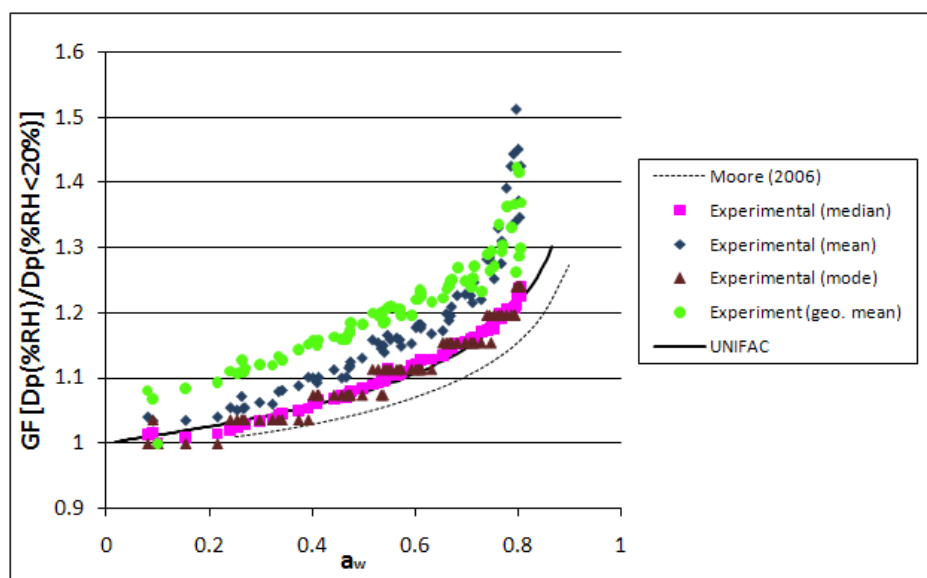
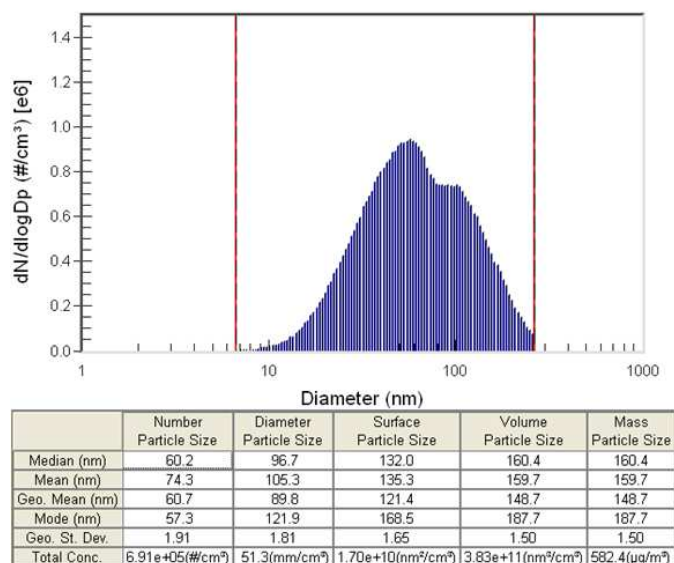


Figure 4.53: Size distributions for mixture C at 20% and 80% RH

### 4.3.17 Mixture D: Adipic, Glutaric, Maleic, Aspartic and Succinic Acids



**Figure 4.54:** Hygroscopic growth curves for mixture D: adipic, glutaric, maleic, aspartic and succinic acids



**Figure 4.55:** Full distribution for a 1 g/L mixture D solution

Mixture D was composed of adipic, glutaric, maleic, aspartic and succinic acids and grew hygroscopically over the tested range of RH. The effects of adipic and succinic acid were negated by the low concentrations of each substance. While the strong growth effect of maleic acid was present by 78% RH, its effects were also inhibited by the lower concentration of maleic acid in the mixture, as pure maleic acid reached a GF over 3.0 and this mixture exhibited a max GF of 1.57 (mean). The mode and median curves were accurately modeled by UNIFAC and were more active than that published by Moore. The full distribution (Figure 4.55) exhibited unique behavior of a nearly bi-modal distribution. That said, the distributions of the size-selected particles were as expected. The average maximum growth factor was  $1.35 \pm 0.14$ .

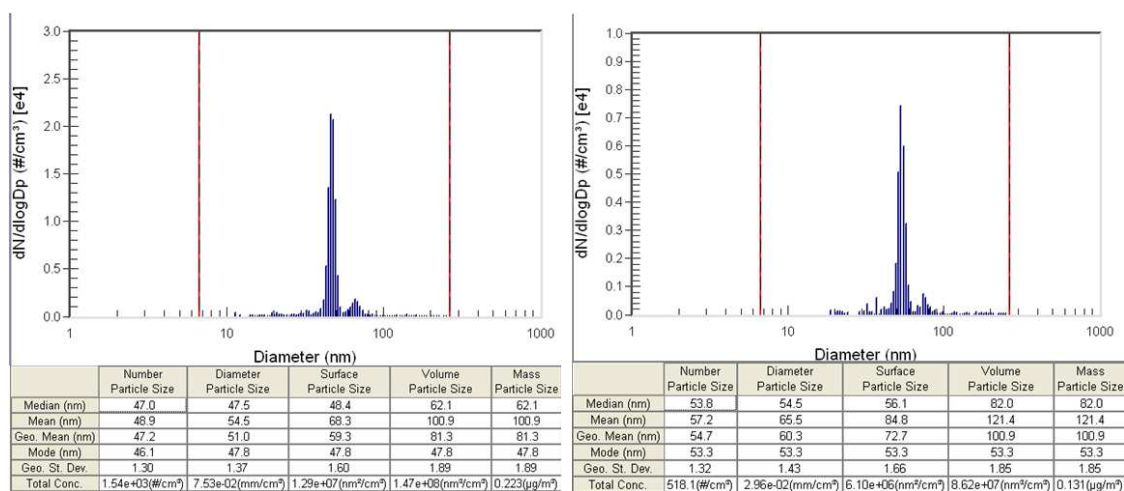
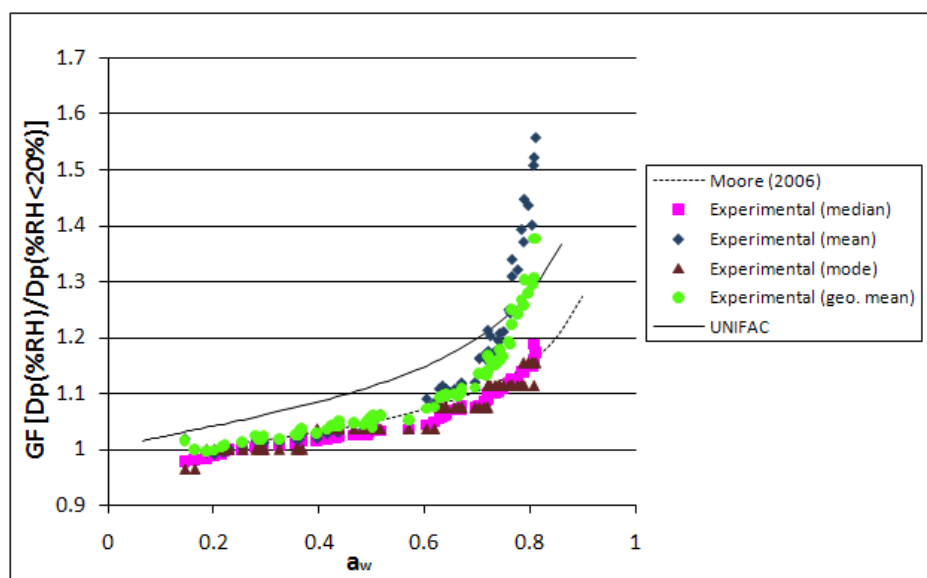
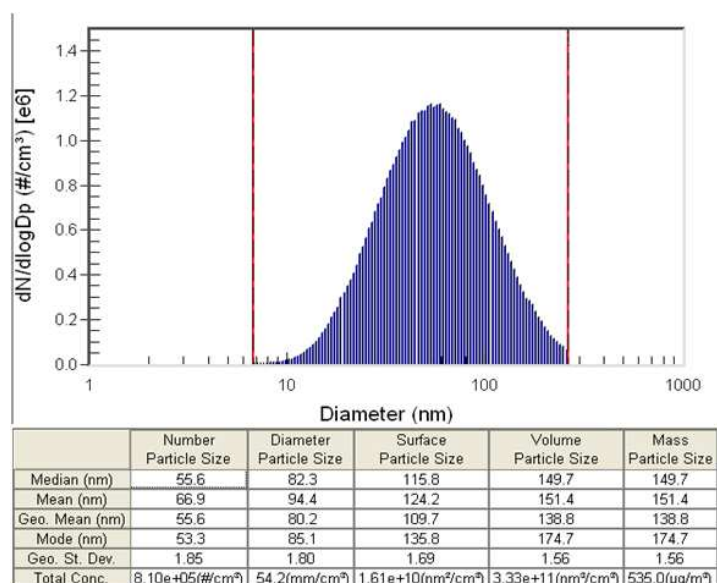


Figure 4.56: Size distributions for mixture D at 21% and 80% RH, respectively

### 4.3.18 Mixture E: Glutaric, Maleic, Tartaric, and Malonic Acids



**Figure 4.57:** Hygroscopic growth curves for mixture E: glutaric, maleic, tartaric, and malonic acids



**Figure 4.58:** Full distribution for a 1 g/L mixture E solution

Mixture E was comprised of glutaric, maleic, tartaric and malonic acids. As can be seen from Figure 4.57, the mixture grew hygroscopically, overall. However, the mean and geometric mean experienced a sharp increase around 70%, which could be considered a deliquescence point. This increase was also seen in the pure maleic acid sample and can be concluded that maleic acid has a strong influence on the mixture. Although not as active as UNIFAC predicted, the mixture followed the trend line provided by Moore. The average maximum growth factor was  $1.31 \pm 0.17$ .

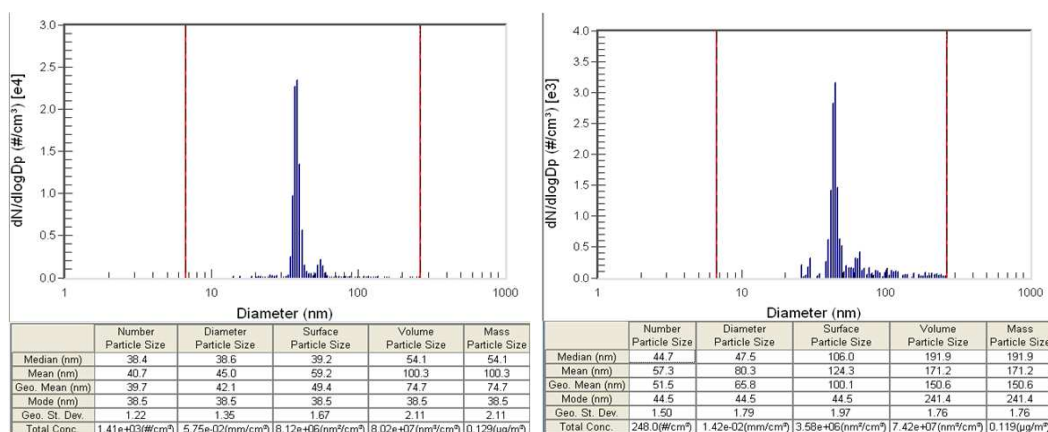


Figure 4.59: Size distributions for mixture E at 16% and 80% RH, respectively

### 4.3.19 Mixture F: Adipic, Aspartic, Phthalic and Azelaic Acids

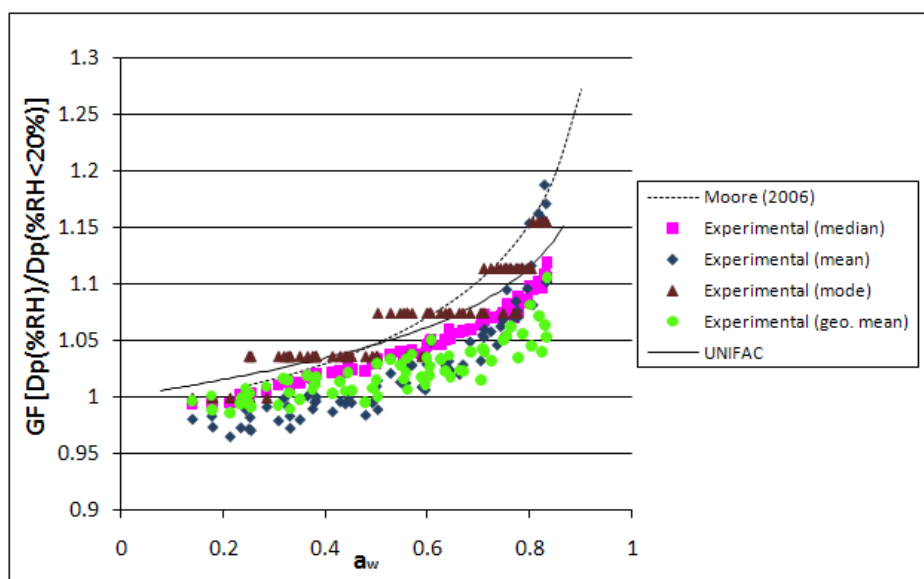
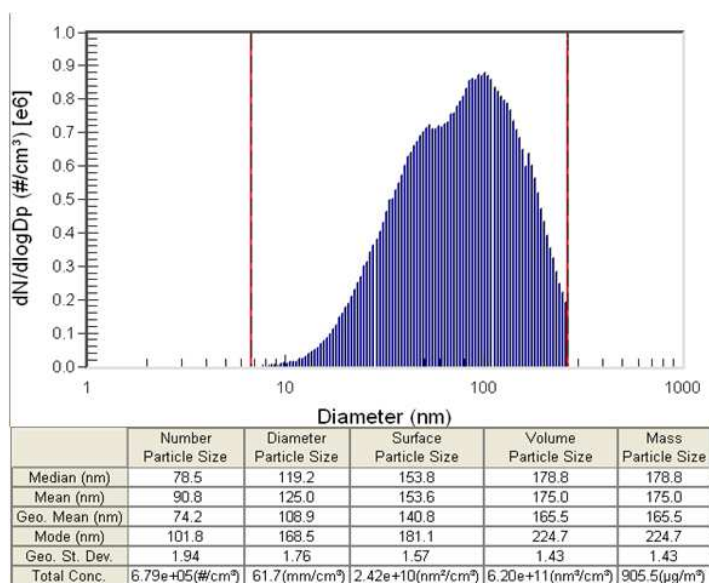


Figure 4.60: Hygroscopic growth curves for mixture F: adipic, aspartic, phthalic and azelaic acids



**Figure 4.61:** Full distribution for a 1 g/L mixture F solution

Mixture F was composed of adipic, aspartic, phthalic and azelaic acids. While UNIFAC had the same trend as all the average growth curves, both UNIFAC and Moore's trend line seemed to fit the modal growth curve the best. The full distribution (Figure 4.61) also appeared to have bimodal behavior, which could also be found with mixture D. Two common components between the mixtures are adipic and aspartic. As neither of these two pure components showed this trend, it can be inferred that some interaction between the two is causing the unusual distributions and that adipic may have the greater influence, as its pure component full distribution was not perfectly normal. The average maximum growth factor for all the averages was  $1.14 \pm 0.03$ .

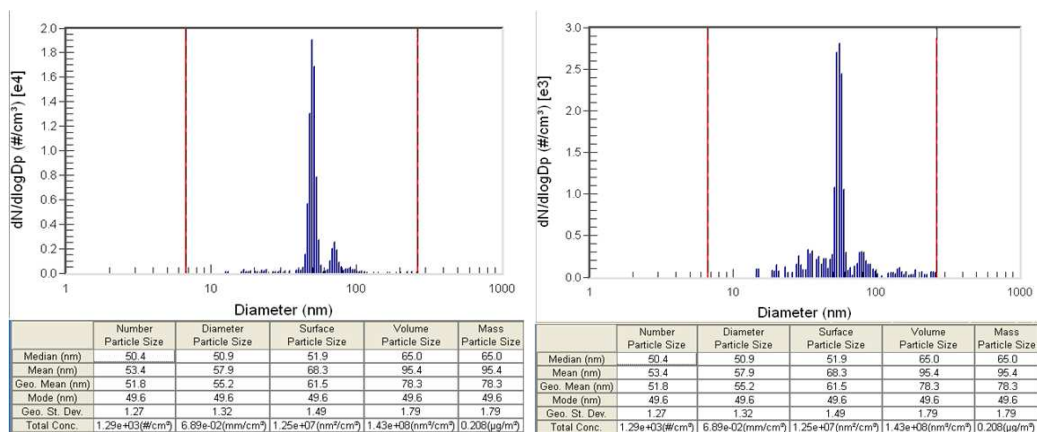


Figure 4.62: Size distributions for mixture F at 13% and 80% RH, respectively

### 4.3.20 Mixture G: Phthalic and Azelaic Acids

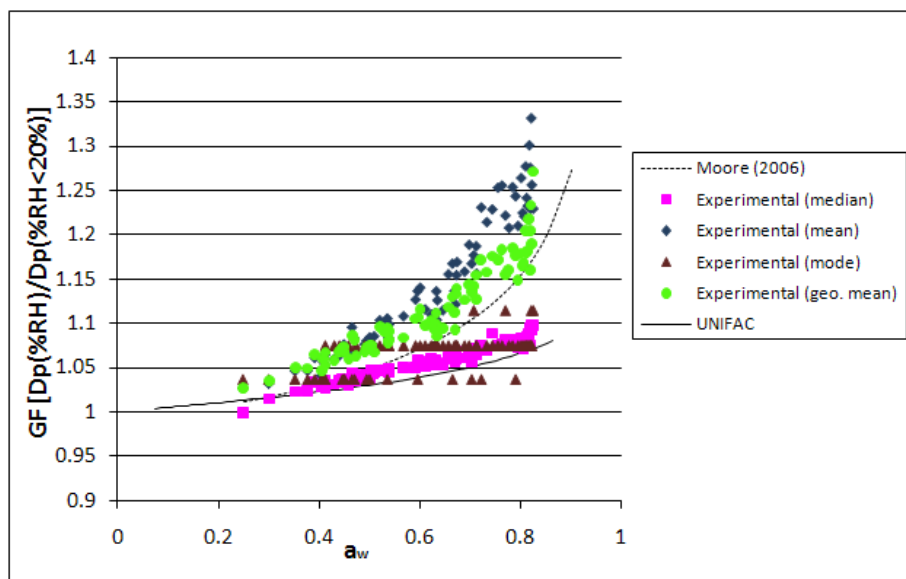
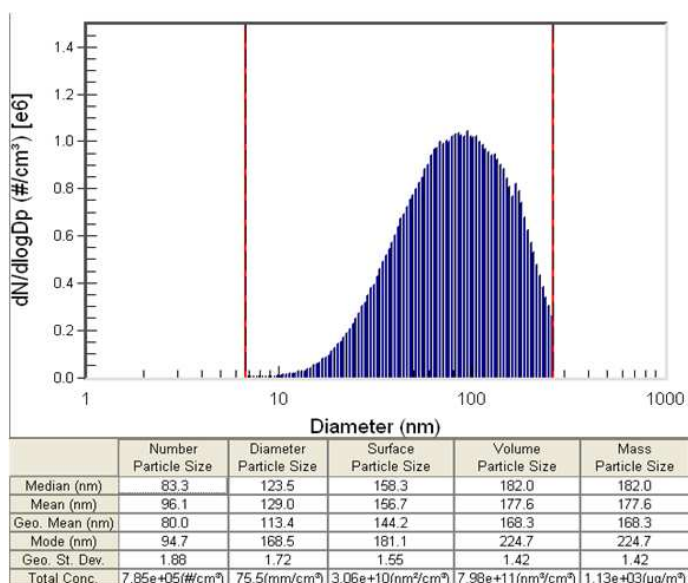


Figure 4.63: Hygroscopic growth curves for mixture G: phthalic and azelaic acids



**Figure 4.64:** Full distribution for a 1 g/L mixture G solution

Mixture G was formed from two organic acids: phthalic acid and azelaic acid. Although UNIFAC best fit the modal distribution, it followed the trend of the median well. The line formed by Moore best follows the trend of the mean and geometric mean, even though the experimental data for this study was more active than the trend predicts. The distributions for mixture G were normal and the average maximum growth factor for all the averages was  $1.23 \pm 0.11$ .

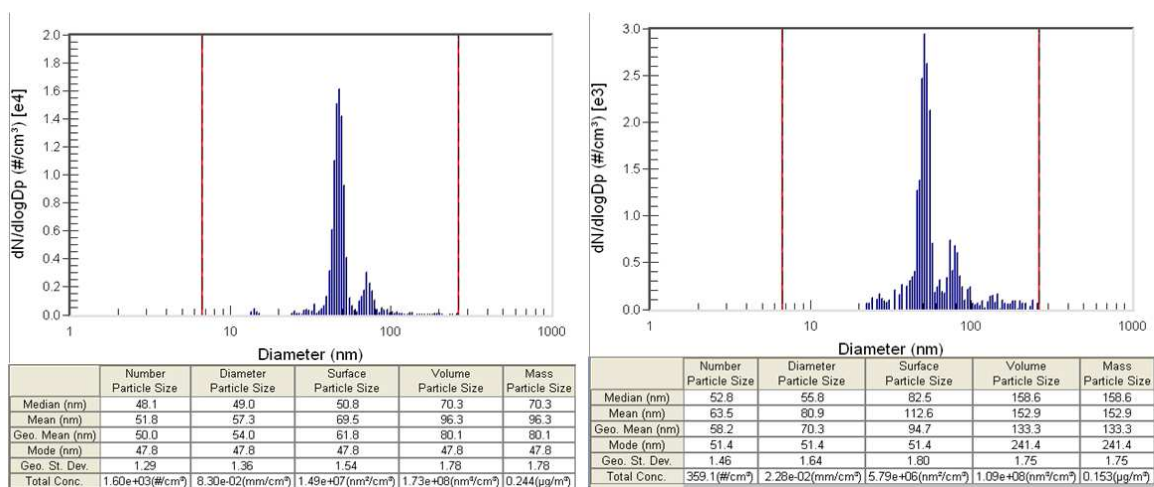


Figure 4.65: Size distributions for mixture G at 8% and 80% RH, respectively

### 4.3.21 Mixture H: Tartaric and Malonic Acids

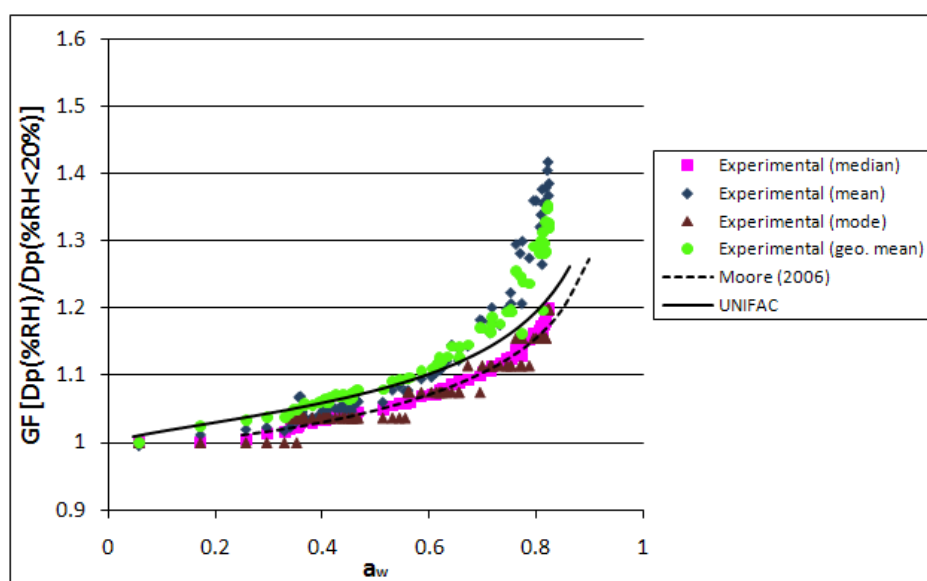
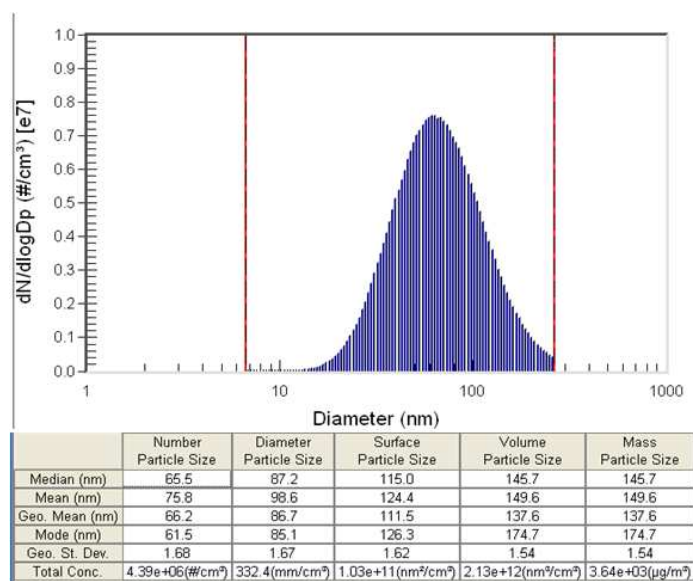
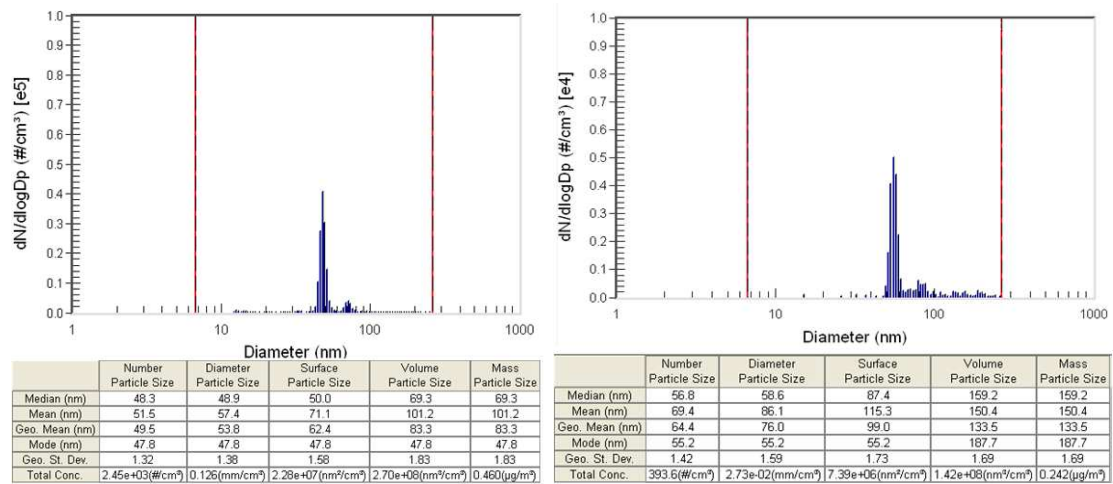


Figure 4.66: Hygroscopic growth curves for mixture H: tartaric and malonic acids



**Figure 4.67:** Full distribution for a 1 g/L mixture H solution

Mixture H was also composed of two organic acids: tartaric acid and malonic acid. The growth of this mixture was hygroscopic in nature and followed UNIFAC and Moore's trend line well. The mean and geometric mean appear to have experienced more growth than either of the fits, which is seen in Figure 4.68, where the concentration of larger particles increased at higher relative humidity. The average maximum growth factor across all averages was  $1.29 \pm 0.11$ .



**Figure 4.68:** Hygroscopic Growth Curves for Mixture H at 6% and 81% RH, respectively

### 4.3.22 Fitted Curves

As the mode and geometric mean are typically published growth factors, the mode and geometric mean for all the mixtures were combined and a fit was created to describe the data trends.

Richard Moore previously characterized his mixtures with the curve fit:

$$GF = A + Be^{C \cdot \%RH} + De^{E \cdot \%RH} \quad (4.2)$$

where the parameters are:

$$A = 0.9717$$

$$B = 0.0202$$

$$C = 0.0265$$

$$D = 1.86 \cdot 10^{-8}$$

$$E = 0.17$$

For this study, curves that best describe the mode and geometric mean for all the mixtures with increasing relative humidity are shown in Figures 4.69 and 4.70. These equations were adaptations of Moore's results so that a direct comparison could be made. A direct comparison of the equations has been made below where the constants have been fit to the general equation shown in Equation 4.2.

**Table 4.3:** Curve Fit Parameters

| Constants | Moore's Fit          | Experimental |                   |
|-----------|----------------------|--------------|-------------------|
|           |                      | Mode         | Geometric Mean    |
| A         | 0.9717               | 0.99         | 0.9702            |
| B         | 0.0202               | 0.003        | 0.0202            |
| C         | 0.0265               | 0.05         | 0.03              |
| D         | $1.86 \cdot 10^{-8}$ | -            | $3 \cdot 10^{-7}$ |
| E         | 0.17                 | -            | 0.17              |

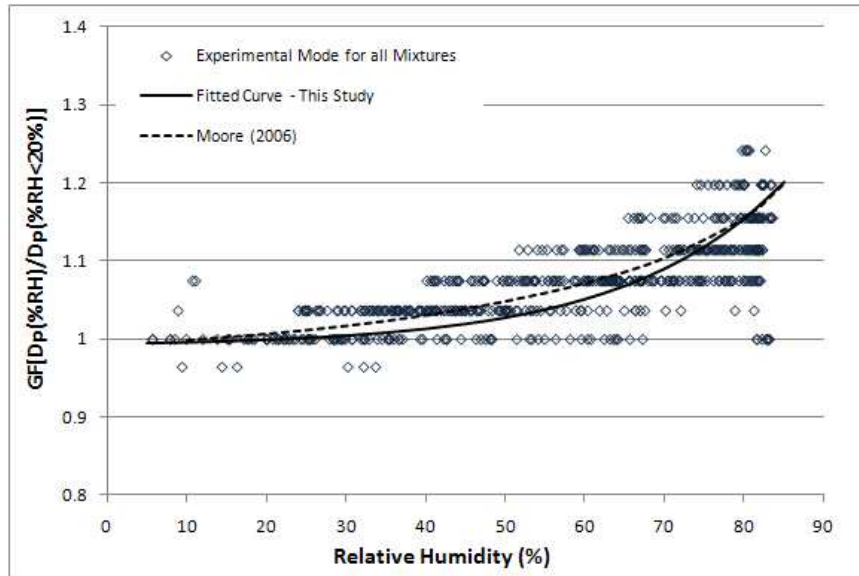


Figure 4.69: Curved fit for the mode growth factors of all mixtures

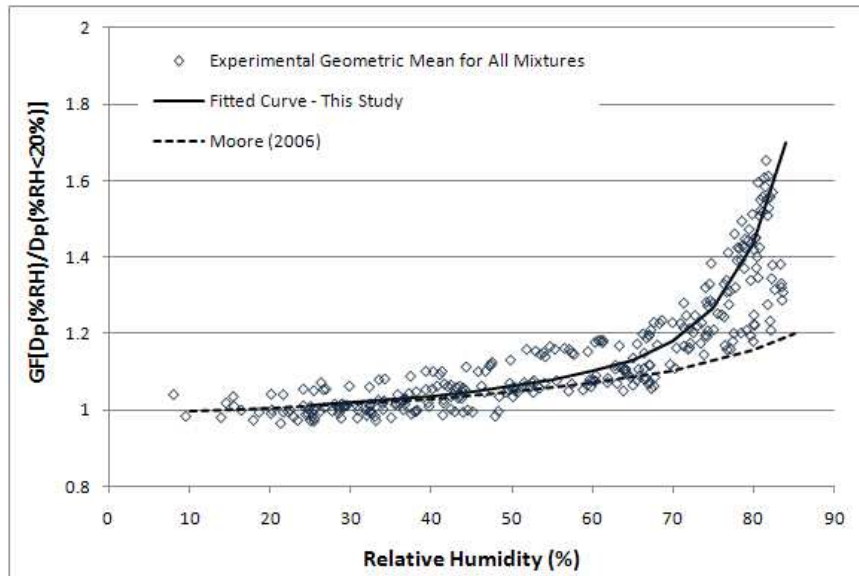


Figure 4.70: Curved fit for the geometric mean growth factors of all mixtures

### 4.3.23 Kappa Values

Petters and Kreidenweis (2007) developed a single parameter to relate particle dry diameters and cloud condensation nuclei (CCN),  $\kappa$ . This parameter was applied to 25 components, 8 of which were used in this study. Lower values of  $\kappa$  describe components that exhibit less hygroscopic or less CCN-active behavior. As this study did not have a CCN focus, the following  $\kappa$  values were determined for the HTDMA system and tabulated in Table 4.4. These values were calculated for the mode and geometric mean of the distributions, as these are recognized as the most widely published indicators of distribution behavior. The growth factor derived  $\kappa$ s for Petters and Kreidenweis were calculated at the highest measured water activity ( $a_w \sim 0.9$ ). As not all components could be studied above 80%,  $\kappa$  values were determined for  $a_w$  0.7 for adipic acid, aspartic acid, and the geometric mean of mixture B. For the results in Table 4.4, the  $\kappa$ s were defined for a water activity above 80%, with exception of those noted. Experimental values were further expressed in bar-graph form in Figures 4.71 and 4.72, where the error bars represent one standard deviation from the mean.

**Table 4.4:** Experimental Kappa Values

| Compound          | Mode |         |      |      | Geo. Mean |         |      |      |
|-------------------|------|---------|------|------|-----------|---------|------|------|
|                   | Avg. | St.Dev. | Min  | Max  | Avg.      | St.Dev. | Min  | Max  |
| Ammonium Chloride | 0.19 | 0.03    | 0.16 | 0.25 | 0.25      | 0.06    | 0.17 | 0.37 |
| Ammonium Nitrate  | 0.24 | 0.05    | 0.18 | 0.31 | 0.50      | 0.09    | 0.42 | 0.60 |
| Ammonium Sulfate  | 0.37 | 0.04    | 0.30 | 0.45 | 0.33      | 0.03    | 0.26 | 0.39 |
| Calcium Chloride  | 0.24 | 0.04    | 0.17 | 0.27 | 1.21      | 0.11    | 1.09 | 1.35 |
| Sodium Chloride   | 1.12 | 0.11    | 0.96 | 1.37 | 1.44      | 0.12    | 1.22 | 1.61 |
| Adipic Acid*      | 0.05 | 0.01    | 0.03 | 0.06 | 1.36      | 0.58    | 0.75 | 2.70 |
| Aspartic Acid*    | 0.26 | 0.04    | 0.19 | 0.33 | 0.88      | 0.14    | 0.63 | 1.20 |
| Azelaic Acid      | 0.04 | 0.01    | 0.03 | 0.06 | 0.09      | 0.03    | 0.05 | 0.02 |
| Maleic Acid       | 0.15 | 0.04    | 0.10 | 0.23 | 0.03      | 0.01    | 0.01 | 0.04 |
| Malonic Acid      | 0.28 | 0.06    | 0.16 | 0.50 | 0.31      | 0.09    | 0.19 | 0.49 |
| Phthalic Acid     | 0.07 | 0.02    | 0.05 | 0.10 | 0.45      | 0.11    | 0.28 | 0.60 |
| Succinic Acid     | 0.14 | 0.07    | 0.07 | 0.22 | 0.07      | 0.01    | 0.02 | 0.21 |
| Tartaric Acid     | 0.11 | 0.01    | 0.09 | 0.13 | 0.20      | 0.03    | 0.15 | 0.27 |
| Mixture A         | 0.14 | 0.03    | 0.11 | 0.19 | 0.20      | 0.06    | 0.13 | 0.30 |
| Mixture B*        | -    | -       | -    | -    | 0.40      | 0.08    | 0.31 | 0.59 |
| Mixture C         | 0.09 | 0.01    | 0.06 | 0.09 | 0.33      | 0.07    | 0.22 | 0.47 |
| Mixture D         | 0.43 | 0.07    | 0.35 | 0.51 | 0.35      | 0.08    | 0.28 | 0.45 |
| Mixture E         | 0.12 | 0.02    | 0.09 | 0.14 | 0.32      | 0.05    | 0.28 | 0.39 |
| Mixture F         | 0.10 | 0.01    | 0.09 | 0.11 | 0.05      | 0.02    | 0.03 | 0.07 |
| Mixture G         | 0.06 | 0.01    | 0.05 | 0.08 | 0.16      | 0.03    | 0.12 | 0.22 |
| Mixture H         | 0.13 | 0.01    | 0.12 | 0.15 | 0.27      | 0.04    | 0.16 | 0.32 |

\*-  $\kappa$  values were computed for above 70% RH. Mixture B experimental mode did not experience enough growth to calculate  $\kappa$  values.

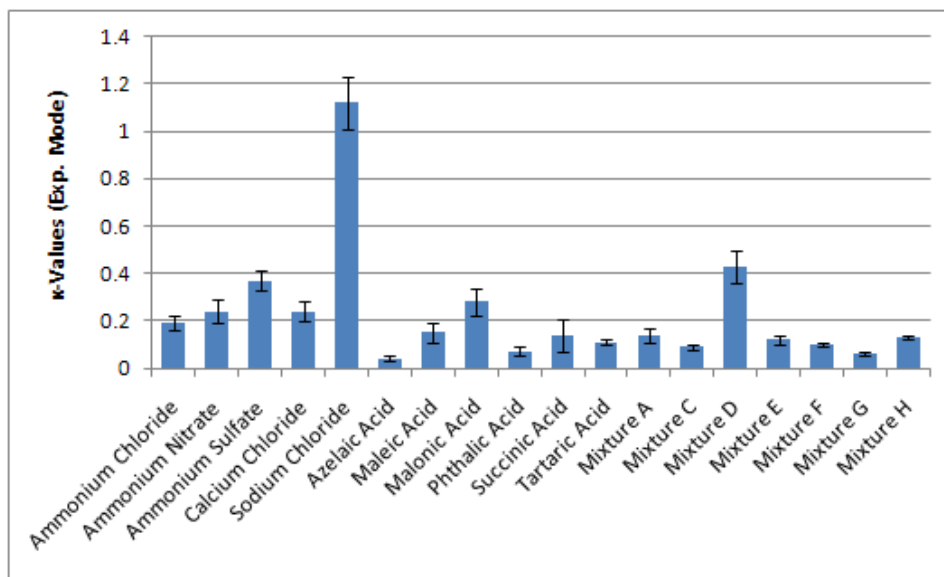


**Figure 4.71:** Experimental Kappa Values for the Mode

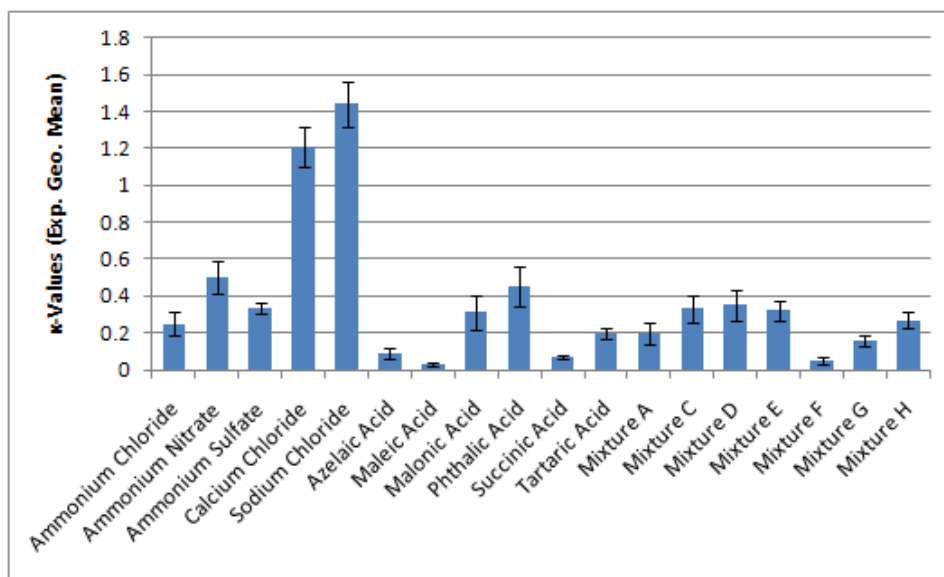


**Figure 4.72:** Experimental Kappa Values for the Geometric Mean

The results published by Petters and Kreidenweis (2007) for the components in

this study are tabulated below.

**Table 4.5:** Petters and Kreidenweis (2007) Kappa Values

| Compound         | $\kappa_{low}$    | $\kappa_{mean}$     | $\kappa_{up}$     |
|------------------|-------------------|---------------------|-------------------|
| Ammonium Nitrate | N/A               | N/A                 | N/A               |
| Ammonium Sulfate | 0.33 <sup>a</sup> | 0.53                | 0.72 <sup>a</sup> |
| Sodium Chloride  | 0.91 <sup>a</sup> | 1.12 <sup>b</sup>   | 1.33 <sup>a</sup> |
| Adipic Acid      | N/A               | <0.006 <sup>d</sup> | N/A               |
| Glutaric Acid    | 0.12              | 0.2 <sup>a</sup>    | 0.28              |
| Malonic Acid     | 0.28              | 0.44 <sup>a</sup>   | 0.6               |
| Phthalic Acid    | N/A               | <0.059 <sup>e</sup> | N/A               |
| Succinic Acid    | N/A               | <0.006 <sup>c</sup> | N/A               |

<sup>a</sup> Koehler *et al.* (2006) - range of  $\kappa$  from Table 3

<sup>b</sup> Clegg and Wexler (1998) - Aerosol Inorganic Model

<sup>c</sup> Chan and Chan (2003) -  $\kappa$  estimated from mass GF for succinic acid was below detection limit

<sup>d</sup> Prenni *et al.* (2003) - GF's for adipic acid were below detection limit

<sup>e</sup> Huff Hartz *et al.* (2006) - mass GF were converted to size GF

When comparing this study's data (Table 4.4) to that of published values (Table 4.5

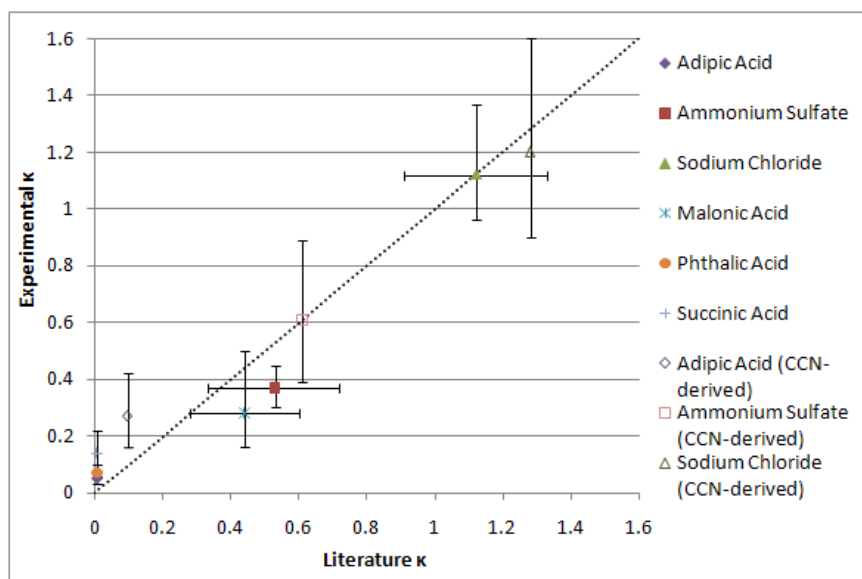


**Figure 4.73:** Comparison of Experimental and Literature Kappa Values

and Figure 4.73), it can be noted that HTDMA-derived sodium chloride and CCNC-derived ammonium sulfate exhibited similar behavior for both this study and literature data. Sodium chloride had the highest  $\kappa$  values in both data sets, while adipic acid did not experience enough growth for  $\kappa$  values to be calculated for either set above 80% RH. However,  $\kappa$  values could be calculated in this study for adipic acid above 70% RH. The largest discrepancy between the two studies is with phthalic acid. Huff Hartz *et al.* (2006) published nearly negligible  $\kappa$  values. In this study, values could be calculated; however, they were considerably lower than most organic acids and their mixtures. As phthalic acid was a component in mixtures F and G, the mixtures had resulting lower  $\kappa$ s. Error bars for Figure 4.73 are of the minimum and maximum experimental kappa values, rather than standard deviation, to better observe the range in the data.

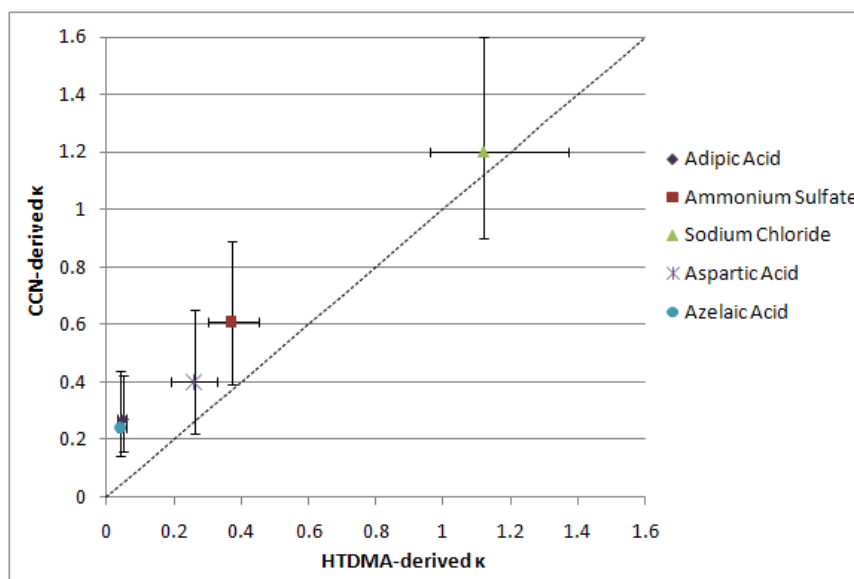


**Figure 4.74:** Comparison of HTDMA-derived and CCN-derived Kappa Values

Figure 4.74 illustrates a comparison of kappa values between two experimental systems: HTDMA and CCNC. For every component, the CCNC-derived kappa value was higher than that of the HTDMA value. This trend was expected as a particle can activate more readily in a super-saturated environment than in a sub-saturated environment. Sodium chloride exhibited slightly less activation signifying that sodium chloride is not as susceptible to water interactions as the other studied species.

#### 4.3.24 Summary

Several conclusions can be made from trials performed with the HTDMA system. The most interesting of which was significant changes in adipic, azelaic and succinic acid morphology. All three of these acids are linear dicarboxylic acids with varying

degrees of chain length. Succinic acid has been known to form plate-like crystal shapes. Once water adsorbs to the particle surfaces, the plate-like structure begins to turn into a spherical droplet. This change in morphology was drastic enough to be seen in the distributions, as well as the growth curves. It is also interesting to note the strong influence maleic acid has on mixtures. In its pure form, maleic acid appears to exhibit deliquescent behavior. When in a mixture, there are stronger increases in growth curves to match that of maleic acid. Mixture C best describes this behavior and while other mixtures containing maleic acid show some effect, the influence is diluted due to the larger number of compounds. In fact, the more components the mixtures contained, the less unusual behavior was exhibited as the mixture behavior seemed to converge, especially for those mixtures containing succinic and/or maleic acids.

It was noted that mixtures containing few components seemed to have stronger increase in growth over those mixtures with more than 2 or 3 components, which grew more slowly and steadily. Shape factors were used to account for changes in morphology of particles, specifically ammonium sulfate and sodium chloride. The DMAs determine particle size based on electrical mobility and therefore, lack the ability to detect and account for changes in morphology.

## Chapter 5

# Conclusions and Recommendations

### 5.1 Conclusions

Inorganic aerosols properties have been studied extensively and well-characterized while only recent studies have examined the effects of organics with respect to aerosol-water interactions. While other experimental techniques are able to capture bulk hygroscopic properties, few, if any, are able to capture morphological changes associated with deliquescence and hygroscopic growth. The ESEM provides this advantage over typical experiments (e.g. flow cell, electrodynamic balance, TDMA). The majority of past experimentation also focused on either pure substances or mixtures up to three components, inorganics or organics. In this HTDMA study, organic mixtures up to five components were analyzed.

### 5.1.1 ESEM

Using the ESEM to analyze *in-situ* growth of aerosols is a novel, useful tool for hygroscopic and morphological studies. For this study, particle growth was assessed quantitatively (DRH, GFs) and qualitatively (morphologically) for ammonium sulfate, ammonium chloride, calcium chloride, sodium chloride, glutaric acid and malonic acid aerosols. Moore (2006) previously studied pure component particles within 800 nm-2  $\mu\text{m}$  diameter size range. To create a full data set and more realistic model for potential aerosol sizes, this study analyzed the same component particles up to 10  $\mu\text{ms}$ .

Overall, the hygroscopic growth of components in this study were consistent with that by published literature. In some cases, the experimental DRH was higher than that of other studies, which can be explained by the temperature-dependence of the component. In the case of sodium chloride, the DRH was lower than expected due to earlier onset of water adsorption, which was seen in the ESEM, but is not quantified in bulk measurement studies. Ammonium sulfate experienced both initial growth before that of the reported DRH and continued to grow at a value higher than the reported DRH.

The main complications from this system occurred at higher relative humidity environments within the microscope when imaging and subsequent analysis became difficult due to the hydrophilic nature of certain particles. As water uptake increased, it became more difficult to discern the particle edge from the substrate. Thus, organic acids and strongly hydrophilic components were difficult to image and analyze.

### 5.1.2 HTDMA

The humidification section for the HTDMA system was created from laboratory materials. To verify the experimental technique, ammonium sulfate and sodium chloride were tested and DRH and GF values were compared to that of literature. Several conclusions can be made from trials performed with the HTDMA system. The most interesting of which was significant changes in adipic, azelaic and succinic acid morphology. All three of these acids are linear dicarboxylic acids with varying degrees of chain length. Succinic acid has been known to form plate-like crystal shapes. Once water adsorbs to the particle surfaces, the plate-like structure begins to turn into a spherical droplet. This change in morphology was drastic enough to be seen in the distributions, as well as the growth curves. It is also interesting to note the strong influence maleic acid has on mixtures. In its pure form, maleic acid appears to exhibit deliquescent behavior. When in a mixture, there are stronger increases in growth curves to match that of maleic acid. Mixture C best illustrates this behavior and while other mixtures containing maleic acid show some effect, the influence is diluted due to the larger number of compounds. In fact, the more components the mixtures contained, the less unusual behavior was exhibited as the mixture behavior seemed to converge, especially for those mixtures containing succinic and/or maleic acids.

It was noted that mixtures containing few components seemed to have stronger increase in growth over those mixtures with more than 2 or 3 components, which grew more slowly and steadily. Shape factors were used to account for changes in morphology of particles, specifically ammonium sulfate and sodium chloride. The DMAs determine particle size based on electrical mobility and therefore, lack the

ability to detect and account for changes in morphology.

## 5.2 Recommendations

While this study did provide insight into the hygroscopic and morphological properties of atmospheric aerosols, additional work can be done to better exploit the advantages of both experimental methods. First, as organics are large constituents in the atmosphere but are not well-characterized, more organic compounds should be studied in the ESEM. Additionally, organic mixtures and inorganic-organic mixtures should be created and studied in the ESEM for their component interactions and component-water interactions. This study should also be expanded to include ambient field samples to model more realistic atmospheric interactions.

More mixtures should be analyzed using the HTDMA system. Specifically, components of more varied structure and properties should be used as this study focused on dicarboxylic acids. HTDMA can elucidate the interactions of chemical species in bulk measurements and consequently, mixtures of increased complexity can serve as more realistic atmospherically relevant models. A better understanding of aerosol properties with larger component mixtures is necessary as current global climate and aerosol chemistry models lack the ability to account for the complications in chemistry. In addition to further experimentation, kappa values should be calculated and compared to that of current literature and cloud condensation nuclei (CCN) derived values.

# Chapter 6

## Appendix A

### 6.1 UNIFAC Model Derivations

Growth factors were calculated by comparing the size of particles during growth to that of the dry particle. The UNIFAC model calculates the mole fraction solute of a mixture as a function of water activity. This can then be converted to mass fraction solute ( $mfs$ ) and further converted to growth factor (GF) through:

$$GF = \left[ \frac{\rho_s \left( \frac{mfs}{\rho_s} + \frac{1-mfs}{\rho_w} \right)}{mfs} \right]^{1/3} \quad (6.1)$$

where  $\rho_s$  is the dry solute density and  $\rho_w$  is the density of water. The mass fraction

solute (mfs) was defined as:

$$mfs = \frac{x_p MW_p}{x_p MW_p + x_w MW_w} \quad (6.2)$$

where the mole fraction water was used by UNIFAC to determine corresponding growth factors (GF).

UNIFAC model splits up the activity coefficient for each component in the system into two components: a combinatorial  $\gamma^C$  and a residual component  $\gamma^R$ . The total activity coefficient for water is related to the two components as shown in here:

$$\ln \gamma_w = \ln \gamma_w^C + \ln \gamma_w^R \quad (6.3)$$

$$\ln \gamma_w^C = \ln \left( \frac{\phi_w}{x_w} \right) + 5q \ln \left( \frac{\theta_w}{\phi_w} \right) + L - \frac{\phi_w}{x_w} \sum (x_i L_i) \quad (6.4)$$

$$\theta_i = \frac{x_i q_i}{\sum_{j=1}^n x_j q_j} \quad (6.5)$$

$$\phi_i = \frac{x_i r_i}{\sum_{j=1}^n x_j r_j} \quad (6.6)$$

$$L = \frac{z}{2} (r - q) - (r - 1); z = 10 \quad (6.7)$$

$\theta_i$  and  $\phi_i$  are defined as the molar weighted segment and area fractional components for molecule  $i$  of the total system.  $L$  is a compound parameter that is defined by the Van der Waals volume ( $r$ ) and the Van der Waals molecular square area ( $q$ ).  $z$  is the coordination number that is frequently published as having a constant value of 10 due to the insensitivity of the model.

The residual component of the activity coefficient is a function of the functional groups and has been previously identified for the investigated organic species by Reid *et al* (1987) and for inorganic species by Erdakos *et al* (2006).

Finally, the activity coefficient for water can be calculated into a water activity through the following equation:

$$a_w = x_w \gamma_w \quad (6.8)$$

### 6.1.1 Summary

To form a theoretical growth factor model, the UNIFAC model was employed. For this study, the mole fraction of water and the mole fractions of the components involved were known. UNIFAC was used to calculate activity coefficients ( $\gamma_w$ ) through the use of binary interaction parameters in Equation 6.3. For a given mole fraction of water ( $x_w$ ) and a calculated activity

coefficient, the water activity for the system was calculated using Equation 6.8. By using the mole fraction of water and mole fractions of components in the system, the mass fraction solute (mfs) of the system was calculated from Equation 6.2, which was used to determine growth factors (Equation 6.1). To create a growth factor curve, growth factors were plotted against water activity.

# Chapter 7

## Appendix B

### 7.1 Aerosol Distributions

The following figures represent each distribution of data prior to size-selection.

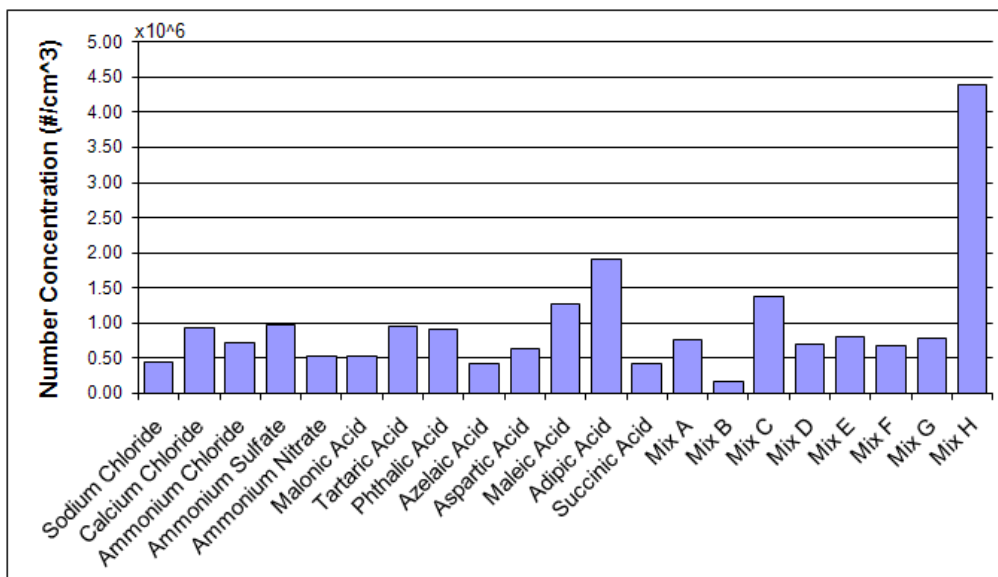


Figure 7.1: Number concentration of HTDMA solutions

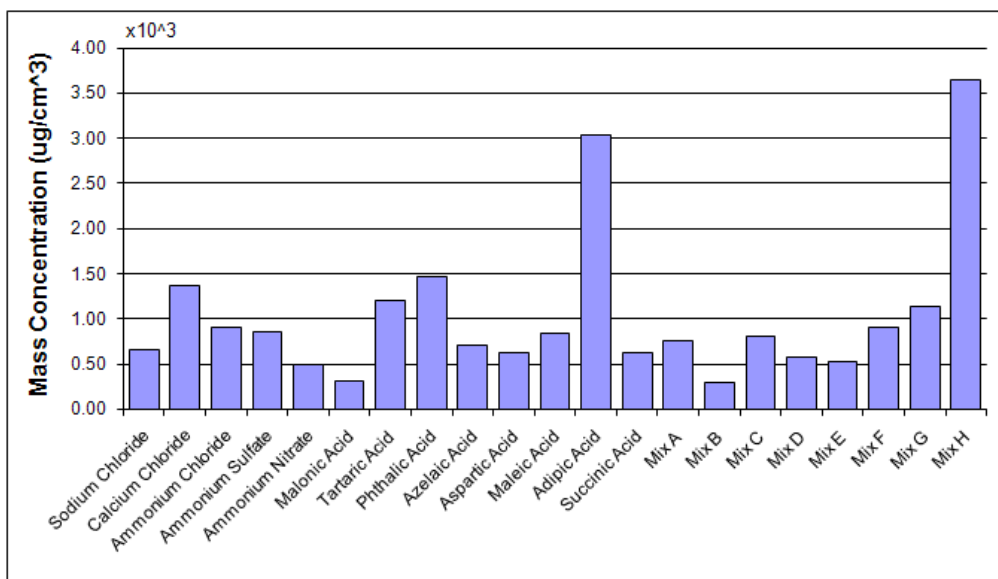
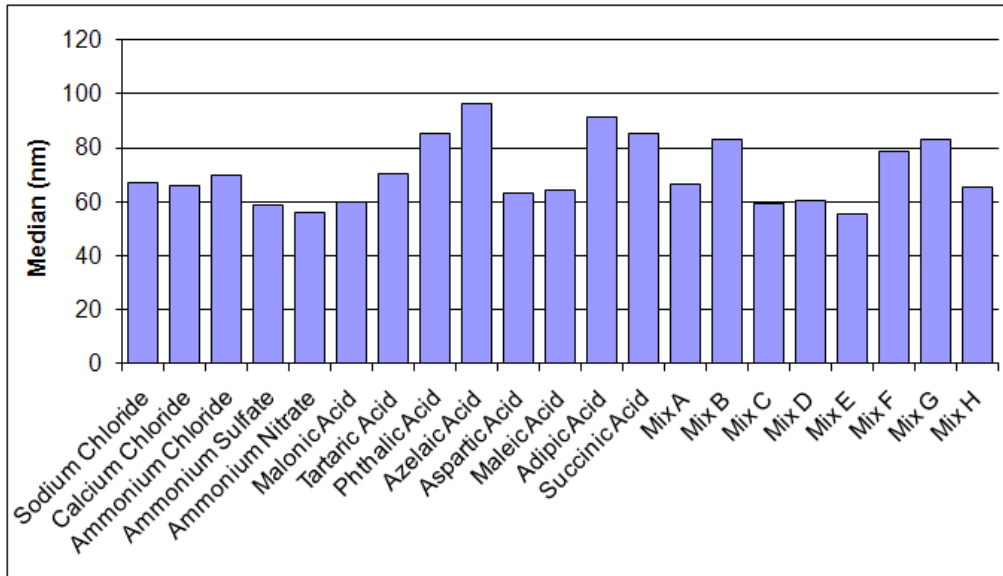
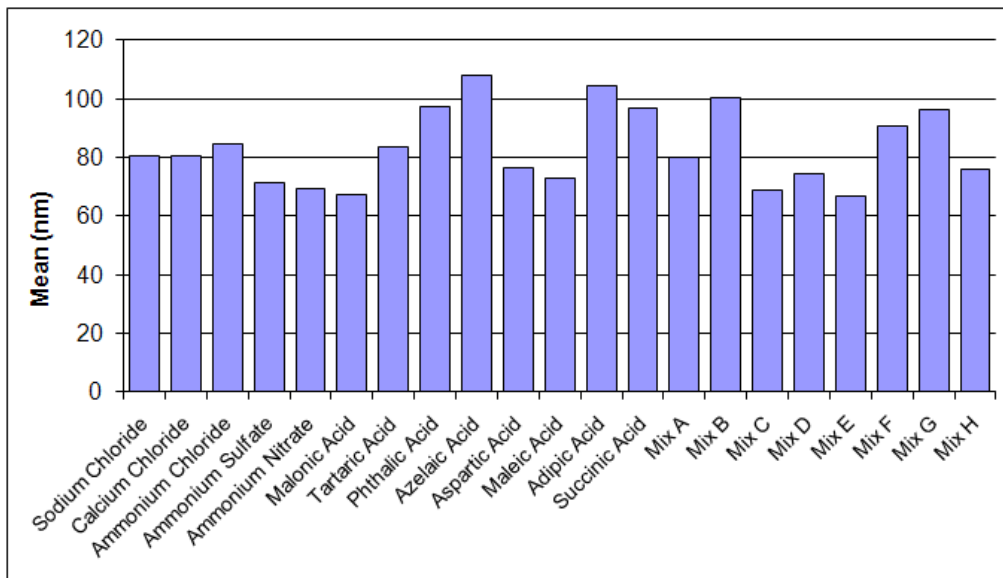


Figure 7.2: Mass concentration of HTDMA solutions



**Figure 7.3:** Median of HTDMA solution distributions



**Figure 7.4:** Mean of HTDMA solution distributions

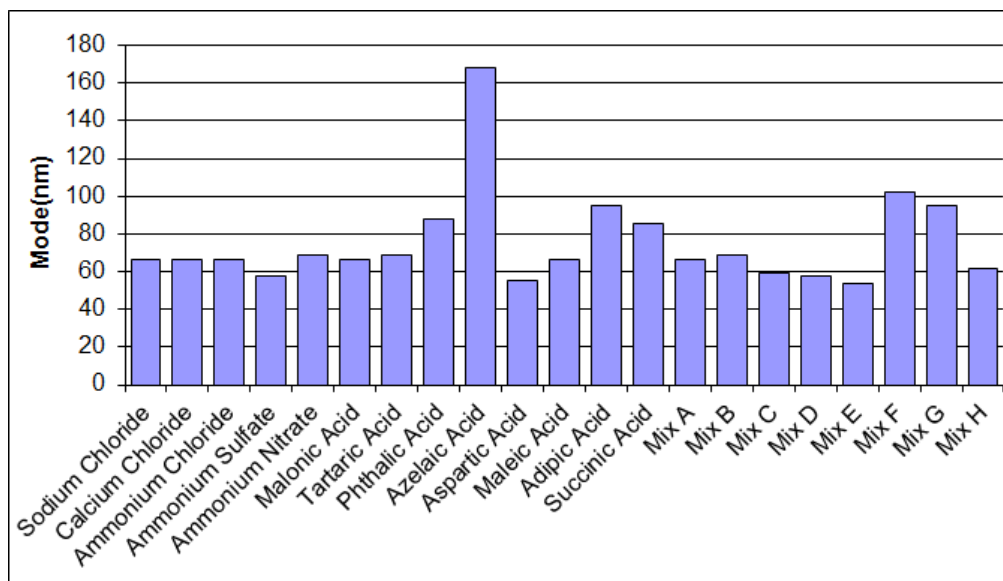


**Figure 7.5:** Mode of HTDMA solution distributions

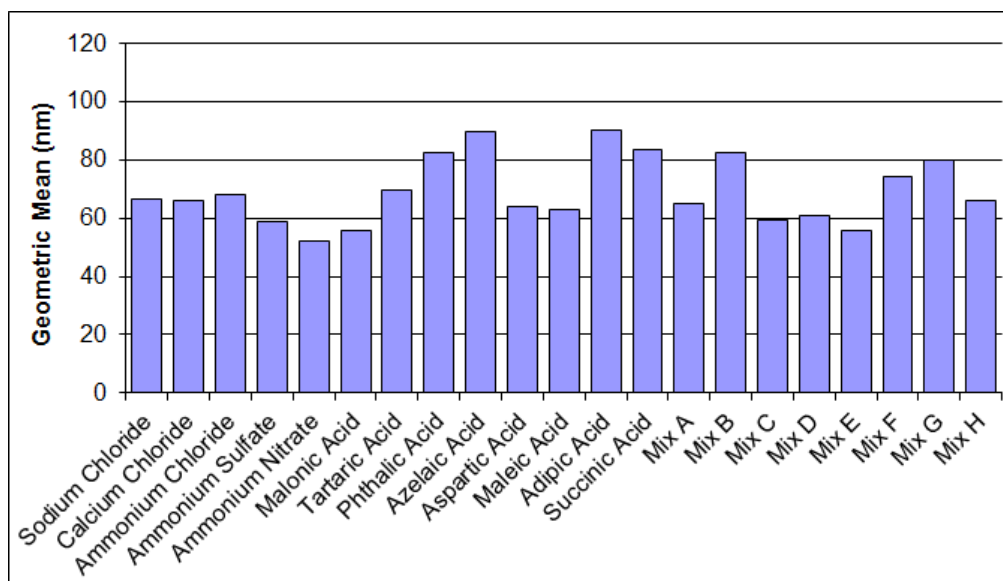


**Figure 7.6:** Geometric mean of HTDMA solution distributions

## Chapter 8

### Appendix C

#### 8.1 Atomic Force Microscopy Images of Studied Components

The following images were developed and published in a thesis entitled, "Morphology and Cloud Condensation Nuclei Activity of Single-Component and Multi-Component Organic Aerosols" by Juan Lopez Ruiz (2009) and can be used to distinguish morphological effects between components.

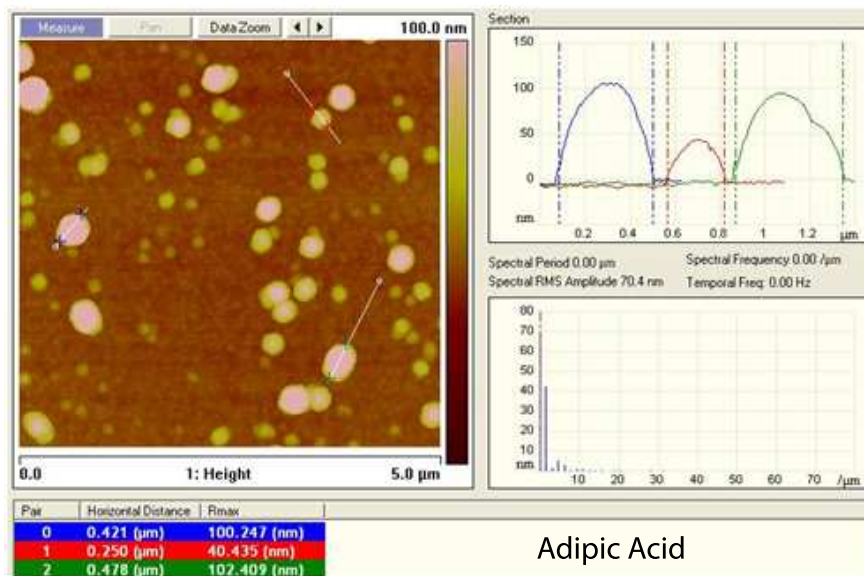


Figure 8.1: AFM images of Adipic Acid

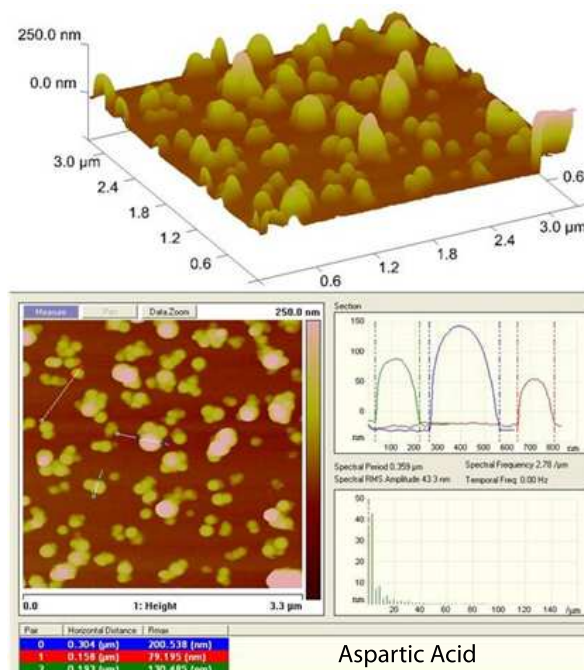


Figure 8.2: AFM images of Aspartic Acid

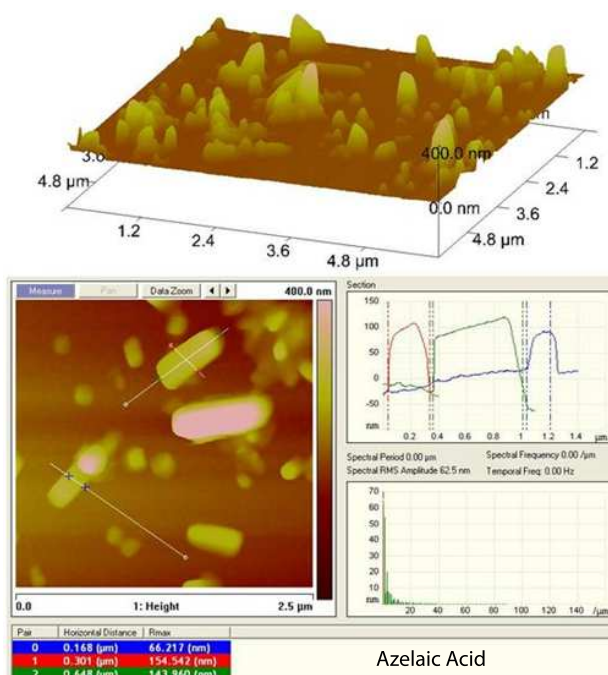


Figure 8.3: AFM images of Azelaic Acid

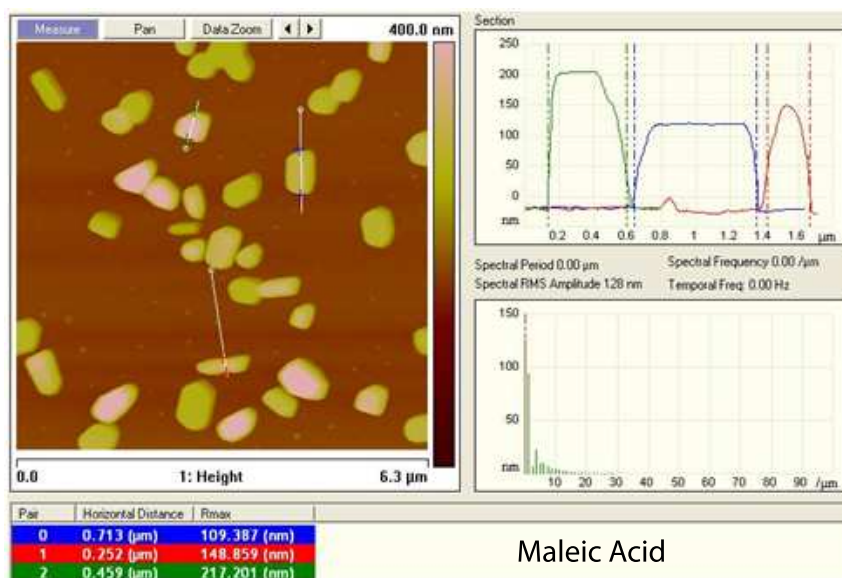


Figure 8.4: AFM images of Maleic Acid

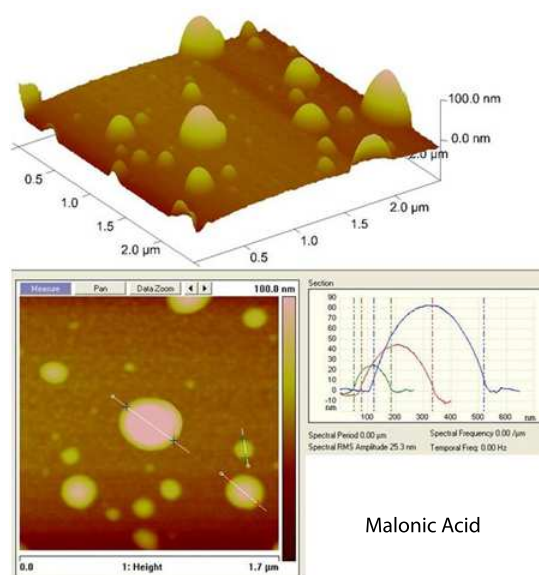


Figure 8.5: AFM images of Malonic Acid

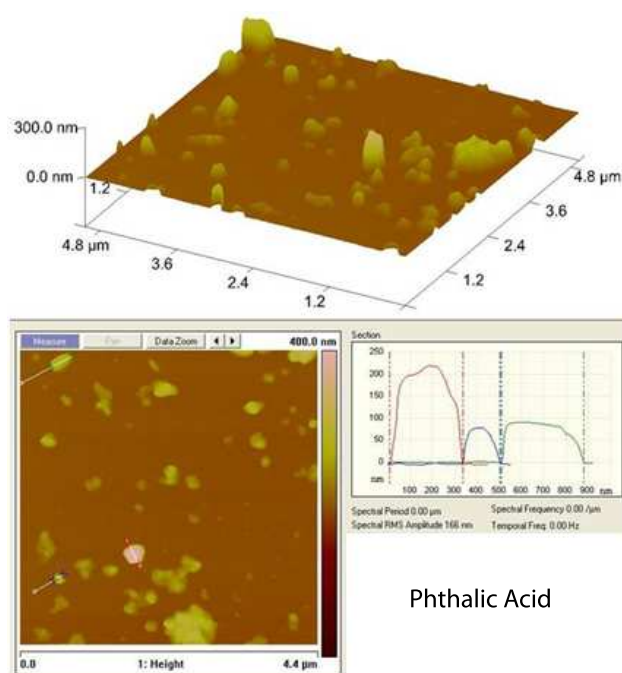


Figure 8.6: AFM images of Phthalic Acid

### 8.1.1 Summary

As suspected, adipic and azelaic acid showed significant elongation to cause charging effects in the HTDMA system. Adipic acid was interesting in this data as it first appears to exhibit spherical morphology. Despite this, it still experiences exaggerated elongation that can affect the charge distribution of the DMAs. Aspartic, phthalic and malonic acids had nearly spherical or round morphologies and maleic acid had a noticeably low aspect ratio.

## References

- [1] J. H. Seinfeld and S. N. Pandis, *Atmospheric Chemistry and Physics. From Air Pollution to Climate Change*. (John Wiley Sons, Inc., New York, NY, 1998).
- [2] J. E. Penner, M. Andreae, H. Annegarn, L. Barrie, J. Feichter, D. Hegg, A. Jayaraman, R. Leaitch, D. Murphy, J. Nganga, and G. Pitari, “Aerosols, their direct and indirect effects,” IPCC WGI Third Assessment Report (2000).
- [3] K. T. Whitby and B. K. Cantrell, “Atmospheric aerosols: Characteristics and measurements,” IEEE; ICESA (1976).
- [4] S. M. Wall, W. John, and J. L. Ondo, “Measurement of aerosol size distributions for nitrate and major ionic species,” *Atmospheric Environment*, **22**, 1649 (1988).
- [5] S. Solomon, D. Qin, M. Manning, Z. Chen, M. Marquis, K. B. Averyt, M. Tignor, and H. L. Miller, *Climate Change 2007: The Physical Science Basis. Contribution of Working Group I to the Fourth Assessment Report of the Intergovernmental Panel on Climate Change (IPCC)* (Cambridge University Press, Cambridge, United Kingdom; New York, NY, 2007).
- [6] C. Luo, C. Zender, H. Bain, and S. Metzger, “Role of ammonia chemistry and

- coarse mode aerosols in global climatological inorganic aerosol distributions,” *Atmospheric Environment*, **41** (2007).
- [7] P. Saxena and L. M. Hildemann, “Water-soluble organics in atmospheric particles: A critical review of the literature and application of thermodynamics to identify candidate compounds,” *Journal of Atmospheric Chemistry*, **24**, 57.
- [8] J. H. Seinfeld and J. F. Pankow, “Organic atmospheric particulate material,” *Annual Review of Physical Chemistry*, **54**, 121 (2003).
- [9] J. Ludwig and O. Klemm, “Organic acids in different size classes of atmospheric particulate material,” *Tellus*, **40B**, 340 (1988).
- [10] S. Twomey, “Aerosols, clouds, and radiation,” *Atmospheric Environment*, **25A** **11**, 2435 (1991).
- [11] H. Wex, F. Stratmann, and S. Hartmann, “Connecting hygroscopic growth at high humidities to cloud activation for different particle types,” .
- [12] H. R. Pruppacher and J. D. Klett, *Microphysics of Clouds and Precipitation* (Kluwer Academic Publishers, Boston, 1997).
- [13] G. McFiggans, M. R. Alfarra, J. Allan, K. Bower, H. Coe, M. Cubison, D. Topping, P. Williams, S. Decesari, C. Facchini, and S. Fuzzi, “Simplification of the representation of the organic component of atmospheric particulates,” *Faraday Discuss*, **130**, 341 (2005).
- [14] C. Marcolli, B. Luo, and T. Peter, “Mixing of the organic aerosol fractions: Liq-

- uids as the thermodynamically stable phases,” *Journal of Physics and Chemistry*, **108**, 2216 (2004).
- [15] P. H. McMurry, “A review of atmospheric aerosol measurements.” *Atmospheric Environment*.
- [16] M. E. Wise, J. D. Surratt, D. B. Curtis, J. E. Shilling, M. A., and Tolbert, “Hygroscopic growth of ammonium sulfate/dicarboxylic acids,” *Journal of Geophysical Research*, **108**, 4638 (2003).
- [17] D. O. Topping, B. McFiggans, H., and Coe, “A curved multi-component aerosol hygroscopicity model framework: Part 1 - inorganic compounds,” *Atmospheric Chemistry and Physics*, **5**, 1205 (2004).
- [18] S. M. Kreidenweis, K. Koehler, P. DeMott, J. Prenni, C. Carrico, B., and Ervens, “Water activity and activation diameters from hygroscopicity data - part 1: Theory and application to inorganic salts,” *Atmospheric Chemistry and Physics*, **5**, 1357 (2005).
- [19] R. K. Chakrabarty, H. Moosmuller, M. A. Garro, W. Arnott, S. Patrick, G. Jay, E. S. Cross, J.-H. Han, P. Davidovits, T. B. Onasch, and D. R. Worsnop, “Morphology based particle segregation by electrostatic charge,” *Journal of Aerosol Science*, **39**, 758 (2008).
- [20] P. A. Baron, C. M. Sorensen, and J. E. Brockmann, *Nonspherical Particle Measurements: Shape Factors, Fractals and Fibers*, p. 105, *Aerosol Measurements: Principles, Techniques, and Applications*, 2 ed. (Wiley-InterScience, Inc., 2001).

- [21] L. Kramer, U. Poschl, and R. Niessner, “Microstructural rearrangement of sodium chloride condensation aerosol particles on interaction with water vapor,” *Journal of Aerosol Science*, **31** **6**, 673 (2000).
- [22] C. M. Carrico, M. D. Petters, S. M. Kreidenweis, J. L. C. Jr., G. Engling, and W. C. Malm, “Aerosol hygroscopicity and cloud droplet activation of extracts of filters from biomass burning experiments,” *Journal of Geophysical Research*, **113** (2008).
- [23] M. Rhodes, *Introduction to Particle Technology* (John Wiley and Sons, England, 2008).
- [24] J. A. Bernstein, N. Alexis, C. Barnes, L. Bernstein, A. Nel, D. Peden, D. Diaz-Sanchez, S. M. Tarlo, and P. B. Williams, “Environmental and occupational respiratory disorders,” *American Academy of Allergy, Asthma and Immunology* (2004).
- [25] T. Incorporated, *Model 3450 Vibrating Orifice Aerosol Generator: Operation and Service Manual* (TSI Incorporated, Shoreview, MN, 2009).
- [26] G. Danilatos and R. Postle, “The environmental scanning electron microscope and its applications,” *Scanning Electron Microscopy*, p. 1 (1981).
- [27] J. M. Ficke and P. R. Lowe, “Technical paper 4-74,” .
- [28] G. Hanel, “Parametrization of the influence of relative humidity on optical aerosol properties,” *Aerosols and Their Climate Effects* (1984).

- [29] C. Pilinis, S. N. Pandis, and J. H. Seinfeld, "Sensitivity of direct climate forcing by atmospheric aerosols to aerosol size and composition," *J. Geophys. Res.*, **100**, 18739 (1995).
- [30] S. E. Schwartz, "The whitehouse effect - shortwave radiative forcing of climate by anthropogenic aerosols: an overview." *Journal of Aerosol Science*, **27**, 359 (1996).
- [31] C. Braun and U. K. Krieger, "Two-dimensional angular light-scattering in aqueous nacl single aerosol particles during deliquescence and efflorescence." *Optics Express*, **8**, 314 (2001).
- [32] R. J. Charlson, S. E. Schwartz, J. M. Hales, R. D. Cess, J. A. C. Jr., J. E. Hansen, and D. J. Hofmann, "Climate forcing by anthropogenic aerosols," *Science*, **255**, 423 (1992).
- [33] M. E. Wise, T. A. Semeniuk, R. Brintjes, S. T. Martin, L. M. Russell, and P. R. Buseck, "Hygroscopic behavior of nacl-bearing natural aerosol particles using environmental transmission electron microscopy," *J. Geophys. Res.*, **112** (2007).
- [34] O. V. Rattigan, M. I. Mirza, B. M. Ghauri, A. R. Khan, K. Swami, K. Yang, and L. Husain, "Aerosol sulfate and trace elements in urban fog," *Energy Fuels*, **3** 640-646 (2002).
- [35] J. L. Collett, A. Bator, D. E. Sherman, K. F. Moore, K. H. J., B. B. Demoz, X. Rao, and J. E. Reilly, "The chemical composition of fogs and intercepted clouds in the united states," *Atmospheric Research*, **64** 1-4, 29 (2002).

- [36] H. et al Yang, "Chemical characterization of water-soluble organic aerosols at jeju island collected during ace-asia," *Environmental Chemistry*, **1**, 13 (2004).
- [37] B. T. Mader, J. Z. Yu, J. H. Xu, Q. F. Li, W. S. Wu, R. C. Flagan, and J. H. Seinfeld, "Molecular composition of the water-soluble fraction of atmospheric carbonaceous aerosols collected during ace-asia," *J. Geophys. Res.*, **109** (2004).
- [38] M. Bilde and B. Svenningsson, "Ccn activation of slightly soluble organics: the importance of small amounts of inorganic salt and particle phase," *Tellus*, **56**, 128 (2004).
- [39] R. H. Moore, *Hygroscopic Properties of Atmospheric Aerosols* (Lewisburg, PA, 2006).
- [40] I. N. Tang and H. R. Munkelwitz, "Composition and temperature dependence of the deliquescence properties of hygroscopic aerosols." *Atmos. Environ.*, **27A** 4, 467 (1993).
- [41] *International Critical Tables of Numerical Data, Physics, Chemistry and Technology, 1st Electronic Edition. Available online at <http://www.knovel.com>. (1926-1930, 2003).*
- [42] H. Stephen and T. Stephen, *Solubilities of Inorganic and Organic Compounds* (Macmillan, New York, 1963).
- [43] A. Apelblat and E. Manzurola, "Solubility of oxalic, malonic, succinic, adipic, maleic, malic, citric, and tartaric acids in water from 278.15 to 338.15 k." *Journal of Chemical Thermodynamics*, **19**, 317.

- [44] A. Khlystov, C. O. Stanier, S. Takahama, and S. N. Pandis, “Water content of ambient aerosol during the pittsburgh air quality study,” *Journal of Geophysical Research*, **110** (2005).
- [45] M. D. Cohen, R. C. Flagan, and J. H. Seinfeld, “Studies of concentrated electrolyte solutions using the electrodynamic balance. 1. water activities for single-electrolyte solutions,” *Journal of Physics and Chemistry*, **91** **17**, 4463 (1987).
- [46] C. Peng, M. N. Chan, C. K., and Chan, “The hygroscopic properties of dicarboxylic and multifunctional acids: Measurements and unifac predictions,” *Environ. Sci. Technol.*, **35** **22**, 4495 (2001).
- [47] M. Kanikidou, J. H. Seinfeld, S. N. Pandis, I. Barnes, F. J. Dentener, M. C. Facchini, R. V. Dingenen, B. Ervens, A. Nenes, C. J. Nielsen, E. Swietlicki, J. P. Putaud, Y. Balkanski, S. Fuzzi, H. Horth, G. K. Moortgat, T. Winterhalter, C. E. L. Myhre, K. Tsigaridis, E. Vignati, E. G. Stephanou, and G. Wilson, “Organic aerosol and global climate modeling: a review,” *Atmospheric Chemistry and Physics*, **5**, 1053 (2005).
- [48] W. White, “Contributions to light scattering,” *Visibility: Existing and Historical Conditions: Causes and Effects*, pp. 24–102.
- [49] S. Fuzzi, S. Decasari, M. C. Facchini, E. Matta, and M. Mircea, “A simplified model of the water soluble organic component of atmospheric aerosols,” *Geophysical Research Letters*, **28** **21**, 4079 (2001).
- [50] M. T. Parsons, J. Mak, S. R. Lipetz, and A. K. Bertram, “Deliquescence of

- malonic, succinic, glutaric and adipic acid particles.” *Journal of Geophysical Research*, **109** (2004).
- [51] S. D. Brooks, M. E. Wise, M. Cushing, and M. A. Tolbert, “Deliquescence behavior of organic/ammonium sulfate aerosol.” *Geophysical Research Letters*, **29**, 1 (2002).
- [52] E. Andrews and S. M. Larson, “Effect of surfactant layers on the size changes of aerosol particles as a function of relative humidity,” *Environmental Science and Technology*, **27**, 857 (1993).
- [53] M. Y. Choi and C. K. Chan, “The effects of organic species on the hygroscopic behaviors of inorganic aerosols,” *Environmental Science and Technology*, **36**, 2422 (2002).
- [54] S. D. Brooks, P. J. DeMott, and S. M. Kreidenweis, “Water uptake by particles containing humic materials and mixtures of humic materials with ammonium sulfate,” *Atmospheric Environment*, pp. 1859–1868 (2004).
- [55] A. Apelblat, M. Dova, J. Wisniaka, and J. Zabicky, “The vapour pressure of water over saturated aqueous solutions of malic, tartaric, and citric acids at temperatures from 288 k to 323 k,” *Journal of Chemical Thermodynamics*, **27**, 35 (1995).
- [56] S. L. Clegg, P. Brimblecombe, and A. S. Wexler, “A thermodynamic model of the system  $\text{h}^+ - \text{nh}_4^+ - \text{na}^+ - \text{so}_4^{2-} - \text{no}_3^- - \text{cl}^- - \text{h}_2\text{o}$  at 298.15 k,” *J. Phys. Chem.*, pp. 2155–2171 (1998).

- [57] C. N. Cruz and S. N. Pandis, "Deliquescence and hygroscopic growth of mixed inorganic-organic atmospheric aerosol," *Environ. Sci. Technol.*, **34**, 4313 (2000).
- [58] J. A. L. Ruiz, "Morphology and cloud condensation nuclei activity of single-component and multi-component organic aerosols," (2009).
- [59] P. W. Winston and D. H. Bates, "Saturated solutions for the control of humidity in biological research," *Ecology*, **41** **1**, 232 (1960).
- [60] D. Rose, S. S. Gunthe, E. Mikhailov, G. P. Frank, U. Dusek, M. O. Andreae, and U. Poschl, "Calibration and measurement uncertainties of a continuous-flow cloud condensation nuclei counter (dmt-ccnc): Ccn activation of ammonium sulfate and sodium chloride aerosol particles in theory and experiment," *Atmos. Chem. Phys.*, **8**, 1153 (2008).
- [61] W. D. Dick, P. Saxena, and P. H. McMurry, "Estimation of water uptake by organic compounds in submicron aerosols measured during the southeastern aerosol and visibility study," *J. Geophys. Res.*, **105**, 1471 (2000).
- [62] K. A. Koehler, S. M. Kreidenweis, P. J. DeMott, A. J. Prenni, C. M. Carrico, B. Ervens, and G. Feingold, "Water activity and activation diameters from hygroscopicity data - part ii: Application to organic species," *Atmospheric Chemistry and Physics*, **6**, 795 (2006).
- [63] M. N. Chan and C. K. Chan, "Hygroscopic properties of two model humic-like substances and their mixtures with inorganics at atmospheric importance," *Environ. Sci. Technol.*, **37** **22**, 5109 (2003).

- [64] A. J. Prenni, P. J. DeMott, and S. M. Kreidenweis, "Water uptake of internally mixed particles containing ammonium sulfate and dicarboxylic acids," *Atmospheric Environment*, **37 30**, 4243 (2003).
- [65] K. E. H. Huff-Hartz, J. E. Tischuk, M. N. Chan, C. K. Chan, N. M. Donahue, and S. N. Pandis, "Cloud condensation nuclei activation of limited solubility organic aerosol," *Atmospheric Environment*, **40 4**, 605 (2006).
- [66] G. B. Erdakos, W. E. Asher, J. H. Seinfeld, and J. F. Pankow, "Prediction of activity coefficients in liquid aerosol particles containing organic compounds, dissolved inorganic salts, and water - part 1: Organic compounds and water by consideration of short- and long-range effects using x-unifac," *Atmospheric Environment*, **40 33**, 6410 (2006).
- [67] R. C. Reid, J. M. Prausnitz, and B. E. Poling, *The Properties of Gases and Liquids* (1987).